

© Copyright by Shashank Natesh 2012
All Rights Reserved

A NUMERICAL STUDY OF THE FLOW AND HEAT TRANSFER IN THE NEAR FIELD OF A
CYLINDRICAL BUBBLE MOVING IN A NARROW CHANNEL

A Thesis

Presented to

the Faculty of the Department of Mechanical Engineering

University of Houston

In Partial Fulfillment

of the Requirements for the Degree

Master of Science

in Mechanical Engineering

by

Shashank Natesh

December 2012

ACKNOWLEDGEMENTS

First and foremost, I wish to express my genuine gratitude to my advisor Professor Keith Hollingsworth and my co-advisor Professor Stanley Kleis. Their guidance over the course of my stay at University of Houston has had a profound influence on my development, both academic and personal. Their insightful suggestions have steered my research towards many interesting directions. I consider myself fortunate to have had mentors who dedicate so much time and attention to their students. I thank Professor Larry Witte, who in addition to forming my thesis committee, has contributed many valuable comments to this work. I thank him for his kindness to share his vast experience in the field of heat transfer with me.

I am also grateful to Trina Johnson for always being available for assistance. For an international student in this department, she is no less than a surrogate mother. I thank my lab-mates Aritra, Eddy, Khaled, Leyuan and Wasy to have provided invaluable help, ranging from deep discussions on two-phase heat transfer to comic relief. My roommates and my good friends at the university also deserve special attention for their company and lunches/get-togethers at Satellite.

I finally express my heartfelt gratitude to my parents, my cousins Karthik and Chitra and my family back home in India for their support, encouragement and understanding. Throughout my studies, they have stood by my side, and without their love and support, I doubt my ability to have successfully completed this thesis.

A NUMERICAL STUDY OF THE FLOW AND HEAT TRANSFER IN THE NEAR FIELD OF A
CYLINDRICAL BUBBLE MOVING IN A NARROW CHANNEL

An Abstract

of a

Thesis

Presented to

the Faculty of the Department of Mechanical Engineering

University of Houston

In Partial Fulfillment

of the Requirements for the Degree

Master of Science

in Mechanical Engineering

by

Shashank Natesh

December 2012

ABSTRACT

A direct numerical simulation is performed of a cylindrical bubble moving in a pressure-driven flow of NovecTM 649 in a heated channel. The upper wall is an electrically heated metal foil, and the bubble diameter is on the order of the channel spacing. Phase change is not included to isolate the contribution of the liquid motion to the heat transfer. The simulation is performed with FluentTM, the volume-of-fluid method tracks the interface, and the reference frame translates with the bubble.

The heat transfer coefficient increases tenfold due to the bubble passage. A lobed structure immediately behind the bubble forms in the surface heat flux, and the surface temperature is depressed over several bubble diameters. A complex horseshoe-like vortex system wraps the bubble and drives the heat flux lobes. The evolution of the heat flux at a point on the surface compares well to predictions of an existing quenching/diffusion model.

TABLE OF CONTENTS

ACKNOWLEDGEMENTS.....	iv
ABSTRACT	vi
TABLE OF CONTENTS	vii
LIST OF FIGURES	ix
LIST OF TABLES.....	xv
NOMENCLATURE	xvi
CHAPTER 1 INTRODUCTION	1
CHAPTER 2 LITERATURE REVIEW	5
2.1 Interface-Tracking Methods.....	5
2.2 Sliding Bubble Dynamics and Heat Transfer	8
2.3 Motivation	21
CHAPTER 3 PHYSICAL MODEL	23
3.1 Model Description.....	23
3.1.1 Single bubble inside a narrow channel	23
3.1.2 Moving reference frame (Lagrangian framework).....	26
3.2 Mathematical Formulation	28
3.2.1 Definition of dimensionless groups	29
3.2.2 Governing equations	30
3.2.3 Fully developed laminar flow in a narrow channel	31
3.2.4 Boundary and initial conditions	34
3.2.5 Wall-adhesion boundary condition	39
CHAPTER 4 NUMERICAL MODEL	41
4.1 Volume of Fluid Method	41
4.2 Numerical Schemes	43
4.3 Model Implementation in Fluent™	44

4.3.1	User defined functions (UDFs)	46
4.3.2	Solution procedure	47
4.4	Computational Domain	50
4.4.1	Computational mesh and boundary conditions	53
CHAPTER 5	RESULTS AND DISCUSSION	58
5.1	Code Validation and Convergence Tests	58
5.1.1	Single phase test case	58
5.1.2	Spatial and temporal convergence	61
5.2	Effect of Bubble Velocity	68
5.3	Wall Heat Transfer	72
5.4	Flow Structure Visualization	78
5.4.1	Velocity vector plots	79
5.4.2	Vorticity fields	84
5.5	Wall Heat Flux – Time History	92
CHAPTER 6	SUMMARY AND CONCLUSIONS	96
6.1	Summary	96
6.2	Conclusions	97
6.3	Recommendations for Future Work	100
REFERENCES	101
APPENDIX A	THERMOPHYSICAL PROPERTIES OF WORKING MATERIALS	107
APPENDIX B	USER DEFINED FUNCTIONS	108

LIST OF FIGURES

Figure 2.1	Variation of liquid temperature in the channel after bubble passage shown at various time intervals (Kusuda et al., 1981).	9
Figure 2.2	Change in the temperature of the heated surface due to passage of the bubble during one cycle: (a) saturated liquid; (b) subcooled liquid with $\Delta T_{\text{sub}} = 70 \text{ K}$ (Monde et al., 1989).....	10
Figure 2.3	The corrected physical model for enhancement of heat transfer in saturated liquid flows, accounting for latent heat transport by evaporation (Monde and Mitsutake, 1989).....	11
Figure 2.4	Shear layer shown at the lower extremity of the large cap-shaped sliding bubble (Bayazit et al., 2003).	13
Figure 2.5	Wake behind the sliding bubble showing a wavy chaotic fluid pattern (Qiu and Dhir, 2002).....	14
Figure 2.6	Velocity field in front (left image) and rear (right image) of the sliding bubble determined using PIV (Qiu and Dhir, 2002).	15
Figure 2.7	Sequence of liquid crystal images for passage of the FC-87 sliding vapor bubble. The bubble is moving towards the right and is depicted by an ellipse in each image. A time span of 140 ms separates each successive image (Hollingsworth et al., 2009).....	16
Figure 2.8	Vector plot (left) and the temperature field (right) of the sliding bubble motion at an instant for a plate inclination of 30° (Senthilkumar, 2009).....	17
Figure 2.9	Variation in the fluid temperature field (right) between (a) 65 ms and (b) 125 ms as the vapor bubble (left) slides along the surface (Akhtar, 2011).	20

Figure 3.1	A schematic showing the initial configuration for the physical model.....	24
Figure 3.2	A two-dimensional schematic of the numerical domain and the precursor velocity profile in (a) a stationary laboratory reference frame and (b) a moving reference frame.....	27
Figure 3.3	Flow between two parallel walls, top heated and bottom insulated (adapted from Özer, 2010).	32
Figure 3.4	Fully developed velocity and temperature distributions for the precursor flow at $Nu = 5.385$ (adapted from Özer, 2010).	34
Figure 3.5	An illustration showing laboratory reference frame and moving reference frame axes.	35
Figure 3.6	An illustration showing the measurement of contact angle within two phases (taken from Fluent™ user guide).....	40
Figure 4.1	Schematic showing the cell terminology in the modified HRIC scheme (adapted from Fluent™ user manual)	44
Figure 4.2	An overview of the solution procedure (adapted from Fluent™ 6.3.26 user manual)	49
Figure 4.3	The computational domain showing the $75\ \mu m$ thick plate (red), the $1.25\ mm \times 10\ mm \times 30\ mm$ channel, and the $1.5\ mm$ diameter bubble (blue) along with the relevant boundaries.....	51
Figure 4.4	The computational domain seen from (a) $Z = 0$, (b) $Y = 0$ and (c) $X = 0$ showing the plate (dark grey); channel (light grey) and the bubble (blue). Initialized velocity profile (dotted line) and temperature distribution (solid line) vs. z -direction are shown in (b).....	52

Figure 4.5	Example of an adapted grid (light grey) showing hanging nodes (black dots) at the interface of grid adaption below the heated foil (dark grey) 53
Figure 4.6	Illustration of the computational meshed grid, where a portion is enlarged to depict the solid domain/plate (in red), fluid inlet (blue) and side-wall (green). Mesh sizes for (a) channel are as follows: $\Delta x = \Delta y = 156.25 \mu m$, $\Delta z = 62.5 \mu m$; and (b) plate are as follows: $\Delta x = \Delta y = 156.25 \mu m$, $\Delta z = 0.075 \mu m$ 55
Figure 5.1	Temperature distributions of the heated wall and the bulk fluid along the channel for the HS precursor flow at $t^* = 1$ 60
Figure 5.2	Heat flux and Nu distribution along the heated wall center-line for the HS precursor flow at $t^* = 1$. Theoretical curves are from Heaton et al. (1964). 60
Figure 5.3	Grid independence test on temperature distribution of the heated wall during HS run at (a) $t^* = 0.5$, where the coarse grid curve is shifted 1.5 mm to the left and (b) $t^* = 1$, where the coarse grid curve is shifted 3 mm to the left 62
Figure 5.4	Grid sensitivity check for heat flux distribution of the heated wall for the HS run at $t^* = 1$ 63
Figure 5.5	convergence for Nusselt number distribution of the heated wall for the HS run at $t^* = 1$ 63
Figure 5.6 (a)	Grid convergence for the fluid temperature during HS run at $x = -7.5 \text{ mm}$ ($t^* = 0.5$). 64
Figure 5.6 (b)	Grid convergence for the fluid temperature during HS run at $x = -2.5 \text{ mm}$ ($t^* = 0.5$). 64
Figure 5.7	Centerline fluid temperature profiles in the near-field and far-field of the bubble at two different t^* values for the medium grid. 65

Figure 5.8	Time sensitivity test for the medium grid during HS run: dimensionless temperature profile at $x = -2.5 \text{ mm}$ and $t^* = 0.25$	66
Figure 5.9	Heat flux distribution along the centerline of the heated wall versus x -direction at different computational times.....	67
Figure 5.10	Distribution of the streamwise velocity across the channel at the channel centerline at $x = -2.5 \text{ mm}$	68
Figure 5.11	Plots of (a) driving temperature difference against streamwise position and (b) non-dimensional driving temperature difference versus x^* , for LS and HS runs at $t^* = 3$	70
Figure 5.12	Wall heat flux distribution against normalized streamwise position comparing HS and LS runs at $t^* = 3$	71
Figure 5.13	Nu distribution versus normalized streamwise direction for HS and LS cases at $t^* = 3$	71
Figure 5.14	Node values of temperature of the heated plate at initialization with $T_{iw} = 327 \text{ K}$	72
Figure 5.15	Node values of volume fraction of the vapor phase in the symmetrical x - y plane at initialization.....	72
Figure 5.16	Contours of surface heat flux (kW/m^2) on the heated wall for HS run at $t^* = 5$	73
Figure 5.17	Contours of wall temperature (K) on the heated wall for HS case at $t^* = 5$. The location of the bubble interface on the heated wall is depicted by a dashed line.	74
Figure 5.18	Temporal evolution of total surface heat flux (left) and temperature (right) on the heated wall for HS case. Range for heat flux and temperature is specified in W/m^2 and K respectively	76

Figure 5.19	Isometric view illustrating the planes, Plane A ($x = -1 \text{ mm}$), plane B ($x = 1 \text{ mm}$), plane C ($x = 0 \text{ mm}$), plane D ($y = 0.3 \text{ mm}$) and plane E ($y = 1 \text{ mm}$); created near areas of high heat transfer activity on the heated wall and overlaid with contours of vapor phase (bubble).	79
Figure 5.20	Fluid temperature overlaid with in-plane velocity vectors on plane A ($x = -1 \text{ mm}$) to explain the formation of the high heat flux spots C1 and C2. Fluid in the center of the channel is flowing perpendicular to the page, inwards.	80
Figure 5.21	Fluid temperature overlaid with in-plane velocity vectors on plane B ($x = 1 \text{ mm}$) to explain wall heat transfer upstream of the bubble. Fluid in the center of the channel is flowing perpendicular to the page, inwards.	81
Figure 5.22	Fluid temperature overlaid with in-plane velocity vectors on plane C ($x = 0 \text{ mm}$) to explain the thermal structure along the bubble shoulders. Fluid in the center is flowing perpendicular to the page, outwards.	82
Figure 5.23	Fluid temperature overlaid with in-plane velocity vectors and line contours of vapor phase volume fraction on plane D ($y = 0.3 \text{ mm}$).	83
Figure 5.24	Fluid temperature overlaid with in-plane velocity vectors and transparent contours of vapor phase density on plane E ($y = 1 \text{ mm}$).	84
Figure 5.25	Contours of vorticity magnitude and velocity vector plots on the symmetry plane ($y = 0 \text{ mm}$).	85
Figure 5.26	Transverse vorticity (y -axis) on the heated wall showing footprints of vortices to the left and right of the bubble.	86
Figure 5.27	Contours of vorticity magnitude and velocity vector plots at varying distances from the heated wall (HS run at $t^* = 5$).	88

Figure 5.28	Formation, stretching and the transport of the upstream vortex pair by the near-wall flow, visualized at different streamwise positions around the bubble (HS run at $t^* = 5$). The axis is same for all the contour plots.	90
Figure 5.29	Iso-surface of vorticity magnitude, $\omega = 175 \text{ 1/s}$ (HS run at $t^* = 5$). Contours are colored with temperature in the range shown above, over-laid with velocity vectors and the bubble is indicated by contours of vapor density (transparent blue).	91
Figure 5.30	Time history of the wall heat flux of a point on the heated surface for LS and HS cases compared with Özer's (2010) quenching/diffusion model.	93
Figure 5.31	Energy added into the heated plate due to single bubble passage as a function of the mixed length.	94
Figure 5.32	Power added to the plate per unit streamwise length downstream due to passage of a single confined cylindrical bubble for HS and LS cases. The integration is computed over an area shown by dashed line on the surface heat flux contour.....	95

LIST OF TABLES

Table 3.1	Parameters used in low-speed and high-speed cases.	26
Table 4.1	Function and current use of User-defined Functions	47
Table 4.2	Dimensions of the computational domain	50
Table 4.3	Dimensions of the computational grid (in μm).....	54
Table 4.4	Boundary conditions and their associated User-defined Functions	56

NOMENCLATURE

Roman Characters

a	Linearized coefficient for the scalar variable ϕ in Eq. (4.8)
\vec{A}	Area vector of a surface, m^2
$A_{surface}$	Area of the top wall bounding the channel, m^2
C_p	Specific heat of the fluid, $J/kg\ K$
D	Diameter of the bubble, mm
D_h	Hydraulic diameter of the channel, mm , ($\equiv 2H$)
F_j	Volume fraction (color function) of the j th phase in a cell
\vec{F}_{st}	Force of surface tension, as a source term in the momentum equation, N
\vec{g}	Acceleration due to gravity, m^2/s
h	Heat transfer coefficient of the fluid, $W/m^2\ K$
H	Height of the channel, mm
k	Thermal conductivity of a material, $W/m\ K$
L	Length of the channel, mm
\dot{m}	Mass transfer from vapor to liquid phase or vice-versa, $kg/m^3\ s$
n	Unit vector normal to the liquid-vapor interface
N_{faces}	Number of faces enclosing a cell
n_t	Unit vector tangential to the wall
n_w	Unit vector normal to the wall
nb	Neighboring cells
Nu	Nusselt number, ($\equiv h D_h/k$)
p	Pressure of the fluid (volume-averaged), N/m^2
p_l	Pressure at the interface on the liquid side, N/m^2
p_v	Pressure of the vapor, N/m^2
Pr	Prandtl number, ($\equiv \mu C_p/k$)
\dot{Q}	Heat generation from the solid domain, as a source term in the energy equation, W/m^3
\dot{q}_w''	Surface heat flux on the heated wall, W/m^2

Re	Channel Reynolds number, $(\equiv u_l D_h / \nu)$
Re_b	Bubble Reynolds number, $(\equiv (u_l - u_p) D / \nu)$
S_ϕ	Source of the scalar quantity ϕ per unit volume, W/m^3
S_F	Mass source term as a function of color function F , $kg/m^3 s$
t	Time, s
t_p	Time taken for a point to traverse from left end to the right end of the plate, s
t^*	Dimensionless time $(= t/t_p)$
T	Temperature of the fluid, K
T_b	Temperature of the bottom wall, K
T_{iw}	Temperature of the wall at the left end of domain, K
T_m	Mixing cup (bulk) temperature of the fluid, K
T_w	Wall temperature as a function of time or position, K
u	Velocity component of the fluid (liquid or vapor) in the streamwise (x) direction, m/s
\vec{u}	Velocity of the fluid $(\equiv u\hat{i} + v\hat{j} + w\hat{k})$, m/s
u^*	Dimensionless streamwise velocity component of the liquid, $(\equiv u/u_l)$
u_l	Average streamwise velocity of the liquid (a function of the axial pressure gradient), m/s
u_p	Streamwise velocity of the plate relative to moving reference frame, m/s
\vec{u}_r	Velocity of the moving reference frame, m/s
v	Velocity component of the fluid (liquid or vapor) in the transverse (y) direction, m/s
V	Volume of a computational cell (control volume), m^3
V_b	Absolute streamwise velocity of the bubble in the inertial frame, m/s
w	Velocity component of the fluid (liquid or vapor) in the vertical (z) direction, m/s
W	Width of the channel and the plate, mm
x	X-axis of the stationary (laboratory) reference frame, mm
x^*	Dimensionless streamwise position based on the plate velocity $(= x/Re Pr D_h)$
x_c, X	X-axis of the moving reference frame, mm
y	Y-axis of the stationary (laboratory) reference frame, mm
z	Z-axis of the stationary (laboratory) reference frame, mm

z_c, Z Z-axis of the moving reference frame, mm

Greek Characters

α	Thermal diffusivity of a material, m^2/s
Γ_ϕ	Diffusion coefficient for the scalar quantity ϕ
δ	Thickness of the heated plate bounding the top of the channel ($= 75 \mu m$), μm
Δt	Time-step for the computation, ms
ΔT	Driving temperature difference between the wall and the bulk fluid, K
ΔT_{sub}	Sub-cooling relative to the fluid saturation temperature, K
$\Delta x, \Delta y, \Delta z$	Grid sizes in the x, y, z -direction respectively, mm
∇_s	Surface gradient operator, m^{-1}
θ	Dimensionless temperature of the fluid based on the bulk fluid temperature, ($\equiv (T_w - T)/(T_w - T_m)$)
θ^*	Dimensionless temperature of the fluid based on the bottom wall temperature, ($\equiv (T_w - T)/(T_w - T_b)$)
θ_a	Static contact angle between the liquid-vapor interface and the wall, <i>arc degrees</i>
κ	Surface curvature, m^{-1}
λ	Separation constant for Eq. (3.22)
μ	Absolute viscosity of a fluid, $kg\ m^{-1}\ s^{-1}$
ν	Kinematic viscosity of a fluid, $m^2\ s^{-1}$
ρ	Density of a material, kg/m^3
σ_{vl}	Surface-tension coefficient, N/m
τ and $\hat{\tau}$	External and internal stress respectively, N/m^2
τ_c	Time constant for the heated plate, s
$\bar{\bar{\tau}}$	Volume averaged deviatoric stress for the fluid, N/m^2
ϕ	A general scalar quantity used in Eq. (4.6)
ω	Vorticity magnitude, $1/s$

Subscripts

A Acceptor cell

D	Donor cell
F	Face
ij	From i^{th} to the j^{th} phase
j	j^{th} phase
l	Liquid phase
nb	Neighboring cell
s	Solid
U	Upwind cell
v	Vapor phase

Acronyms

VOF	Volume of fluid
LBM	Lattice Boltzmann Method
CSF	Continuum surface force
UDF	User defined function
$HRIC$	High resolution interface capturing
NVD	Normalized variable diagram
$QUICK$	Quadratic upstream interpolation for convective kinetics
$PRESTO!$	Pressure staggered option
AMG	Algebraic multi-grid
$SIMPLE$	Semi-implicit method for pressure linked equations
GUI	Graphic user interface

CHAPTER 1: INTRODUCTION

The need for heat transfer from a solid surface to a moving fluid at extremely high levels of heat flux (power per unit area cooled) arises in removing absorbed or internally-generated energy from densely-packed electronic packages, components in high-power laser weapons systems, heat exchangers in nuclear fission reactors, and even plasma diverters in proposed nuclear fusion reactors. Cooling these systems with a two-phase flow in small channels that highly confine the vapor phase is an interesting design option in these applications because these flows offer enhanced convection through bubble-driven mixing mechanisms between the near-wall and bulk fluid and energy transfer via evaporation. But if the bulk fluid temperature is equal to the saturation temperature of the liquid the bubbles may grow substantially and create dry-out regions on the heated surface. This may lower the heat transfer rates and cause a sharp localized increase in the surface temperature that can lead to equipment failure. To avoid such problems, a subcooled bubbly flow can be considered as a design alternative. In this situation, the bulk, or mixing-cup, temperature of the liquid is always substantially below the fluid saturation temperature. Bubbles may nucleate on the wall if the wall superheat is sufficiently high, or bubbles can be injected into the flow by an artificial and controlled means. The flow pattern created by bubbles moving through the confined geometry draws low-temperature fluid from the center of the channel towards the wall. These motions increase the temperature gradient at the wall and dramatically enhance the average heat transfer coefficient. Given the confined geometry, enough of the bubble surface can be in the superheated near-wall region to allow the bubbles to persist far downstream without condensing into the subcooled bulk flow.

“Mini-channels” with hydraulic diameters on the order of single-digit millimeters to several hundred microns are ideal for this application. In a single-phase flow, heat transfer

coefficient and hydraulic diameter are inversely related; therefore, large numbers of small channels are desirable. The addition of a vapor phase may further increase the heat transfer coefficient if the resulting flow regime is managed such that the void fraction is limited and dry-out does not occur. As channel sizes enter the “micro-channel” range of near 100 microns or less, the heat flux levels are high, but the total energy removal rate can be too low for many applications given the small mass flux through these channels. Channels with such small diameters also can be difficult to maintain reliably. Thus, channels with sizes around 1 *mm* could be suitable for systems that combine high heat flux and high heat removal rate.

The Heat Transfer and Phase Change Laboratory at the University of Houston have been performing an experimental investigation of these flows at very high subcooling levels (30 °C or more). This work has documented the capacity of bubbles flowing in rectangular mini-channels of 1.5 *mm* channel spacing (3 *mm* hydraulic diameter) to increase the time-averaged heat transfer coefficient by over a factor of three. This increase occurs regardless of the bubble-generation mechanism: uncontrolled heterogeneous nucleation of vapor bubbles; controlled localized generation of vapor bubbles; or injection of air bubbles into the liquid phase. From these experiments, a simple physical model of the cooling process associated with a single bubble passing a spot on the surface has been developed. This model can produce the enhancements measured without any consideration of evaporation. The general conclusion from this work is that it is the liquid-phase flow pattern around a single confined bubble that is largely responsible for the enhancement, and that a more complete picture of the details of this flow field through a direct numerical simulation of a simple model problem is desirable.

This thesis provides a first look at that picture by simulating the model problem of a cylindrical vapor bubble moving through a rectangular channel with relevant characteristics similar to those of the channel used in our past experiments. The commercial software Fluent™

is used to perform a three-dimensional direct numerical simulation (at laminar Reynolds numbers) using the *Volume of Fluid* method for tracking the bubble interface. The simulations are run on a single processor in a standard 32-bit Windows-based operating system with added memory capacity. Given the available resources, the current computational grid may not satisfactorily resolve the large gradients in velocity and temperature near the juncture of the heated wall and the bubble interface. However, it does illuminate and solve all other challenges associated with the approach selected to simulate this model problem, and it provides proof-of-concept results that support an investigation using a finer mesh and a highly efficient computer.

The study considers fully developed laminar flow inside a rectangular channel of spacing 1.25 mm along with initial and boundary conditions consistent with the experiments by Özer (2010). The fluid (liquid and vapor phases) have constant properties consistent with the nominal properties published for the fluid used in the experiments, 3M™ Novec™ 649. Phase change is not included in the simulation in order to isolate the contribution of the liquid motions to the wall heat transfer. The cylindrical vapor bubble of diameter 1.5 mm and a length that spans the channel height is tracked using a Lagrangian (moving) reference frame that translates down the channel at the speed of the bubble. The intent is that the bubble position remains fixed in the computation domain so that a mesh size can be created that conserves computational resources. The upper wall of the channel is attached to a $75\text{ }\mu\text{m}$ thick uniform-energy-generation foil of the type used in the experiments, and the lower wide wall is adiabatic. The temporal response of the foil surface (its capacity to transport and store energy within its volume) is included in the simulation. Mass transport by phase change through the liquid-vapor interface is not allowed, and the contact angle between the interface and the upper and lower walls of the channel is prescribed.

Solutions for the temperature and heat flux distributions of the heated upper surface are computed and compared to the computed velocity and vorticity fields around the bubble. The evolution in time of the heat flux of a point on the heated surface is compared to the simplified model proposed by Özer (2010).

CHAPTER 2: LITERATURE REVIEW

This chapter presents a concise review of various interface tracking methods and of relevant experimental and numerical studies of heat transfer enhancement due to sliding bubbles. The final section in this chapter summarizes the motivation for the current work.

2.1 INTERFACE-TRACKING METHODS

Multi-phase flows demand accurate modeling of sharp interfaces between the phases in the flow. The interface topology must be realistically represented and must capture all the topological changes occurring due to vorticity-driven stretching near the interface. But it is generally difficult to simulate these flows because of (1) the fact that the interface separating the two fluids must be tracked while avoiding any excessive numerical smearing and (2) the inclusion of surface tension in the case of highly curved interfaces. Various numerical simulation techniques, each with their particular benefits and drawbacks have been developed in the past two decades. A brief review of these techniques is presented here.

Level-set methods (Sussman et al., 1994; Sethian, 1996; Chang et al., 1996; Fedkiw and Osher, 2001) use a smooth position function γ to track the interface. A set of points where $\gamma = 0$ represents the interface, the liquid regions are defined as $\gamma > 0$, and the vapor regions are defined as $\gamma < 0$. The equation governing the advection of this position function is

$$\frac{\partial \gamma}{\partial t} = -(\vec{u} \cdot \nabla) \gamma. \quad (2.1)$$

This equation shows that the interface property, γ , is advected by the local fluid velocity. Level-set methods are simple to implement and yield accurate results when the advection of the interface occurs parallel to one of the coordinate axes. But when significant vorticity is present in

the velocity fields, the interfaces can get deformed, and this method suffers from loss of volume and accuracy.

The *Lattice Boltzmann* method (LBM) is a particle-based discretization method, which solves the Boltzmann equation. It considers a typical volume element of the fluid which acts as a collection of particles represented by a particle velocity distribution function for each fluid component at each grid point. Time is counted discretely and the particles can collide with each other under the action of applied forces. The collisions of these particles are modeled such that the time-averaged motion of the particles is consistent with the Navier-Stokes equations. Thus, LBM is favored when multiple moving objects (such as bubbles, droplets etc.) are being treated. Ladd (1994) used LBM to calculate gas-particle drag in particulate suspensions and Sundaresan et al. (2002) extended the method to deformable interfaces and studied the dynamics of isolated gas bubbles in quiescent liquids. However, this method may possess the disadvantage of creating artificial coalescence of dispersed elements (bubbles or drops).

The *Volume of Fluid* (VOF) method (Hirt and Nichols, 1981; Youngs, 1982; Rudman, 1997; Rider and Kothe, 1998; Bussman et al., 1999) uses a color function $F(x, y, z, t)$ that indicates the partial amount of fluid present at a certain position (x, y, z) and time t . Equation (2.2) represents the advection of the color function, which can be solved by a variety of available schemes (geometric reconstruction, HRIC etc.), to minimize numerical diffusion.

$$\frac{DF}{Dt} = \frac{\partial F}{\partial t} + (\vec{u} \cdot \nabla F) = 0. \quad (2.2)$$

The interface orientation is also important along with the position of the interface, which follows from the gradient of the color function. Modern VOF techniques include the piecewise linear interface calculation (PLIC) method attributed to Youngs' (1982) work. The accuracy and the capabilities of this PLIC-VOF algorithm greatly exceed that of the older VOF algorithms such as those of the Hirt and Nichols' VOF method (1981). But again, a drawback of the VOF method is

similar to that of LBM, the apparent numerical merging of the interfaces that occurs when the distance between the interfaces is less than the size of a computational cell. But unlike the front tracking methods, VOF does not require any specific algorithms for breaking (or merging) of the interface in the case where coalescence actually prevails. Recently, Akhtar (2011) successfully applied a three-dimensional VOF model, based on Youngs' method, to simulate the interaction between a vapor bubble and an inclined superheated wall on an adaptive tree-based grid structure. Kenning et al. (2011) performed a three-dimensional simulation using the VOF method to study the flow field within a rectangular micro-channel and the heat transfer from the channel wall during the growth of a bubble in the channel.

In *marker particle* methods (Rider and Kothe, 1995; Welch et al., 1965) marker particles are assigned to a particular phase (vapor or liquid) and are used to track the motion of that fluid and thus the interface. Navier-Stokes equations are solved by retrieving the Eulerian fluid properties at instantaneous positions of the marker particles. These methods are extremely robust and accurate and can be used to locate the interface subjected to intense shear and vorticity in the fluid velocity fields. But these methods are computationally expensive, especially in three-dimensions. Difficulties arise when the interface stretches or shrinks considerably, so that marker particles must be added or subtracted during the simulation. A sub-grid model is then applied to facilitate the merging and breakup of the interfaces.

Front-tracking methods (Unverdi and Tryggvason, 1992; Esmaeeli and Tryggvason, 1998; Tryggvason et al., 2001) track the interface with the use of markers (triangles), connected to a set of points, and a fixed or Eulerian grid is used to solve the Navier-Stokes equations. This method is accurate but is difficult to implement because of the need to re-mesh the Lagrangian interface and map that data onto the Eulerian mesh. Difficulties may arise when coalescence or breakup of bubbles is considered, and this situation may require a proper sub-grid model. Unlike the LBM

and VOF, however, the automatic merging of interfaces does not occur in these methods because a separate mesh is used to track the interface. Thus, this property is useful when considering swarming of bubbles in a fluid and it offers considerable flexibility to assign different properties (such as dynamic contact angle and surface tension coefficient) to separate the bubbles in the flow.

2.2 SLIDING BUBBLE DYNAMICS AND HEAT TRANSFER

Our understanding of the heat transfer enhancement due to sliding bubbles inside a narrow channel would benefit greatly from a thorough understanding of the flow structure around the bubble. Many numerical and experimental studies have been conducted in the realm of two-phase flow research with phase combinations ranging from air-water systems to refrigerant-vapor flows. This section summarizes studies judged to be an important background for the current investigation.

Research into the dynamics of sliding bubbles commenced with the need to understand the heat transfer enhancement arising from flow-boiling inside inclined or horizontal tubes and inside shell-and-tube heat exchangers. The heat transfer associated with these sliding bubbles was similar in magnitude to that occurring in annular or slug flows where a liquid microlayer is present between the bubble and the wall. A couple of studies (Cooper and Lloyd, 1969; Koffman and Plesset, 1983) support the above observation. Maneri and Zuber (1974) first performed experiments to study the motion of air bubbles rising along an inclined surface in a pool of deionized water or methanol. Both the liquid and the surface were at room temperature and it was determined that the bubble rise velocity depends on bubble volume, tank spacing, fluid properties and the inclination of the surface. For an inclination of 30 to 90 degrees from vertical, they found that the rise velocity of the bubble depends on the properties of the fluid.

Kusuda et al. (1981) measured the temperature change occurring in an electrically heated stainless steel foil due to bubble passage inside a narrow rectangular vertical channel (20 mm wide, 2 mm deep and 450 mm long). They proposed a theoretical model for the enhancement of heat transfer based on the relationship between the measured change in the surface temperature and the period of the passing bubble. The model is based on the assumptions that: (i) most of the superheated liquid is swept away by the bubble passing along the heated surface; (ii) a thin liquid film always remains between the heated surface and the passing bubble, however evaporation from its surface can be ignored; (iii) the stationary liquid at the bulk temperature immediately covers the heated surface after the bubble passes, as illustrated in Figure 2.1. Based on these assumptions, the problem was treated as heat conduction from a semi-infinite solid, since the thickness of the liquid microlayer was very thin compared with its width.

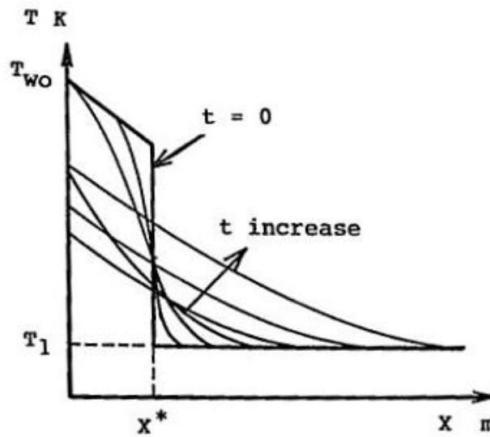


Figure 2.1 Variation of liquid temperature in the channel after bubble passage shown at various time intervals (Kusuda et al., 1981).

Monde (1988) applied the model proposed by Kusuda et al. (1981) to constant heat flux and constant temperature boundary conditions on the heated surface without evaporation from the microlayer. He concluded that for the constant heat flux boundary condition, the heat is first transported by latent heat of evaporation of the liquid film and is followed by sensible heating of

the liquid behind the bubble. In a later study, experiments were conducted by Monde et al. (1989) to report surface temperature changes in the heated surface during one cycle for both saturated and subcooled bulk liquid flows. Figure 2.2 shows that in the case of saturated liquid, the temperature drops as the bubble reaches the heated surface while in the subcooled liquid the temperature rises. This difference in wall temperature was attributed to the evaporation of the liquid film on the interface when the bubble covers the heated surface.

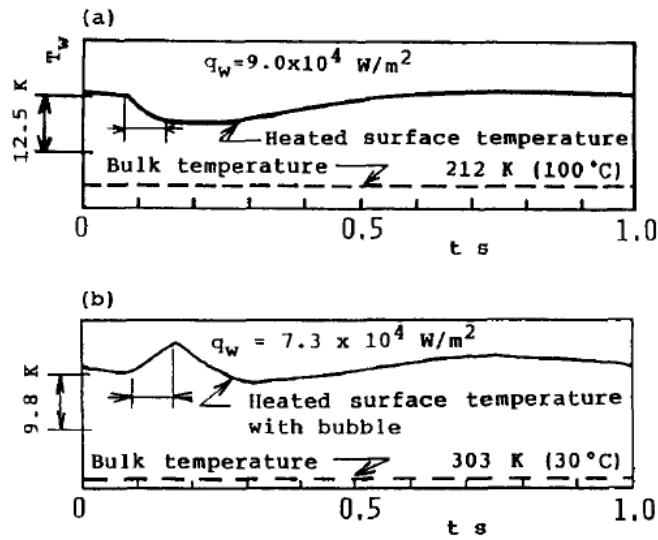


Figure 2.2 Change in the temperature of the heated surface due to passage of the bubble during one cycle: (a) saturated liquid; (b) subcooled liquid with $\Delta T_{sub} = 70 \text{ K}$ (Monde et al., 1989).

Monde and Mitsutake (1989) corrected the Kusuda et al. (1981) model by accounting for the evaporation of the liquid microlayer as follows: the heated surface is cooled by evaporation for a specific time duration during which the surface is covered by the passing bubble; saturated liquid from the bulk flows into the space immediately after the bubble passes, as shown in Figure 2.3. The results from this study were compared with existing experimental data (Monde et al., 1986). The heat transfer enhancement is predicted well in the low heat flux region; agreement becomes less satisfactory for high heat fluxes due to sensible heat transfer added by the flow along the heated surface.

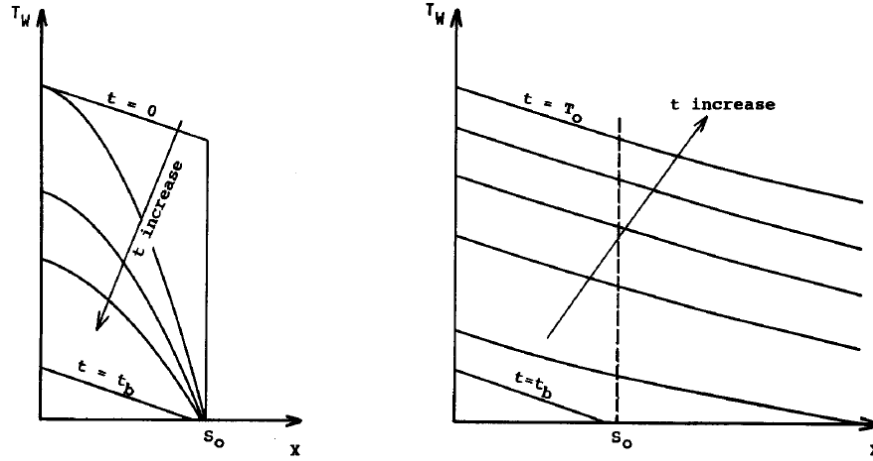


Figure 2.3 The corrected physical model for enhancement of heat transfer in saturated liquid flows, accounting for latent heat transport by evaporation (Monde and Mitsutake, 1989).

Houston and Cornwell (1996) predicted the heat transfer enhancement caused by sliding bubbles in a tube under both evaporating and non-evaporating conditions. The experiments were performed in a boiling cell arrangement consisting of 34 tubes, 33 being stainless steel tubes and a copper test-cylinder, in two in-line columns. R113 was used as the test liquid and heat flux was obtained from the temperature gradient along the test-cylinder. The experiments concluded that heat transfer due to bulk-liquid turbulent convection mechanism caused by the translating bubbles was the most significant portion of the total heat transfer.

Thorncroft and Klausner (1999) also presented conclusive evidence that sliding bubbles enhance heat transfer in forced convection boiling. Measurements were made during both vertical up-flow and down-flow in FC-87 at both saturated and subcooled conditions. Vapor bubbles were generated from one side of the test section which was attached to a Nichrome heating surface. Images were obtained from a high-speed digital camera as the test section was a clear tube. Distinct differences were noted between up-flow and in down-flow. As much as 52 % of the total heat transfer in up-flow with single-phase inlet conditions was attributed to the motion of sliding bubbles. The heat transfer associated with a sliding vapor bubble contained

contributions from both turbulent convection and latent heat transport, which could not be distinguished from the boiling experiments. In order to discriminate between the contributions of the two mechanisms, a subcooled single phase up-flow was established by using an air-bubble injection system to promote air bubble wall attachment. These air bubble injection experiments demonstrated that bulk turbulent enhancement is a major heat transfer mechanism in forced convection boiling, which was in agreement with Houston and Cornwell (1996). This experimental study also provided new ways to model heat transfer mechanism during forced convection boiling by stating that nucleate boiling and bulk turbulent mixing are inter-dependent mechanisms. The bubble dynamics in forced convection boiling are strongly influenced by bulk flow behavior and hence play a significant role in enhancing bulk flow heat transport. However, the boiling correlations used in this study did not attempt to mechanistically account for the sliding bubble heat transfer mechanism, so the model had to be re-examined.

Kenning et al. (2000) and Bustnes (2002) examined the heat transfer from a single vapor bubble sliding on a downward facing heater surface. High-speed video was used to observe the bubbles sliding along the surface and liquid crystal thermography was utilized to obtain spatial variations of surface temperature. A thin liquid layer was assumed to exist between the heated surface and the bubble in the bubble contact area. Based on the transient conduction model proposed for this liquid layer and the wall temperature measurements, it was concluded that 10% of the heat input *to the bubble* comes from the bubble contact area on the heated wall. The remaining 90% was associated with the wedge-shaped region near the stagnation point of the bubble and the previously heated liquid around the remaining surface of the bubble.

Bayazit (2000) and Bayazit et al. (2003) also studied the enhancement of heat transfer due to sliding bubbles. The bottom surface of an electrically heated thin foil was exposed to the sliding bubbles. The upper side of the foil was exposed to still air and coated with thermochromic

liquid crystals. The change in the recorded hue of the liquid crystal layer with time was analyzed to yield a measure of the heat transfer due to the passage of a single bubble and a measure of the thickness of the liquid microlayer between the bubble and the heated surface. Two synchronized cameras, one showing the bubble location and one the response of the surface, were used and FC-87 was used as the fluid. The wake behind the bubble was suggested in an image of a large cap-shaped bubble shown in Figure 2.4. Here, a thin shear layer can be seen due to changes in the index of refraction in the high-gradient region near the wall. The shear layer, which appears to contain small vortices, appears to mark a triangular wake. The bubbles were also observed to create a temperature depression on the heated surface of about one-third of the driving temperature difference. Nearly all that drop occurred in a triangular region behind the bubble and it recovers slowly after the bubble passes.

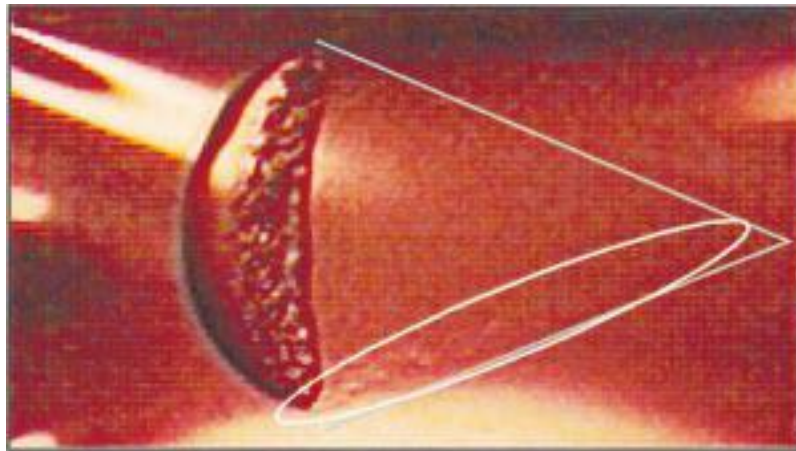


Figure 2.4 Shear layer shown at the lower extremity of the large cap-shaped sliding bubble (Bayazit et al., 2003).

Qiu and Dhir (2002) and Manickam and Dhir (2003) presented the heat transfer and flow patterns associated with a sliding bubble on a downward facing heated surface in subcooled and nearly saturated conditions. Tests were conducted with PF-5060 as the working fluid and the

bubble was generated at an artificial cavity. Figure 2.5 shows an indication of the bubble wake observed for an inclination angle of 15° .

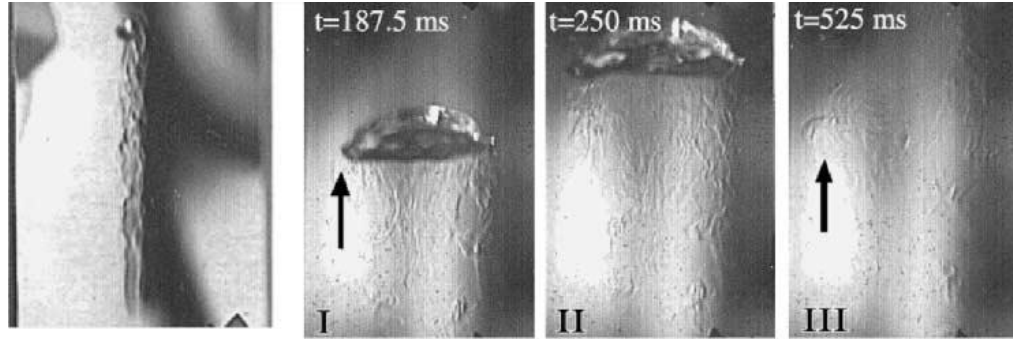


Figure 2.5 Wake behind the sliding bubble showing a wavy chaotic fluid pattern (Qiu and Dhir, 2002).

Particle image velocimetry (PIV) was used to obtain the velocity field around the bubble. Liquid in front of the bubble was observed to be pushed outwards and liquid behind the bubble was pushed inwards. This motion created a strong latitudinal vortex as seen in Figure 2.6, and was responsible for bringing colder liquid from the surroundings into the thermal layer.

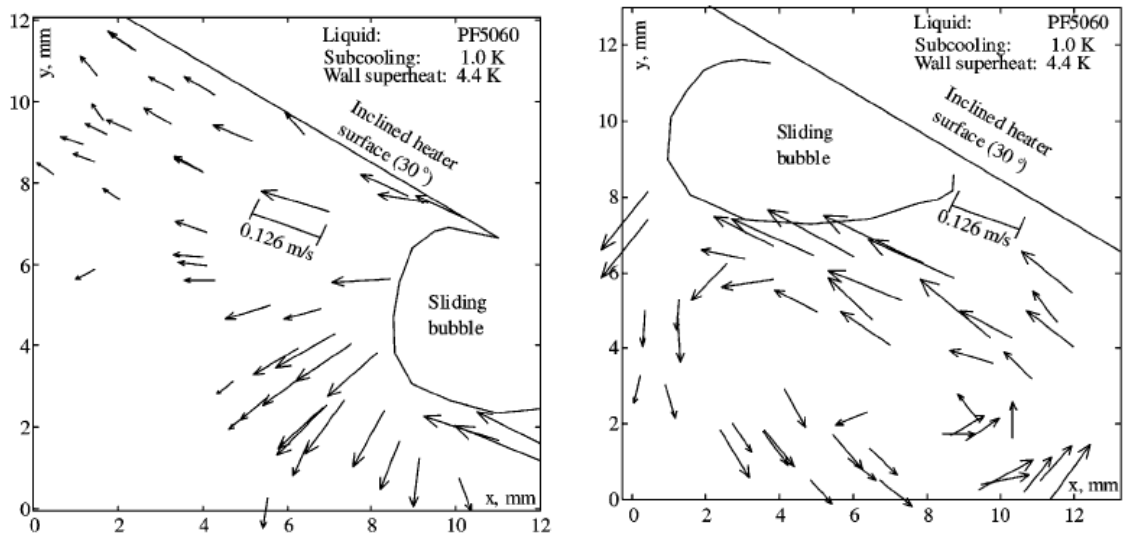


Figure 2.6 Velocity field in front (left image) and rear (right image) of the sliding bubble determined using PIV (Qiu and Dhir, 2002).

Li and Dhir (2007) developed a semi-empirical three-dimensional computational model for a single PF-5060 bubble sliding along an isothermal surface using level set method. A relationship between dynamic contact angle and the liquid-vapor interface velocity was employed to account for the shape and motion of the sliding bubble, data for which is gathered from Maity (2000). The general shape evolution of the bubble (from spheroids to bubble-caps) and the liquid agitation around the bubble compared well with the experimental results of Qiu and Dhir (2002). Among the numerical results, wall heat flux was observed to increase significantly behind the bubble but due to an isothermal boundary condition on the heated surface, no temperature changes were noticed. The study failed to report standard details concerning the accuracy and consistency of the numerical scheme and grid independence.

Hollingsworth et al. (2009) expanded the work done by Bayazit et al. (2003) using the same two-camera sliding-bubble facility. The working fluid was again FC-87. These studies mainly focused on the heat transfer in the bubble wake. A sequence of liquid crystal images, shown in Figure 2.7, exhibits the history of the surface temperature for each indicated bubble location. Local heat transfer coefficients in the wake showed a sharp increase to peaks of around $1500\text{--}2500\text{ W/m}^2\text{ K}$, about 20-50 times the natural convection value. The maxima of the local heat transfer coefficient occurred where the time derivative of the temperature was largest, approximately one bubble width behind the nose of the bubble. The local heat flux enhancement compared to the natural convection precursor values occupied a distance of approximately three times the bubble width. It was concluded that the capacity of the heater to deliver energy (through the exhaustion of the energy stored in the thin foil as its temperature drops) is the dominant source of the additional flux – a thinner foil or a thicker isothermal surface may have behaved differently.

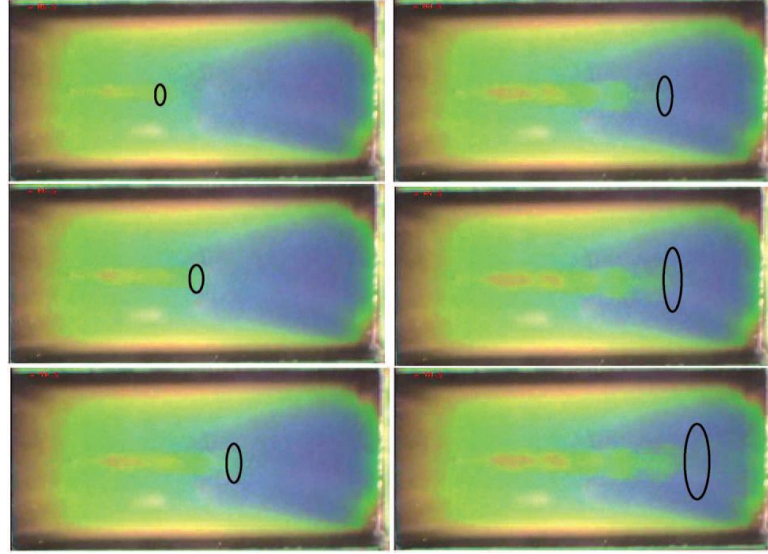


Figure 2.7 Sequence of liquid crystal images for passage of the FC-87 sliding vapor bubble. The bubble moving towards the right is depicted by an ellipse in each image. A time span of 140 ms separates each successive image (Hollingsworth et al., 2009).

Senthilkumar (2009) performed a two-dimensional numerical study to investigate the different convective heat transfer mechanisms involved with the sliding of air bubbles along an inclined thin heated plate placed inside a quiescent isothermal viscous liquid. This study was split into three parts as follows:

- (1) analyze the dynamics of isothermal ellipsoidal rising bubbles in an enclosed domain,
- (2) study the impact of ellipsoidal air bubbles sliding along a heated plate at different inclination angles, without heat transfer,
- (3) study the enhancement effect of an ellipsoidal bubble on heat transfer from an inclined heated plate immersed in water and the resulting flow patterns.

The third part of the study is of utmost importance. Here, the initial temperature of the bulk water and the lower surface of the 25 μm stainless-steel foil are set to 299 K. A uniform heat source is applied to the foil until the temperature of its lower surface reaches 312 K. The resulting wall temperature will increase from the leading to the trailing edge, produced by the natural

convection boundary layer over a uniform heat flux wall. Figure 2.8 shows the velocity vector plots and temperature field in the wake of the sliding bubble. The interaction between the wake and the thermal boundary layer showed similar results to that of Qiu and Dhir (2003) where a vortex structure brings colder fluid onto the surface in the wake of the bubble. A significant temperature drop was observed immediately after the bubble passage and the extent of the zone of influence grew with time, explained by the mixing between the wake and the boundary layer. Temperature fluctuations were observed for a foil inclination of 30° , and were attributed to the bouncing of the bubbles. Although this study provides insight into the underlying mechanisms of mixing and vortex-shedding responsible for increase in wall heat transfer, a more realistic three-dimensional model with forced convection flow could provide a detailed understanding of the fluid-flow mechanisms around the sliding bubble.

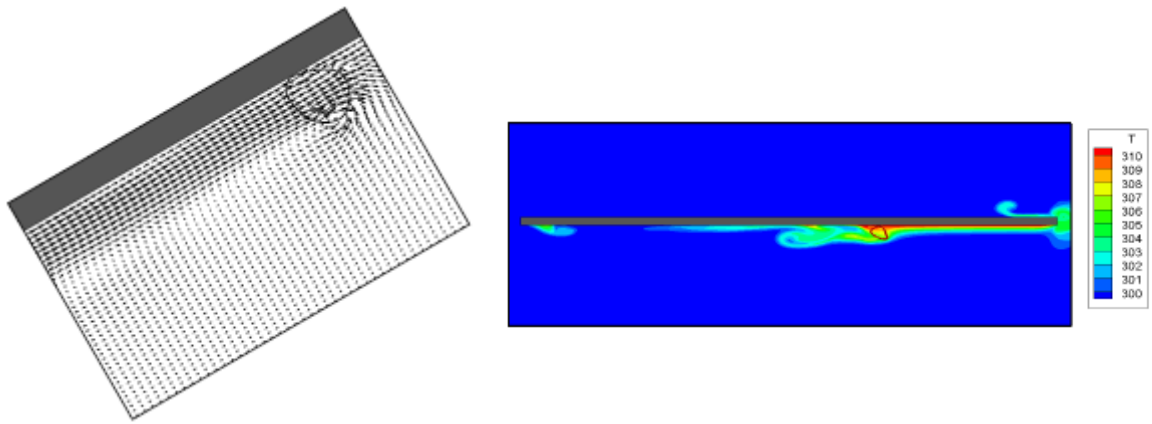


Figure 2.8 Vector plot (left) and the temperature field (right) of the sliding bubble motion at an instant for a plate inclination of 30° (Senthilkumar, 2009).

Özer (2010) and Özer et al. (2010) performed experiments with a horizontal mini-channel with a rectangular cross-section and an electrically heated thin-foil upper surface. They used liquid crystal thermography to measure the foil temperature while simultaneously imaging the bubble motion with a high-speed camera through a transparent lower channel wall. Using this

facility, Özer et al. (2011) studied the onset of nucleate boiling in a highly subcooled liquid in a manner that couples the temperature response of the heater to the images of the bubble size, density, and speed. Two working fluids, R-11 and Novec-649, were used to create bubble swarms in a highly subcooled laminar flow for a channel height near 1.27 mm . Since the speed of these highly confined bubbles were less than the maximum liquid speed at the channel center and more than the liquid speed near the walls, each bubble creates a wake “ahead” of the bubble in the center of the channel and a wake “behind” the bubble near the walls. Other than a fixed “boiling front”, a thin line of active nucleation sites at the upstream edge of the two-phase region, there were few, if any, other active sites in the channel. They therefore concluded that the action of sliding bubbles downstream of the boiling front caused the large measured heat transfer enhancement, not bubble nucleation. Furthermore, they observed de-activation of individual nucleation sites by bubbles from upstream sliding over the site. Since this experimental study could not extract local liquid velocity and temperature fields, it was unable to elucidate the detailed fluid dynamics caused by bubble passage or distinguish between wake and microlayer mechanisms.

To explain his results, Özer (2010) adopted the quenching/diffusion mechanism introduced by Kusuda et al. (1981). He proposed an unsteady diffusion model with a number of enhancements including the capacity to model the unsteady response of the heated surface and the use of the single-phase temperature profile to initialize the computation. He also introduced the concept of thermally uniform “mixed length” in which a uniform fluid temperature is achieved due to the mixing associated with the quenching process. The mixed length extends from the heated surface across the channel for a distance that is a function of the parameters associated with bubble passage (bubble diameter, time between bubble arrivals at the same surface location) and the material properties of the liquid associated with diffusion. A type of

Fourier number was proposed to collect these parameters. When his model results were matched to his experiments, the mixed length was seen to vary from 15% to 50% of the channel height and correlated well with the Fourier number. Microlayer evaporation was ignored (the bubble was assumed to insulate the surface) in the spirit of the conclusion of past studies that microlayer evaporation was not a large contributor to heat transfer enhancement. Özer concluded that this mixed length concept could be examined further by a numerical study of a single bubble moving inside a channel of similar dimensions.

Oncel (2011) used Özer's facility to investigate the heat transfer enhancement due to controlled production of sliding vapor bubbles with the aid of a Ni-Cr heating wire. The data analysis was the same as used by Özer as well. This study found similar heat transfer enhancement in a flow that was built to exclude active nucleation sites. The action of sliding bubbles and their capacity to transport subcooled liquid from the center of the channel to the wall was determined to be the singular cause of the enhancement. The photographic observations showed that single, slow-moving bubbles formed on the heating wire do not change their volume for some distance down the channel even though the bulk liquid is very highly subcooled. For example, a bubble was seen to shrink 25% after traversing 90 *mm* of the channel in 3 seconds. This observation led to the development of a one-dimensional conduction model to simulate the heat transfer of a single cylindrical bubble in a highly subcooled flow between two parallel plates under the assumption that the residence time on the wire superheats the vapor inside the bubble.

Recently, Akhtar (2011) performed a numerical study of sliding vapor bubbles under an inclined heated plate. The motivation was to compare the computed liquid microlayer thickness to the results from the experiments of Bayazit (2000) and those who followed him. The work was broken into three regimes: the bubble approaching the wall (modeled by Akhtar (2006)), the bubble-wall interaction and the bubble sliding along the wall. Although the microlayer was the

chief motivation, this study mainly discusses the shape evolution of bubbles in all these three regimes and the wall temperature time history as the bubble slides along the surface. The development of a phase change computation based on a proper interface temperature condition, implementation of an adaptive octree based grid structure for resolution of steep gradients (close to the wall and the bubble) and a complete verification of the bubble growth rates for uniform superheat were the key improvements of this work over Akhtar (2006). Figure 2.9 shows an example of his results.

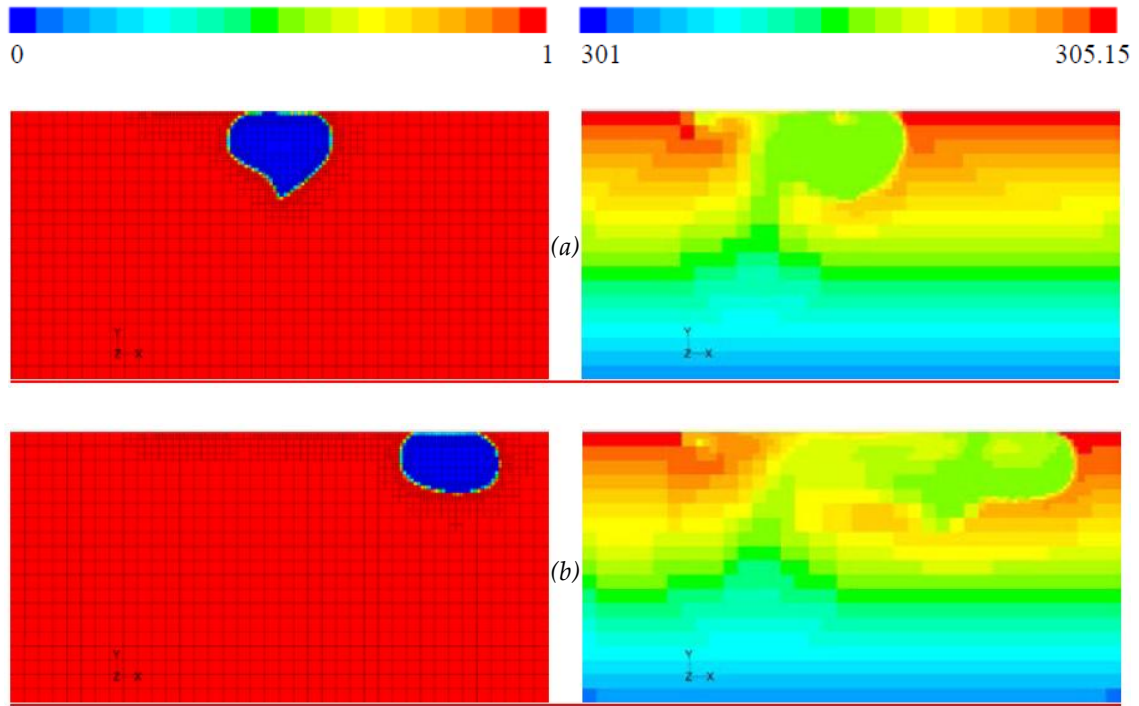


Figure 2.9 Variation in the fluid temperature field (right) between (a) 65 ms and (b) 125 ms as the vapor bubble (left) slides along the surface (Akhtar, 2011).

Iso-temperature contours are shown along with the volume fraction on the symmetric plane at 65 ms, the commencement of the sliding regime and 125 ms, just before the sliding bubble was about to exit the domain. The hot fluid was observed to move in front of the bubble while the cold fluid

impinged the heated plate to the rear of the bubble. A separation line, dividing hot fluid on the right from the cold fluid on the left, existed at the frontal peak of the bubble. A warm circulation region in the wake of the bubble traverses towards the left as the bubble moves towards the right thereby enhancing the heat transfer on the surface, visible from both instances.

2.3 MOTIVATION

Based on the literature review in the previous sections, it is evident that the existing work on the heat transfer enhancement due to purely sliding bubble motion in highly confined geometries is essentially experimental in nature. The numerical works that have been accomplished either consider a natural convection precursor flow, nucleate flow-boiling, or bubble growth due to phase change. So to the author's knowledge, no computational effort has been made to study the influence of forced convective flow around a channel-confined sliding bubble, diameter of the order of the channel height, on the wall heat transfer. The current numerical study is thus motivated by the experiments of Özer (2010) and Oncel (2011) and analyzes the wall heat transfer by elucidating the different flow structure patterns observed around a confined cylindrical vapor bubble of diameter 1.5 *mm* sliding along a thin uniformly-heated foil inside a mini-channel of height 1.25 *mm*. The present computational investigation will be a direct numerical simulation using Volume of Fluid method that will include

- a) a simplified implementation of the channel built by Özer (2010): fully developed laminar flow between two parallel plates, along with initial and boundary conditions consistent with that model,
- b) a uniform-energy-generation foil of the same thickness and properties as Özer's (2010) heated upper wall along with an adiabatic lower wall,

- c) the application of a moving reference frame that traverses with the bubble, so that the bubble remains approximately fixed inside the channel and wakes exist on the upstream and downstream faces of the bubble,
- d) solutions for the evolution of the wall temperature and heat flux distribution on the heated surface as it slides over the bubble,
- e) computation of the vorticity fields and velocity vector fields around the bubble to explain the wall heat flux features, and
- f) wall heat flux time history at a point on the surface.

CHAPTER 3: PHYSICAL MODEL

This chapter presents the physical model selected for this study, explains the assumption and limitations inherent in that selection, and introduces the moving reference frame used with the computational approach. The formulation of the equations to be solved in the numerical simulation and the analytical solution to the precursor flow are then presented along with the formulation of the boundary conditions and the analytical model of the heated surface of the channel.

3.1 MODEL DESCRIPTION

3.1.1 Single bubble inside a narrow channel

The model is that of a fully three-dimensional subcooled transient laminar flow around an isolated cylindrical bubble, 1.5 mm in diameter, in a horizontal rectangular channel of spacing 1.25 mm . One wide wall of the channel is a uniformly heated $75\mu\text{m}$ thick nickel-based metal foil and the opposing wide wall is adiabatic. This configuration, in the absence of the bubble, results in a laminar single-phase forced-convection heat transfer process where the mixing-cup (bulk fluid) temperature remains below the saturation temperature of the liquid at the local pressure. To assure that only single-phase convective processes are considered, no phase change at the bubble surface will be allowed and there is no fluid microlayer between the bubble and the walls. Instead, the bubble will be initialized as a cylinder spanning the channels such that the bubble interface is normal to the walls at the contact location. Heat transfer from the wall will be directly to the vapor phase of the working fluid for points on the heated wall covered by the bubble's footprint. Mass, momentum and energy equations for the vapor within the bubble will be solved along with those for the liquid phase. Figure 3.1 shows a two-dimensional plane through the centerline of the channel. The center of the bubble is initially placed at a distance of one-fourth of

the length of the channel from the right side of the domain. The upper wall of the channel is a 75 μm thick plate with the same nominal material properties as the electrically-heated thin foil used in the experiments of Özer (2010) and Oncel (2011). A uniform internal energy generation rate is specified in accord with those experiments. The top surface of the heated plate is adiabatic.

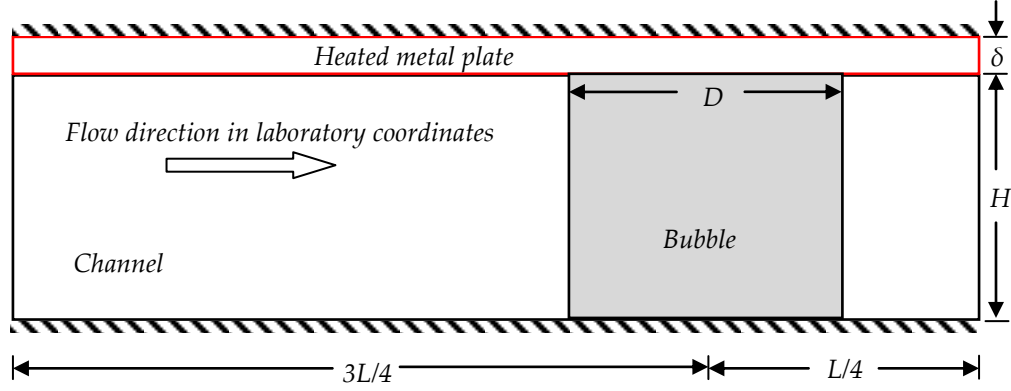


Figure 3.1 A schematic showing the initial configuration for the physical model.

There are a number of additional assumptions used in the physical model:

- a) Both phases are Newtonian and incompressible and fluid properties (viscosity, specific heat, thermal conductivity and density) are constant in each fluid phase. However, given that the solver selected for this research will use the Volume of Fluid approach to describing the phases, the properties across the liquid-vapor interface depend upon the value of the volume fraction.
- b) Gravity will be set to zero in the simulation so that gravity-driven mixed convection is removed from consideration.
- c) The channel side walls that bound the transverse extent of the simulated channel are assumed to have zero shear stress in all directions and are adiabatic.
- d) The geometry is symmetric in the transverse direction with respect to the center of the bubble. Although this would afford an advantage in terms of solving only half of the domain and saving computational resources, it may be that the flow forms an oscillatory

pattern near the bubble, and the assumption of symmetry would not allow that pattern to be resolved.

- e) The flow is laminar. The solver is based on the Reynolds-Averaged-Navier-Stokes formulation of the governing equations, therefore, with no Reynolds stress; the computation can be considered a direct numerical simulation.
- f) The bubble will be modeled as moving through a region of the channel where the precursor flow is fully developed in velocity and temperature. Therefore the analytic solutions for the fully developed velocity and temperature profiles are initialized in the fluid domain along with the appropriate temperature profile in the solid domain. The upstream and downstream boundary conditions are set accordingly. To calculate the temperature profiles that are the boundary conditions on the upstream and downstream ends of the upper plate, heat conduction with internal heat generation is assumed inside the plate.
- g) This study does not consider bubble growth or nucleation. The bubble is patched inside the computational domain at the start of the simulation as a cylinder of vapor attached to the top and bottom walls by a static angle of 90° . No phase change is allowed during the course of the simulation and the contact angle is held constant. The surface tension coefficient at the interface (bubble surface) is held constant. Beyond these constraints, the bubble shape may change as it is influenced by drag forces. There is energy transport across the bubble interface, but by definition of the interface, there is no mass transport. The density and mass of the vapor are fixed; therefore, the volume of the vapor remains constant.

Two cases which differ by liquid flow rate are considered for this study, namely low-speed (LS) and high-speed (HS). The parameters (liquid Reynolds number, driving temperature

difference, bubble speed and the bubble diameter) of the low-speed case are taken from an experimental run from Özer (2010). It has a liquid Reynolds number (based on the channel hydraulic diameter) of 152. The high-speed case was limited by the available computational resources, so that a liquid Reynolds number of 304 exactly twice that of the LS case, was selected. Parameters for both cases are shown in Table 3.1. The constant fluid properties in the liquid and vapor phases are those of the working fluid used in the experiments, 3M™ Novec™ 649. The properties of the heated plate are those of HASTELLOY® C-276 alloy. The thermal and physical properties of both these materials are listed in Appendix A.

Table 3.1 Parameters used in low-speed and high-speed cases.

PARAMETER	DENOTATION	VALUE USED DURING SIMULATION (units)	
		Low Speed Case (LS)	High Speed Case (HS)
Wall heat flux	\dot{q}_w''	1907 (W/m ²)	1907 (W/m ²)
Initial wall temperature at the inlet	T_{iw}	327 (K)	327 (K)
Mean liquid velocity	u_l	27 (mm/s)	54 (mm/s)
Plate or bubble velocity	u_p	22 (mm/s)	44 (mm/s)

3.1.2 Moving reference frame (Lagrangian framework)

Given the limited computational resources available for this study, it was unlikely that a long, fine meshed-channel could be implemented such that the bubble was observed in laboratory coordinates as it moved through the channel. To control domain size, a moving reference frame attached to the bubble was implemented. The general method has been tested with the VOF method (Hua et al., 2008; Huang et al., 2009). With this approach, the length of the channel can be chosen independent of the flow time of the simulation. It allows simulation times to be long enough that the starting transients decay, and it also allows the bubble to move along a

heated channel where the mixing cup temperature and the surface temperature are increasing with downstream distance. The moving reference frame is implemented by moving the entire domain with the velocity of the bubble in the negative x -direction. Figure 3.2 illustrates such a translational reference frame. The frame xz refers to the stationary (laboratory) reference frame and the frame XZ represents the moving reference frame.

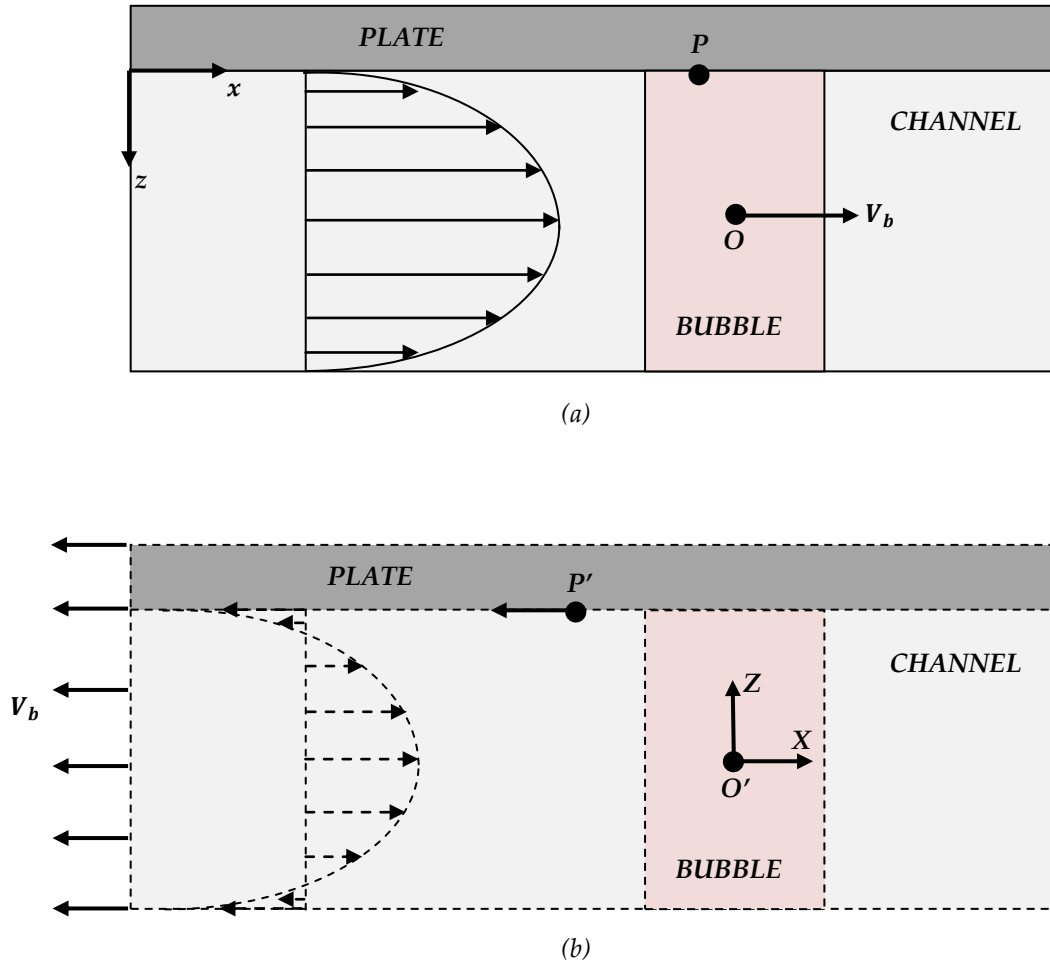


Figure 3.2 A two-dimensional schematic of the numerical domain and the precursor velocity profile in (a) a stationary laboratory reference frame and (b) a moving reference frame.

The positions of the monitoring points on the frames xz and XZ correspond to P and P' , respectively, and the difference in their positions represents the distance moved by the reference frame to the left. Similarly, a point O representing the center of the bubble moves at the constant

bubble velocity of V_b to the *right* in the stationary laboratory reference frame and point O' remains stationary in a moving reference frame.

In addition to modifying the momentum transport equations for the new frame of reference, the velocity boundary conditions at the inlet and outlet boundaries should be changed to account for the frame motion. Therefore, the heated plate and the bottom wall are moving wall boundaries, with constant motion in the negative x -direction. The fluid domain (channel) is initialized with a parabolic velocity profile shifted in the negative x -direction with the velocity of the moving reference frame. The difference in the velocity profiles of the fluid in the stationary and the moving reference frame is apparent in Figure 3.2. The temperature profiles in the fluid and in the plate at the domain boundaries of the moving reference frame are set in such a way that the temperature at the left and right boundaries of the domain increment to reflect the movement of the bubble into progressively warmer sections of the channel as the flow time increases. This aspect of the model is explained at length later in this chapter.

3.2 MATHEMATICAL FORMULATION

The simulation will be performed using the commercial software Fluent™. It is a finite-volume solver which uses the Volume of Fluid method for tracking phase boundaries. What follows is a presentation of the formulation of the governing equations as used in this software.

3.2.1 Definition of dimensionless groups

Before commencing the summary of the governing equations, the dimensionless groups pertinent to this study will be introduced. The channel Reynolds number based on the hydraulic diameter and liquid mean velocity in laboratory coordinates, Re , is defined as

$$Re \equiv \frac{u_l D_h}{\nu}. \quad (3.1)$$

Similarly, the bubble Reynolds number based on the difference between the bubble (or plate) velocity and the liquid mean velocity and the bubble diameter is defined as

$$Re_b \equiv \frac{(u_l - u_p)D}{\nu}. \quad (3.2)$$

The Prandtl number for the liquid, Pr , is defined as

$$Pr \equiv \frac{\mu C_p}{k}. \quad (3.3)$$

In order to define the Nusselt number, the heat transfer coefficient is introduced. The heat transfer coefficient is a measure of the capacity of the flow field to transport thermal energy to or from a surface. It is defined as

$$h \equiv \frac{\dot{q}_w''}{T_w - T_m}. \quad (3.4)$$

The Nusselt number is a dimensionless heat transfer coefficient, which is defined as

$$Nu \equiv \frac{hD_h}{k}. \quad (3.5)$$

In these equations, ν , μ , C_p and k are kinematic viscosity, absolute viscosity, specific heat and thermal conductivity of the fluid. The diameter of the bubble is D , and D_h is the hydraulic diameter of the channel (equals twice the height of the channel), u_l is the mean velocity of the liquid, u_p is the velocity of the bubble (and the plate), \dot{q}_w'' is the total surface heat flux, T_w is the heated wall temperature and T_m is the bulk fluid (mixing-cup) temperature.

3.2.2 Governing equations

The volume-of-fluid method uses a single-field formulation to solve the continuity, momentum and energy equations, which means that these equations are solved by incorporating the volume fraction of one of the phases. All the equations in the current section are excerpted from FluentTM's user guide. For the current numerical study, i.e. a two-phase system, the volume

fraction equation given by Equation (3.6) computes the volume fraction of the secondary (vapor) phase,

$$\frac{\partial}{\partial t}(\alpha_v \rho_v) + \nabla \cdot (\alpha_v \rho_v \vec{u}_v) = 0. \quad (3.6)$$

Here, α_v , \vec{u}_v and ρ_v are volume fraction, velocity and density of the vapor phase, respectively. The volume fraction of the primary (liquid) phase, α_l , is then computed using a constraint given by

$$\alpha_l + \alpha_v = 1. \quad (3.7)$$

The physical and thermal properties like density, specific heat, thermal conductivity and viscosity are determined by the volume fraction of each phase in each computational volume. Since the vapor phase is being tracked, then any property, for example density of the mixture (ρ), in each computational cell is given by

$$\rho = \alpha_v \rho_v + (1 - \alpha_v) \rho_l. \quad (3.8)$$

Here, ρ_l is the density of the liquid phase. Variables such as velocity, pressure and temperature are either mass-averaged or volume-averaged in the same way as the above equation. The one-field formulation presents the following set of continuity, momentum and energy equations for the mixture phase in a translational reference frame:

$$\frac{\partial \rho}{\partial t} + \nabla \cdot (\rho(\vec{u} - \vec{u}_r)) = 0, \quad (3.9)$$

$$\frac{\partial}{\partial t}(\rho \vec{u}) + \nabla \cdot (\rho \vec{u}(\vec{u} - \vec{u}_r)) = -\nabla p + \rho \vec{g} + \nabla \cdot (\vec{\tau}) + \vec{F}_{st}, \text{ and} \quad (3.10)$$

$$\frac{\partial}{\partial t}(\rho C_p T) + \nabla \cdot (\rho(\vec{u} - \vec{u}_r) c T + p \vec{u}_r) = \nabla \cdot (k \nabla T) + \dot{Q}. \quad (3.11)$$

The terms ρ , C_p and k here represent mixture density, mixture specific heat and mixture thermal conductivity, respectively. The variable \vec{u} is the volume-averaged mixture velocity, \vec{u}_r is the velocity of the moving reference frame relative to the inertial frame, p is the volume-averaged mixture pressure, \vec{g} is the acceleration of gravity (this force is zero since gravity is neglected) and

T is the mass-averaged mixture temperature. The source terms in both momentum and energy equations, \vec{F}_{st} and \dot{Q} , are defined per unit volume and represent the surface tension force across the liquid-vapor interface and the volumetric heat generation in the solid, respectively.

Surface tension force is incorporated using the continuum surface force (CSF) model (Brackbill, 1992). This model computes a surface curvature, κ , from the local gradients normal to the liquid-vapor interface. If n is the normal gradient of the vapor phase volume fraction, then the volumetric surface tension is represented by

$$\vec{F}_{st} = \sigma_{vl} \frac{\rho \kappa n}{\frac{1}{2}(\rho_v + \rho_l)}. \quad (3.12)$$

Here, ρ represents the volume-averaged density calculated as per Equation (3.8). In this study, the surface tension coefficient is constant at the interface and only forces normal to the interface are considered.

3.2.3 Fully developed laminar flow in a narrow channel

In order to validate the Navier-Stokes solver, to initialize the problem, and to establish temperature and velocity distributions inside the channel and the plate at the boundaries, the fully developed laminar single-phase precursor flow is analytically solved. The channel geometry is that of two parallel plates, one heated with uniform heat flux and the other insulated. It is important to note that instead of considering a thin solid with uniform heat generation, a uniform heat flux boundary condition is considered for the top wall. The development shown here is taken directly from Özer (2010). Figure 3.3 illustrates the geometry and the shapes of the anticipated temperature and velocity profiles for this configuration.

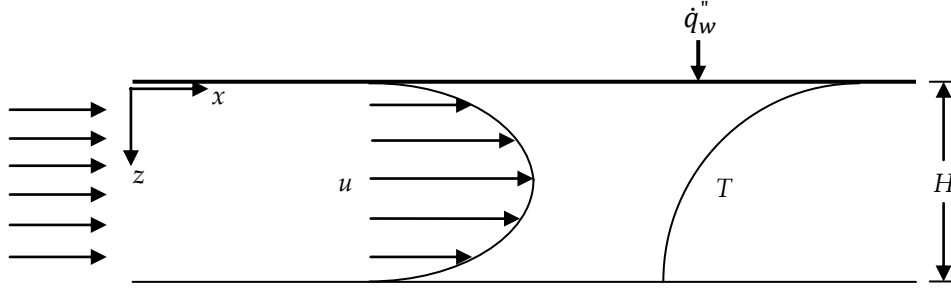


Figure 3.3 Flow between two parallel walls, top heated and bottom insulated (adapted from Özer, 2010).

With relevant assumptions (Özer, 2010), the momentum and energy equations reduce to

$$0 = -\frac{1}{\rho_l} \frac{dp}{dx} + \nu_l \frac{d^2 u}{dz^2}, \text{ and} \quad (3.13)$$

$$u \frac{\partial T}{\partial x} = \alpha_l \frac{d^2 T}{dz^2}. \quad (3.14)$$

The boundary conditions for this configuration are as follows:

$$u = v = 0 \text{ and } \frac{dT}{dz} = -\frac{\dot{q}_w''}{k_l} \text{ at } z = 0, \quad (3.15a)$$

$$\frac{du}{dz} = 0 \text{ at } z = \frac{H}{2}, \text{ and} \quad (3.15b)$$

$$\frac{dT}{dz} = 0 \text{ at } z = H. \quad (3.15c)$$

The momentum equation yields

$$u^* = \frac{u}{u_l} = 6 \left[\left(\frac{z}{H} \right) - \left(\frac{z}{H} \right)^2 \right], \quad (3.16)$$

where

$$u_l = -\frac{H^2}{12\mu_l} \frac{dp}{dx}. \quad (3.17)$$

Similarly, the energy equation yields

$$\frac{1}{\Delta T} \left[\frac{\partial T_w}{\partial x} - \theta \frac{\partial(\Delta T)}{\partial x} \right] = \frac{\partial \theta}{\partial x} - \frac{\alpha_l}{u} \frac{\partial^2 \theta}{\partial z^2}, \quad (3.18)$$

where

$$\theta = \frac{T_w - T(x, z)}{\Delta T}, \quad (3.19)$$

and
$$\Delta T = T_w - T_m. \quad (3.20)$$

In a fully developed flow, Nu is uniform in the streamwise direction and for a uniform heat flux on the top wall

$$\frac{\partial(\Delta T)}{\partial x} = 0. \quad (3.21)$$

The energy equation is thus solved using a separation constant λ so that

$$\frac{1}{\Delta T} \left[\frac{\partial T_w}{\partial x} \right] = \lambda = \frac{\partial \theta}{\partial x} - \frac{\alpha_l}{u} \frac{\partial^2 \theta}{\partial z^2}. \quad (3.22)$$

From the left hand side

$$T_w = \lambda \Delta T x + T_{iw}. \quad (3.23)$$

Here, T_{iw} is the initial wall temperature at $x = 0$, and from the right side with $\partial \theta / \partial x = 0$ for fully developed flow,

$$\frac{\partial^2 \theta}{\partial z^2} = -\frac{\lambda u}{\alpha_l}. \quad (3.24)$$

Equation (3.24) is integrated using the set of boundary conditions in Equation (3.15) to yield

$$\theta = \frac{Nu}{2} \left[\frac{1}{2} \left(\frac{z}{H} \right)^4 - \left(\frac{z}{H} \right)^3 + \left(\frac{z}{H} \right) \right], \quad (3.25)$$

and

$$\lambda \Delta T = \frac{\dot{q}_w''}{\rho_l c_{p_l} u_l H}. \quad (3.26)$$

Using Equations (3.23), (3.25) and (3.26) the temperature profile varying both in streamwise and cross-streamwise direction is given by

$$T(x, z) = T_{iw} + \frac{\dot{q}_w''}{\rho_l c_{p_l} u_l H} x - \frac{Nu}{2} \left[\frac{1}{2} \left(\frac{z}{H} \right)^4 - \left(\frac{z}{H} \right)^3 + \left(\frac{z}{H} \right) \right]. \quad (3.27)$$

Equations (3.16) and (3.25) are the dimensionless fully developed velocity and temperature distributions, respectively, and are plotted in Figure 3.4.

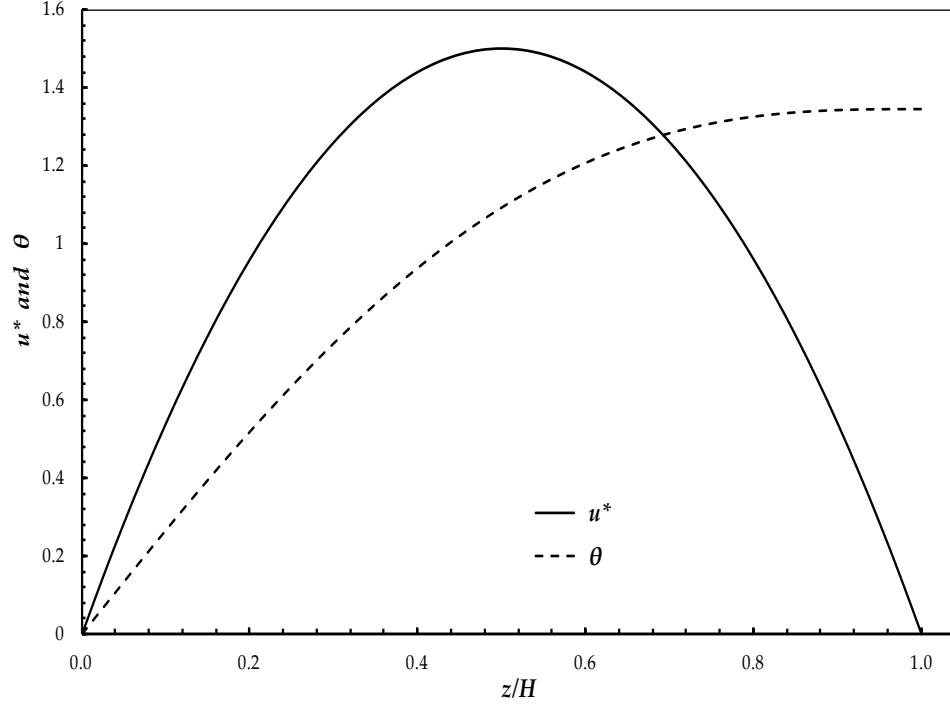


Figure 3.4 Fully developed velocity and temperature distributions for the precursor flow at $Nu = 5.385$ (adapted from Özer, 2010).

3.2.4 Boundary and initial conditions

This section contains a detailed explanation and derivation of the boundary conditions and the initial conditions. Before the boundary and initial conditions are specified, the following variables are introduced,

$$x_c = \frac{4x - 3L}{4}, \quad -\frac{W}{2} \leq y \leq \frac{W}{2} \quad \text{and} \quad z_c = \frac{H - 2z}{2}. \quad (3.28)$$

These variables are represented in Figure 3.5 by two axes, stationary or laboratory (x, y, z) and moving reference frame (x_c, y, z_c) . It should be noted that the y -axis is the same for both reference frames because there is no reference frame motion with respect to that axis.

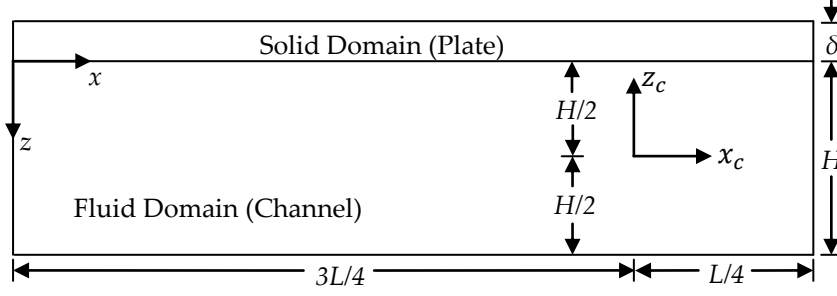


Figure 3.5 An illustration showing laboratory reference frame and moving reference frame axes.

The boundary conditions at the domain surfaces are listed below.

- Channel inlet ($x_c = -3L/4$, $-W/2 < y < W/2$, $-H/2 \leq z_c \leq H/2$)

The liquid entering from the left side of the computational domain (in the moving reference frame) possesses a fully-developed *shifted* parabolic streamwise velocity profile and a fully developed temperature distribution. The temperature in the fluid linearly varying with x -direction in the stationary reference frame now varies with flow time in the moving reference frame, since the reference frame traverses with constant velocity u_p in negative x -direction.

These profiles are given by

$$u(z) = 6 u_l \left(\left(\frac{z}{H} \right) - \left(\frac{z}{H} \right)^2 \right) - u_p, \text{ and} \quad (3.29)$$

$$T(z, t) = T_{iw} + \left\{ \left(\frac{\dot{q}_w''}{\rho_l c_{p_l} u_l H} \right) (u_p t) \right\} - \left\{ \left(\frac{Nu}{2} \right) \left(0.5 \left(\frac{z}{H} \right)^4 + \left(\frac{z}{H} \right)^3 - \left(\frac{z}{H} \right) \right) \right\}. \quad (3.30)$$

- Channel outlet ($x_c = -3L/4$, $-W/2 < y < W/2$, $-H/2 \leq z_c \leq H/2$)

In a similar manner to the channel inlet conditions, the liquid leaving from the right end of the computational domain is also imposed with fully developed streamwise velocity and temperature distributions, given by

$$u(z) = 6 u_l \left(\left(\frac{z}{H} \right) - \left(\frac{z}{H} \right)^2 \right) - u_p, \text{ and} \quad (3.31)$$

$$T(z, t) = T_{iw} + \left\{ \left(\frac{\dot{q}_w''}{\rho_l C_{p_l} u_l H} \right) (L + u_p t) \right\} - \left\{ \left(\frac{Nu}{2} \right) \left(0.5 \left(\frac{z}{H} \right)^4 + \left(\frac{z}{H} \right)^3 - \left(\frac{z}{H} \right) \right) \right\}. \quad (3.32)$$

- Channel side-walls ($-3L/4 < x_c < L/4$, $y = \pm W/2$, $-H/2 \leq z_c \leq H/2$)

The channel side walls act as free slip walls and are imposed with zero-shear stress in all three dimensions and an adiabatic thermal condition given by

$$\tau_x = \tau_y = \tau_z = 0, \quad (3.33)$$

and
$$\frac{\partial T}{\partial y} = 0. \quad (3.34)$$

- Channel bottom wall ($-3L/4 \leq x_c \leq L/4$, $-W/2 < y < W/2$, $z_c = -H/2$)

To account for the motion of the moving reference frame, the bottom wall is imposed with velocity in the negative x -direction and an adiabatic thermal condition given by

$$u = -u_p, \quad v = w = 0, \quad (3.35)$$

and
$$\frac{\partial T}{\partial z} = 0. \quad (3.36)$$

- Channel top wall ($-3L/4 \leq x_c \leq L/4$, $-W/2 < y < W/2$, $z_c = H/2$)

Here, the word “wall” refers to the Fluent™ notion of a bounding surface in the computational mesh, not the physical heated plate. The Fluent™ “top wall” is also moving at the velocity of the reference frame. This “wall” is shared by both the fluid domain and the solid domain of the heated plate, and the solver calculates the heat transfer through the wall and into or out of the adjacent cells of these two domains. The hydrodynamic condition is given by

$$u = -u_p, \text{ and } v = w = 0. \quad (3.37)$$

- Plate bottom wall ($-3L/4 \leq x_c \leq L/4$, $-W/2 < y < W/2$, $z_c = H/2$)

When Fluent™ creates a coupled “wall” as described above, it also creates a shadow of that wall. Hence a coupled wall has two surfaces, a shadow and the wall itself. The plate bottom

wall acts as the shadow of the channel top wall and the thermal conditions of these two walls are coupled. This means both see the same magnitudes for the wall heat fluxes but with opposite sign.

- Plate side-walls ($-3L/4 < x_c < L/4$, $y = \pm W/2$, $H/2 \leq z_c \leq \delta + H/2$)

The side walls of the heated plate are adiabatic and the boundary condition is given by

$$\frac{\partial T}{\partial y} = 0. \quad (3.38)$$

- Plate inlet ($x_c = -3L/4$, $-W/2 < y < W/2$, $H/2 \leq z_c \leq \delta + H/2$)

Given the uniform-flux precursor condition and the motion of the reference frame, the fluid mixing cup temperature in the absence of the bubble varies linearly with the streamwise direction and hence with the flow time for the moving reference frame. Hence the temperature of the plate at the upstream and downstream boundaries must be assigned in a similar way to avoid discontinuities at the boundary shared by the fluid and solid domain.

This condition at the inlet boundary is given by

$$T(t) = T_{iw} + \left\{ \left(\frac{\dot{q}_w''}{\rho_l C_{p_l} u_l H} \right) (u_p t) \right\}. \quad (3.39)$$

- Plate outlet ($x_c = L/4$, $-W/2 < y < W/2$, $H/2 \leq z_c \leq \delta + H/2$)

From the argument stated above, the temperature at the outlet boundary is given by

$$T(t) = T_{iw} + \left\{ \left(\frac{\dot{q}_w''}{\rho_l C_{p_l} u_l H} \right) (L + u_p t) \right\}. \quad (3.40)$$

- Plate top wall ($-3L/4 \leq x_c \leq L/4$, $-W/2 < y < W/2$, $z_c = \delta + H/2$)

The upper surface of the heated plate is adiabatic so that

$$\frac{\partial T}{\partial z} = 0. \quad (3.41)$$

- Initial Condition for the Fluid Domain

The fluid and solid domains are initialized with the fully developed velocity and temperature profiles from the precursor flow. The temperature profile varies linearly with streamwise position due to the uniform heat flux condition as discussed above. The initial profiles are given by

$$u(z) = 6 u_l \left(\left(\frac{z}{H} \right) - \left(\frac{z}{H} \right)^2 \right) - u_p, \text{ and} \quad (3.42)$$

$$T(x, z) = T_{iw} + \left\{ \left(\frac{\dot{q}_w''}{\rho_l C_{p_l} u_l H} \right) x \right\} - \left\{ \left(\frac{Nu}{2} \right) \left(0.5 \left(\frac{z}{H} \right)^4 + \left(\frac{z}{H} \right)^3 - \left(\frac{z}{H} \right) \right) \right\}. \quad (3.43)$$

- Initial Condition for the Solid Domain of the Plate

The temperature of the plate is governed by the energy equation, which is coupled with the fluid energy equations. Temperature variations inside the plate strongly influence the heat flux distribution on the channel top wall (Mei et al., 1995). A dense mesh must be constructed inside the plate and a heat conduction equation with internal heat generation must be solved for the plate. But due to high aspect-ratio problems, only one layer of cells is added on the top of the fluid domain, which acts as the solid domain (plate). The plate traverses with the velocity of the moving reference frame. Fluent™ allows zone motion in two ways: a moving reference frame and a moving mesh method. The former is selected for this study and is represented in the convective energy transfer term of the energy equation for the solid. The initial conditions for the plate are given by

$$u(z) = -u_p, \text{ and} \quad (3.44)$$

$$T(x) = T_{iw} + \left\{ \left(\frac{\dot{q}_w''}{\rho_l C_{p_l} u_l H} \right) x \right\}. \quad (3.45)$$

- Bubble/Vapor phase

User-defined functions are used to initialize the volume fraction of the vapor phase inside the fluid domain and to set liquid-vapor interface boundary conditions. The temperature inside the bubble is initially set to be equal to the saturation temperature of the liquid and this condition is imposed at the start of iterations of each time step. Once the simulation starts, the energy equation is solved for the vapor phase and a temperature field is created inside the bubble in a similar way to that of the liquid. The bubble is attached to the top and bottom channel walls by a static contact angle of 90° , as explained in the next section. The bubble shape may evolve in time in response to the fluid forces at the interface and is determined by performing a normal stress balance (Bush, 1997),

$$p_l = p_v + \sigma_{vl}\kappa - n \cdot (\mu (\nabla \vec{u} + \nabla \vec{u}^T)) \cdot n, \quad (3.46)$$

where n is the unit vector normal to the interface, p_l is the pressure at the interface on the liquid side and p_v is the vapor pressure. The tangential stress vanishes because the viscous stresses in the vapor phase are neglected, which is expressed as

$$t \cdot (\mu (\nabla \vec{u} + \nabla \vec{u}^T)) \cdot n = 0. \quad (3.47)$$

3.2.5 Wall-adhesion boundary condition

Adhesive forces at the point of contact between the liquid-vapor interface and the solid wall give rise to a phenomenon called wall-adhesion. The fluid molecules possess stronger adhesive forces and their tendency to “wet” the wall depends upon the contact angle (θ_a) between the interface and the wall. This angle depends upon the properties of the fluid, and smoothness and the geometry of the wall surface. The normal to the interface is defined using the contact angle from the following relation (Brackbill, 1992) and can be expressed as

$$n = n_w \cos \theta_a + n_t \sin \theta_a. \quad (3.48)$$

Here, n_t lies in the wall and n_w is the unit wall normal directed into the wall. The local curvature of the surface is determined by the combination of the contact angle and the normal calculated one cell away from the wall. Figure 3.6 shows that the contact angle in Fluent™ is measured inside the secondary phase. In the current study, the secondary phase is the vapor phase.

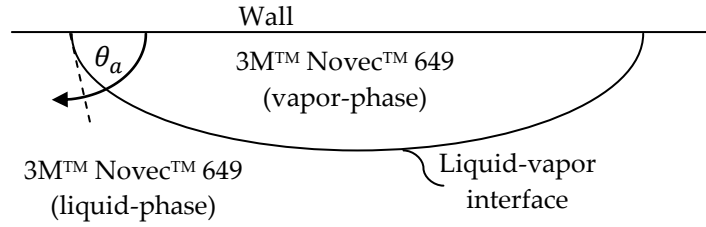


Figure 3.6 An illustration showing the measurement of contact angle within two phases (taken from Fluent™ user guide).

This static contact angle concept is however a physical approximation because θ_a is assumed to be constant at both walls throughout the computation, when in actuality, it depends upon the local fluid conditions and the surface properties. A dynamic contact angle provides an accurate description of the surface curvature because a bubble under flow possesses a different contact angle at the upstream front than at the downstream (Maity, 2000). But due to its unresolved dependence on the material properties and fluid dynamics and the fact that this study requires the bubble to be of a cylindrical shape throughout the computation, implementation of the static contact angle mechanism seemed favorable. Many researchers (Hirt & Nichols, 1981; Kothe et al., 1991; Son, 2001; Mehdizadeh et al., 2011) have adopted the static angle approach in their studies and claim that its role is significant in the case of T or Y type junctions where both phases are in contact with the solid wall.

CHAPTER 4: NUMERICAL MODEL

This chapter presents the numerical framework employed for these simulations. First, a description of the numerical method used to capture the liquid-vapor interface is presented. Then, numerical schemes associated with the spatial and temporal discretization of Navier-Stokes, volume fraction and energy equations, the interpolation near the liquid-vapor interface and the pressure interpolation are explained along with their limitations with the current physical model. The need for implementing user-defined functions (UDFs) is discussed and an algorithm to simulate the model in Fluent™ Version 6.3.26 is presented. The chapter ends with the description of the computational domain, followed by a review of the initial and boundary conditions.

4.1 VOLUME OF FLUID METHOD

The volume of fluid (VOF) method is a popular interface tracking algorithm which has proven to be an effective and a robust tool in simulation of interfacial flows, especially where the liquid-vapor interface undergoes topological changes. The present study incorporates an improvement for the VOF method (Youngs, 1982), originally developed by Hirt and Nichols (1981). This method models two or more immiscible fluids by solving a single set of momentum and energy equations and tracking the fluid interfaces throughout the computational domain. With this single-field approach in the absence of the phase change phenomena, the interfacial dynamics are simple and require no considerations for source terms at the interface. Kataoka (1986) mentioned that this kind of single-field formulation is similar to separate phase formulations characterized by Delhay (1974). The fluid interface between the phases is tracked by solving the continuity equation for a “color function” which is selected to track the phases and

therefore locate the interface. The volume fraction of each phase, F_i , acts as that color function such that the fields of all the variables and properties are shared by the phases and represented as volume-averaged or mass-averaged quantities. Thus for the j^{th} phase, the volume fraction equation takes the form

$$\frac{1}{\rho_j} \left[\frac{\partial}{\partial t} (F_j \rho_j) + \nabla \cdot (F_j \rho_j \vec{u}_j) \right] = S_{F_j} + \sum_{i=1}^n (\dot{m}_{ij} - \dot{m}_{ji}), \quad (4.1)$$

where \dot{m}_{ij} is the mass transfer from phase i to phase j and vice-versa. Since this study is not considering phase change, both the mass source term S_{F_j} and the second term on the right are zero. Hence the above equation reduces to

$$\frac{\partial}{\partial t} (F_j \rho_j) + \nabla \cdot (F_j \rho_j \vec{u}_j) = 0. \quad (4.2)$$

The volume fraction of all the phases adds to unity in each control volume. Thus, depending upon the values of volume fraction, the dynamical and material properties in each cell represent either one of the phases or a mixture of the phases. Since this study comprises of only two phases, primary (liquid) and secondary (vapor), Fluent™ will only compute the volume fraction for the secondary phase and in turn calculate the volume fraction through a summation constraint given by

$$\sum_{j=1}^n F_j = 1. \quad (4.3)$$

Although these equations produce volume fraction values at each cell at every time step, the method does not capture the details of the interface topology because the interface appears as a thin zone of cells where the volume fraction is transitioning between dominant phases. However, a physically useful representation of the interface location can be graphically rendered from these volume fraction data, and these data are used to compute the volume fluxes for the convective term in equation 4.2.

4.2 NUMERICAL SCHEMES

This section introduces the numerical schemes employed by Fluent™ for the discretization of the momentum, energy and volume fraction equations. The algorithms chosen for the interpolation of pressure and the reconstruction of the liquid-vapor interface are discussed.

The discrete values of the scalar variable in the transport equation are stored in cell centers, but the discretization of the convection term requires face values. These face values are interpolated from the cell-centered values by a second-order *upwind* scheme in which the face value is computed from the cell-centered value and the gradient in the upstream cell. This gradient is evaluated by the Green-Gauss cell-based method, where the face values are the averages of the neighboring cell-centered values.

Temporal discretization of the governing equations is carried out using a fully implicit first-order scheme. This method evaluates all the terms in the governing equations, except the transient term, at a future time level. A first-order Eulerian discretization is given by

$$\frac{\partial \phi}{\partial t} = f(\phi), \text{ and} \quad (4.4)$$

$$\frac{\phi^{n+1} - \phi^n}{\Delta t} = f(\phi^{n+1}). \quad (4.5)$$

Equation 4.5 is solved iteratively at each time step before progressing to the next time step. This method is unconditionally stable with respect to the size of the time step.

Upwind schemes are generally exceedingly diffusive in nature, and central differencing schemes are unable to retain the sharpness of the interface and lead to unphysical results in case of VOF simulations. To overcome these inadequacies Fluent™ provides a modified implicit HRIC scheme, originally developed by Muzaferija et al. (1998) to solve the volume fraction equation. It is a normalized variable diagram (NVD) scheme that consists of a non-linear blend of downwind

and upwind differencing. The scheme requires values of volume fraction at the *current* time step. The face values of volume fraction are interpolated from normalized cell values which are computed from the upwind (U), donor (D) and acceptor (A) cell values as shown in Figure 4.1. This scheme provides higher accuracy than second-order and QUICK-type schemes in implicit-VOF simulations (Youngs, 1982) and is computationally less expensive than the explicit Geo-Reconstruct scheme (Mehdizadeh et al., 2011).

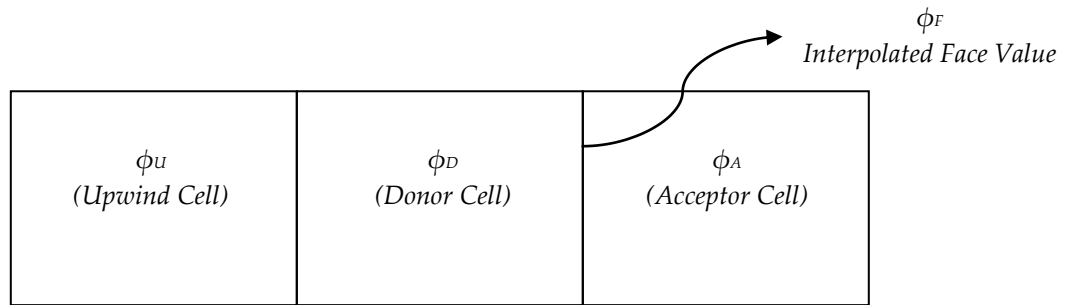


Figure 4.1 Schematic showing the cell terminology in the modified HRIC scheme (adapted from FluentTM 6.3.26 user manual).

In order to interpolate values of pressure at the faces of the cells, FluentTM uses the pressure staggered option (PRESTO!) scheme. It performs a discrete continuity balance on each ‘staggered’ cell or control volume about the face to calculate the ‘staggered’ or the ‘face’ pressure. FluentTM user guide suggests that this scheme provides improved accuracy over other schemes in case of VOF model studies. More details on the implementation of this scheme can be found in Nichita (2010).

4.3 MODEL IMPLEMENTATION IN FLUENTTM

FluentTM 6.3.26 (Ansys Inc.) is a well-known commercial computational fluid dynamics code that is capable of simulating multi-phase flows through the use of the VOF method.

Fluent™ employs a control-volume-based approach to solve the Navier-Stokes and energy equations. The transport equation of a general scalar quantity ϕ can be written in an integral form for an arbitrary control volume V as

$$\int \frac{\partial \rho \phi}{\partial t} dV + \oint \rho \phi \vec{v} \cdot d\vec{A} = \oint \Gamma_\phi \nabla \phi \cdot d\vec{A} + \int S_\phi dV. \quad (4.6)$$

The spatial discretization of Equation 4.6 results in

$$\frac{\partial \rho \phi}{\partial t} V + \sum_f^{N_{faces}} \rho_f \phi_f \vec{v}_f \cdot \vec{A}_f = \sum_f^{N_{faces}} \Gamma_\phi \nabla \phi_f \cdot \vec{A}_f + S_\phi V. \quad (4.7)$$

The face values of the scalar variable ϕ are interpolated from the cell center and its neighboring cell centers as discussed in the previous section. Equation 4.7 is generally non-linear with respect to the scalar flow variable and Fluent™ converts it into a linear form. This leads to a huge set of algebraic equations (for multiple cells) with a sparse coefficient matrix. This linear system is then solved using a point implicit (Gauss-Seidel) solver in combination with an algebraic multi-grid (AMG) method. The AMG method solves the partial differential equations using a hierarchy of discretizations (grids). The steps of this process are as follows (Press et al., 2007):

- i. Reducing the high frequency errors, for example by performing a few iterations of the Gauss-Seidel method, by a process called *smoothing*;
- ii. Down-sampling the residual error to a coarser grid through a process called *restriction*;
- iii. Interpolating the correction computed on a coarser grid into a finer grid by a process known as *prolongation*.

This approach speeds up the convergence of a traditional iterative method by a global correction from time to time, accomplished by computing corrections on a series of coarse grid levels. This

can greatly reduce the number of iterations and processor time required to obtain a converged solution, particularly when the computational grid contains a large number of control volumes.

4.3.1 User-Defined Functions (UDFs)

User-defined functions, or UDFs, are user-created functions that can be loaded into Fluent™ to augment its capabilities. They can be used to define customized boundary conditions, add source terms inside domains, assign variable material properties, change model parameters, start a solution and improve ways of post-processing the final solution. UDFs are written in the C programming language and a single source code file can contain more than one UDF. They are defined using DEFINE macros, a feature supplied in Fluent™. DEFINE macros consists of predefined sub-functions that help accessing data inside the solver, post-process it during and after the solution and perform other complex tasks. Source code files with UDFs are either interpreted or compiled by building a shared library and loading it into Fluent™. The UDFs written inside the code files will be visible in the graphic user interface panel and can be *hooked* (a term used in the Fluent™ jargon) to the solution by selecting the appropriate macro on the panel. The UDFs used for the current study are INIT, PROFILE, ADJUST and SOURCE functions. Table 4.1 gives a brief description, abstracted from Fluent™'s user guide, of these functions and their use in the present study.

Table 4.1 Function and current use of User-defined Functions

DEFINE Macros	Function	Applicability in this study
DEFINE_INIT	A general-purpose macro that can be used to specify the initial values for the solution. As the function name is supplied, the domain to which the function is applied is passed from the solver to the UDF.	Used for initializing the solution inside both the solid and the fluid domains. Used for patching the cylindrical bubble (vapor phase) inside the channel.
DEFINE_PROFILE	A model-specific macro that can be used to define a custom boundary profile varying with spatial coordinates and time.	Used to specify a velocity profile boundary condition at the inlet and outlet of the fluid domain and define the temperature boundary condition at the inlet and outlet of both solid and fluid domains.
DEFINE_ADJUST	A general-purpose macro that can be used to adjust or modify variables inside the code that are <i>not</i> passed as arguments. It can be used to modify velocity, pressure, temperature and other variables and compute integrals. This function is executed iteratively before the transport equations are solved.	Used to specify the temperature of the vapor phase inside the bubble at the beginning of all iterations.
DEFINE_SOURCE	A model-specific macro that can be used to specify custom source terms for solved mass, momentum, energy and user-defined scalar transport equations.	Used to specify the internal heat generation term for the solid domain.

4.3.2 Solution Procedure

Fluent™ employs either a pressure-based or a density-based solver. For all VOF calculations, Fluent™ adopts the pressure-based segregated solver which is similar to the projection method developed by Chorin (1968). This solver uses an algorithm where the

governing equations are solved in a dissociated (i.e., segregated or decoupled from one another) manner. However, during the discretization of the continuity equation, a pressure-velocity coupling SIMPLE (Semi-Implicit Method for Pressure Linked Equations) algorithm (Patankar, 1980) finds the relationship between the velocity and the pressure corrections and obtains the pressure field in a linearized form. This linear equation is again solved by the AMG method before the cell pressure values and face fluxes are corrected to satisfy the continuity equation in further iterations. The solution loop is then carried out iteratively to achieve a converged numerical solution. A detailed solution process for the current two-phase channel flow study is presented below.

The computational mesh generated in Gambit™ is first imported into Fluent™ and the grid parameters are checked along with the mesh details. The grid is then scaled to obtain a computational domain in the preferred units. User-defined database files for properties of the materials are added into the system to access them in the Phases and Boundary Conditions sections of the graphic user interface (GUI) panel. The required VOF model is selected and necessary changes are performed in the GUI panel. Boundary conditions at various surfaces, source terms for the solid domain, initialization process (fully developed velocity and temperature profiles in both domains, patching of the bubble inside the channel and selection of the appropriate numerical schemes and convergence criteria) and initiation of surface animation are some of the important steps to be taken, either by hooking UDFs into Fluent™ or manually selecting the options available in the GUI, before iterating the solution. The flow chart in Figure 4.2 presents the solution procedure. The solution process begins with an initialization of the flow variables with values given in the Fluent™ GUI. The DEFINE_INIT function is called by the pointer, and it initializes both the solid and fluid domains with the user-defined profiles. The iterative loop starts with the introduction of the DEFINE_ADJUST function that assigns the

saturation temperature of the fluid inside the bubble. Momentum equations are solved for all velocity fields followed by the pressure correction equation (tied to the continuity equation), energy equation and lastly the volume fraction equation. DEFINE_SOURCE and DEFINE_PROFILE functions are called upon whenever a variable at a boundary is required. A convergence check is performed at the end of all iterations and the solver either progresses to the next time step or keeps performing iterations at the current time step depending on the satisfaction of convergence criteria which are based on residual values associated with each mass, momentum, and energy equation.

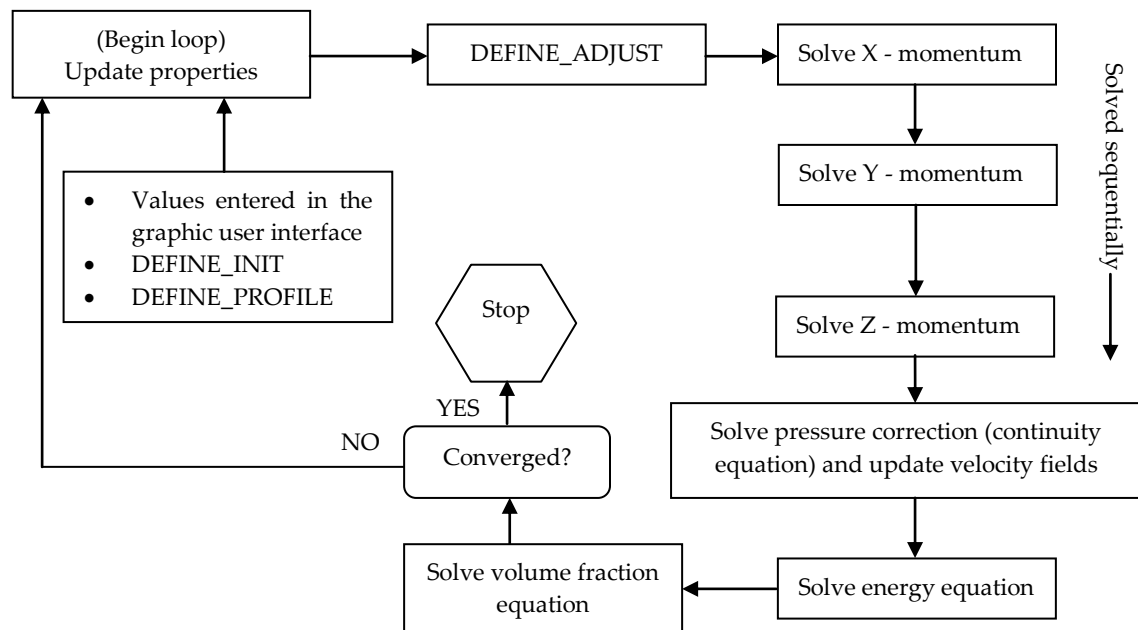


Figure 4.2 An overview of the solution procedure (adapted from FluentTM's user manual).

4.4 COMPUTATIONAL DOMAIN

In the experiments of Özer (2010) and Oncel (2011), the wall temperature depression due to a passing bubble was observed to sustain over large streamwise distances. One of the more difficult challenges of the present study is to create a sufficiently long computational domain while using the available resources. The solution was to track the bubble in a Lagrangian reference frame by moving the walls and the heated plate in the opposite direction at or very near the resulting computed bubble velocity. From the experiments, the bubble velocity was known to be near the mean liquid velocity. A domain length was selected such that it captures the wall heat transfer effects on both upstream and downstream sides of the bubble while allowing a reasonable, if not optimal, computational cell size given the available resources. A length of $20D$ was chosen; $15D$ to the left of the bubble and $5D$ to its right, where D is the diameter of the bubble. The width of the channel ($\pm 10D/3$) was chosen to provide a sufficient transverse ($\pm y$) distance from the bubble. The controlling geometric parameters of the study: height of the channel (1.25 mm), foil thickness ($75\text{ }\mu\text{m}$) and the bubble diameter (1.5 mm) were taken from the experimental apparatus. The resulting channel dimensions are $1.25\text{ mm} \times 10\text{ mm} \times 30\text{ mm}$ long. A detailed schematic of the domain is shown in Figure 4.3 and Table 4.2 lists the dimensions of the numerical domain, and Figure 4.4 illustrates planes bisecting the bubble in all three directions.

Table 4.2 Dimensions of the computational domain.

Denotation	Description	Quantity (units)
L	Length of the channel/plate	30 (mm)
W	Width of the channel/plate	10 (mm)
H	Height of the channel	1.25 (mm)
δ	Thickness of the plate	75 (μm)
D	Diameter of the bubble	1.5 (mm)

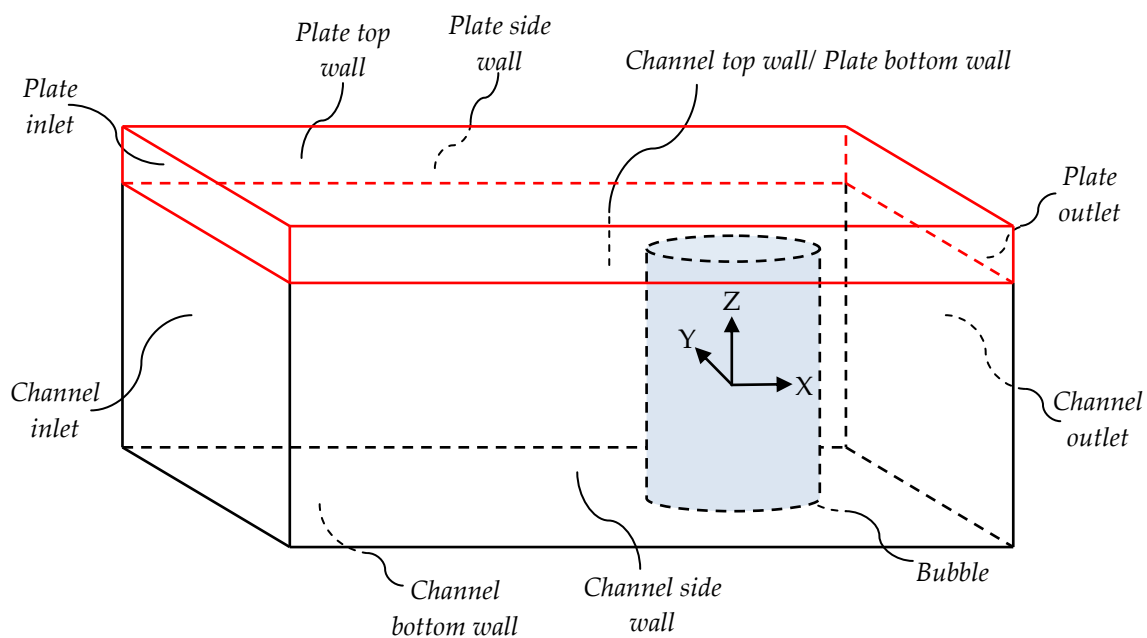


Figure 4.3 The computational domain showing the $75\ \mu\text{m}$ thick plate (red), the $1.25\ \text{mm} \times 10\ \text{mm} \times 30\ \text{mm}$ channel, and the $1.5\ \text{mm}$ diameter bubble (blue) along with the relevant boundaries.

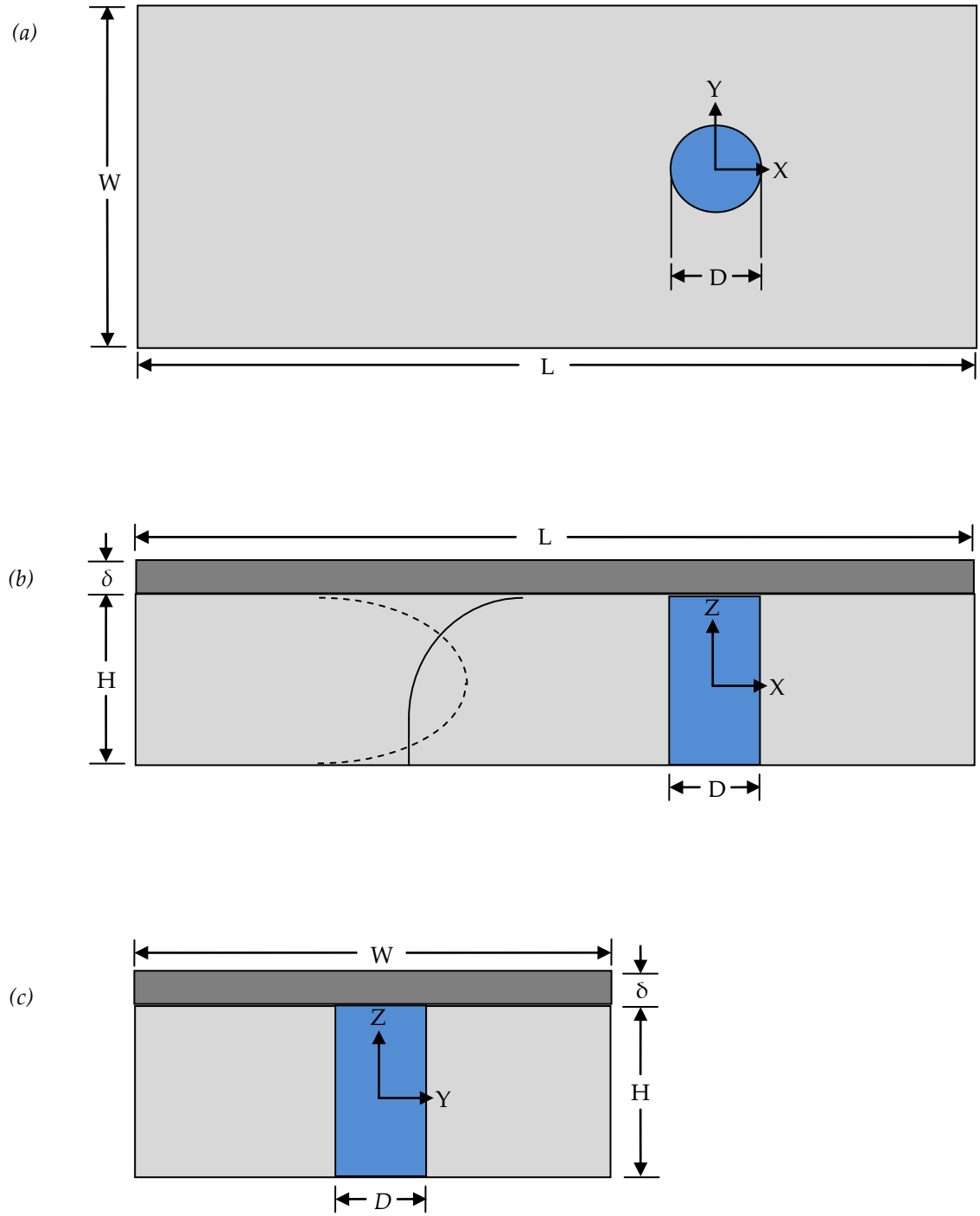


Figure 4.4 The computational domain seen from (a) $Z = 0$, (b) $Y = 0$ and (c) $X = 0$ showing the plate (dark grey); channel (light grey) and the bubble (blue). Initialized velocity profile (dotted line) and temperature distribution (solid line) vs. z -direction are shown in (b).

4.4.1 Computational mesh and boundary conditions

Numerical simulation of the flow around bubbles inside a narrow rectangular channel is a high-dynamic process governed by wall-liquid-vapor interactions and large temperature and velocity gradients near the walls. Thus, high-resolution discretization is necessary to capture the important heat and fluid flow mechanisms. Highly efficient schemes can be used to adapt the grid in areas where the flow undergoes strong variations, in this case near the walls and in the proximity of the bubble. However, an adapted grid can result in hanging nodes. Hanging nodes, as shown in Figure 4.5, are points on edges and faces of a cell that are not vertices of all the cells sharing those edges and faces. The grid refinement using hanging nodes leads to problems with the computation of gradients at this node-interface and significant jumps in temperature and velocity can be observed across the interface owing to large gradients in that region. This problem could be solved by either performing a fourfold refinement of the parent grid beyond that interface or adopting a uniformly discretized grid of a lesser resolution. Since the former requires additional memory and hence more computational time, a uniform discretization is favored.

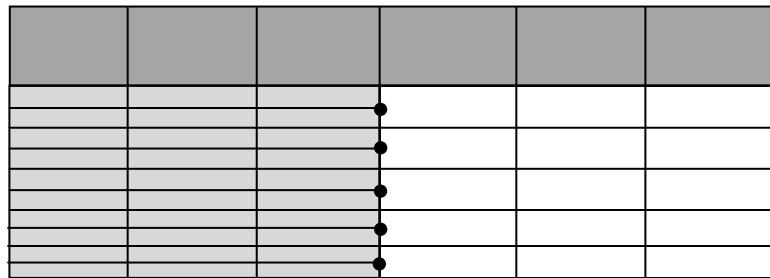


Figure 4.5 Example of an adapted grid (light grey) showing hanging nodes (black dots) at the interface of grid adaption below the heated foil (dark grey).

Gambit™ 2.3.16 (Ansys Inc.) is the mesh generation software used to build all the three parent grids. To reduce numerical errors, a uniform mesh is generated using hexahedral elements. Cell aspect ratio for the channel differs for all three grids with the cell sizes kept same in x - and y -direction and doubled for each successive grid in the z -direction. Inside the channel, cell sizes in the z -direction of $125\ \mu\text{m}$, $62.5\ \mu\text{m}$ and $31.25\ \mu\text{m}$ are chosen for the current study and are subject to sensitivity tests in the next chapter. The dimensions of the three grids are given in Table 4.3.

Table 4.3 Dimensions of the computational grid (in μm).

Type of grid	Channel			Plate (Δz)
	Δx	Δy	Δz	
Coarse	156.25	156.25	125	75
Medium	156.25	156.25	62.5	75
Fine	156.25	156.25	31.25	75

To avoid high aspect ratio problems inside the thin plate, the plate is meshed with a single cell across the z -direction. Hence the cell aspect ratio for the plate remains the same for all the grids with the cell size in the z -direction exactly same as the thickness of the plate. Figure 4.6 shows the meshed *medium-grid* used in the study along with the necessary cell dimensions. This kind of meshing is done to replicate the shell-conduction model in Fluent™ wherein the solver grows a *single* layer of hexagonal cells over the fluid domain to create a *fictitious* solid domain. But the shell-conduction model does not provide a detailed data output for the surfaces of the fictitious solid, and that is why a single layer of meshed solid zone is used for this study.

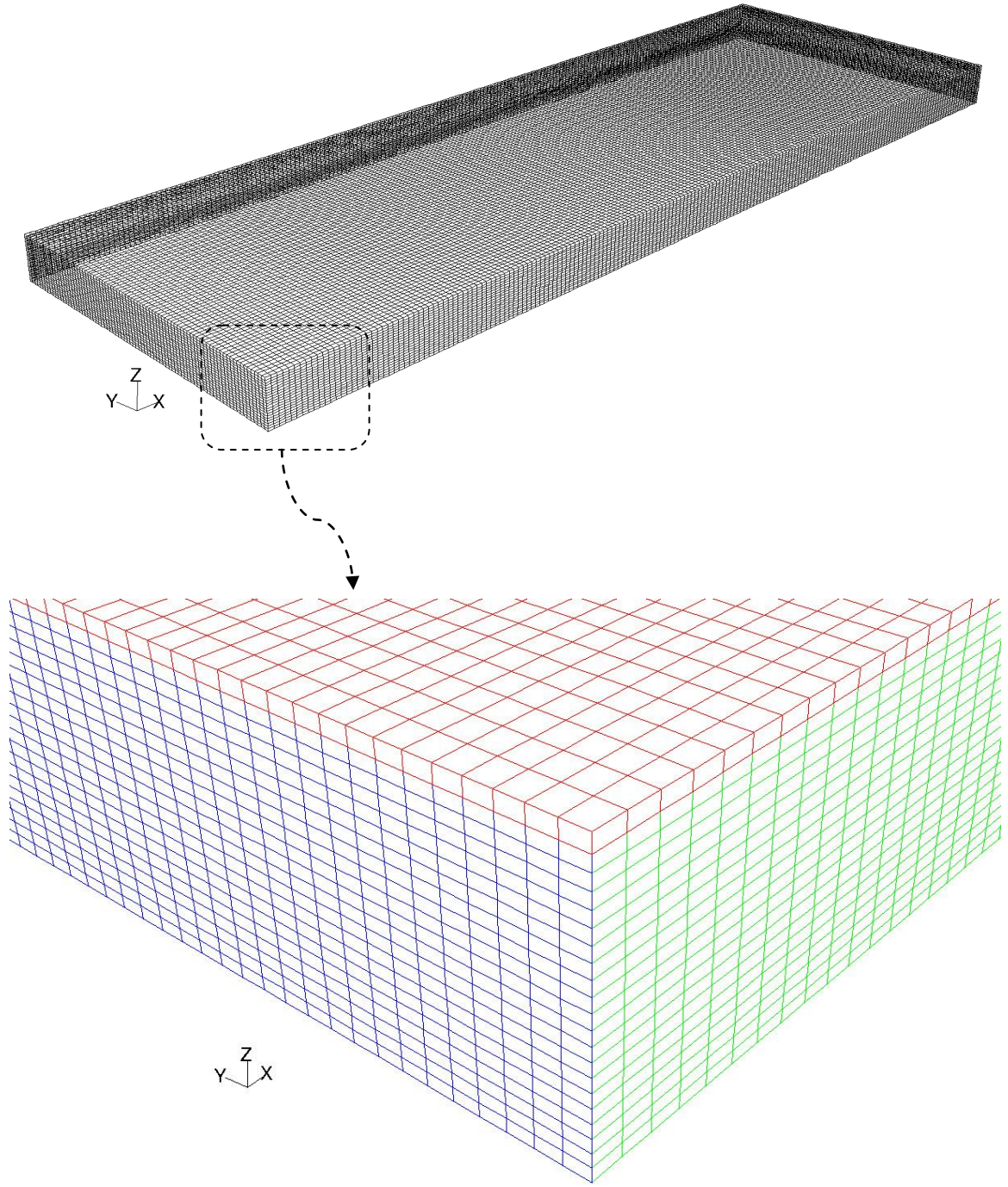


Figure 4.6 Illustration of the computational meshed grid, where a portion is enlarged to depict the solid domain/plate (in red), fluid inlet (blue) and side-wall (green). Mesh sizes for (a) channel are as follows: $\Delta x = \Delta y = 156.25 \mu\text{m}$, $\Delta z = 62.5 \mu\text{m}$; and (b) plate are as follows: $\Delta x = \Delta y = 156.25 \mu\text{m}$, $\Delta z = 0.075 \mu\text{m}$.

Table 4.4 gives a concise review of the boundary and initial conditions discussed in Chapter 3.

Appendix B lists the UDFs that implement these conditions.

Table 4.4 *Boundary conditions and their associated User-defined Functions.*

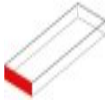
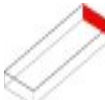



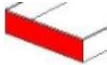




Domain Boundary	Outline	Boundary Conditions (Velocity, Temperature, Wall adhesion etc.)	Implementation in Fluent™
Fluid inlet		$u(z) = 6 u_l \left(\left(\frac{z}{H} \right) - \left(\frac{z}{H} \right)^2 \right) - u_p$ $T(z, t) = T_{iw} + \left\{ \left(\frac{\dot{q}_w''}{\rho_l C_{pl} u_l H} \right) (u_p t) \right\} - \left\{ \left(\frac{Nu}{2} \right) \left(0.5 \left(\frac{z}{H} \right)^4 + \left(\frac{z}{H} \right)^3 - \left(\frac{z}{H} \right) \right) \right\}$ $Z = \frac{(H - 2z)}{2H}$	DEFINE_PROFILE UDF in the graphic user interface (GUI)
Fluid outlet		$u(z) = 6 u_l \left(\left(\frac{z}{H} \right) - \left(\frac{z}{H} \right)^2 \right) - u_p$ $T(z, t) = T_{iw} + \left\{ \left(\frac{\dot{q}_w''}{\rho_l C_{pl} u_l H} \right) (L + u_p t) \right\} - \left\{ \left(\frac{Nu}{2} \right) \left(0.5 \left(\frac{z}{H} \right)^4 + \left(\frac{z}{H} \right)^3 - \left(\frac{z}{H} \right) \right) \right\}$ $Z = \frac{(H - 2z)}{2H}$	DEFINE_PROFILE UDF in the graphic user interface (GUI)
Channel side walls		$\tau_x = \tau_y = \tau_z = 0$ $\frac{dT}{dy} = 0$	In the GUI inside wall boundary conditions

Table 4.4 Boundary conditions and their associated User-defined Functions (continued).

Channel bottom wall		$u = -u_p$ $\frac{dT}{dy} = 0$ $\theta_a = 90^\circ$	In the GUI inside wall boundary conditions
Channel top wall		$u = -u_p$ <p>Thermally coupled wall (shares common boundary with fluid and plate)</p> $\theta_a = 90^\circ$	In the GUI, select <i>coupled</i> under wall thermal boundary conditions
Plate inlet		$T(t) = T_{iw} + \left\{ \left(\frac{\dot{q}_w''}{\rho_f C_{pf} u_l H} \right) (u_p t) \right\}$	DEFINE_PROFILE UDF in the GUI
Plate outlet		$T(t) = T_{iw} + \left\{ \left(\frac{\dot{q}_w''}{\rho_f C_{pf} u_l H} \right) (L + u_p t) \right\}$	DEFINE_PROFILE UDF in the GUI
Plate top wall		$\frac{dT}{dz} = 0$	In the GUI inside wall thermal boundary conditions
Plate side walls		$\frac{dT}{dy} = 0$	In the GUI inside wall boundary conditions
Plate		$u = -u_p$ <p>internal heat generation = \dot{Q}</p>	DEFINE_SOURCE UDF in the GUI

CHAPTER 5: RESULTS AND DISCUSSION

This chapter presents results from the low-speed (LS) and high-speed (HS) cases. The chapter is divided into following sections:

- The first section presents results from a test case to ensure that the numerical code gives the expected results for a known flow. Grid sensitivity and convergence tests are presented.
- In the second section, the effect of bubble velocity on the wall heat transfer is discussed.
- In the third section, the wall heat transfer is analyzed in more detail by examining contours of surface heat flux and surface temperature on the heated wall.
- The fourth section attempts to establish the causal connection between structures in the flow field and the observed spatial pattern in the surface heat flux. This attempt is made using visualizations of iso-surfaces of vorticity tiled with the velocity vectors tangent to those surfaces.
- The last section links this work to the preceding experimental work of Özer by comparing the time histories of heat flux of a point on the heated surface to the results from the quenching/diffusion model Özer proposed and demonstrated to be consistent with his measured data.

5.1 CODE VALIDATION AND CONVERGENCE TESTS

5.1.1 Single phase test case

In order to validate the FluentTM model, simulations were performed for the precursor flow using HS case parameters. The secondary (vapor) phase in the VOF model was turned off and the single-field formulation solves only the primary (liquid) phase. A dimensionless time is

defined to provide a physically meaningful time scale for the computational time required for the initial conditions to relax to a stable solution,

$$t^* = \frac{t}{t_p}. \quad (5.1)$$

Here, t is the flow time and t_p is the time a point on the heated plate takes to traverse from the right end to the left end of the computational domain in the moving reference frame (or the time required for the bubble to traverse a length of channel equal to the length of the domain). Figure 5.1 shows the wall temperature and the mixing cup temperature for the *HS* precursor flow at $t^* = 1$. The slopes are equal and uniform along the channel segment as expected for a channel with a uniform-flux thermal boundary condition.

The definition of the mixing cup temperature is

$$T_m = \frac{\int uT \, dA}{\int u \, dA}. \quad (5.2)$$

The mixing cup temperature as it varies along the channel is not a standard output in the report function in FluentTM. Therefore, a custom field function was created in FluentTM that represents the product of the local fluid velocity (u) and the local fluid temperature (T). The ratio of each integrated (in the y - z plane) value of this custom field function and the corresponding integral of the local fluid velocity gives the mixing cup temperature at a particular streamwise location. FluentTM allows us to perform this two-dimensional integration of the custom field function and the local fluid velocity on each surface starting from the inlet of the channel. These surfaces (of cross sectional area A) are created along the channel at each streamwise location such that every surface is spaced by a cell width from the next surface. Figure 5.2 shows the correspondence between the computed Nusselt number and surface heat flux and the theoretical solution by Heaton et al. (1964) for a fully developed flow between infinitely wide parallel plates.

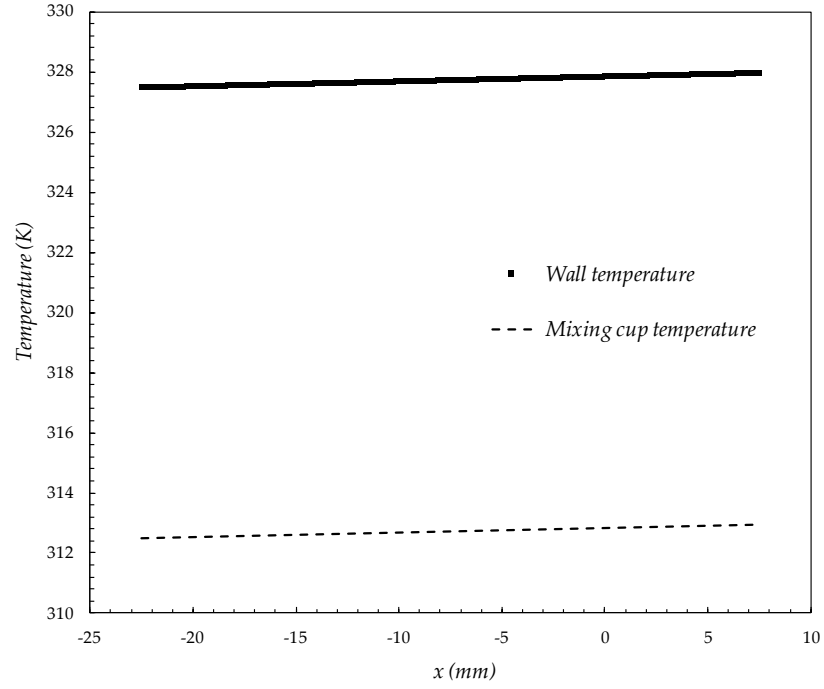


Figure 5.1 Temperature distributions of the heated wall and the bulk fluid along the channel for the HS precursor flow at $t^* = 1$.

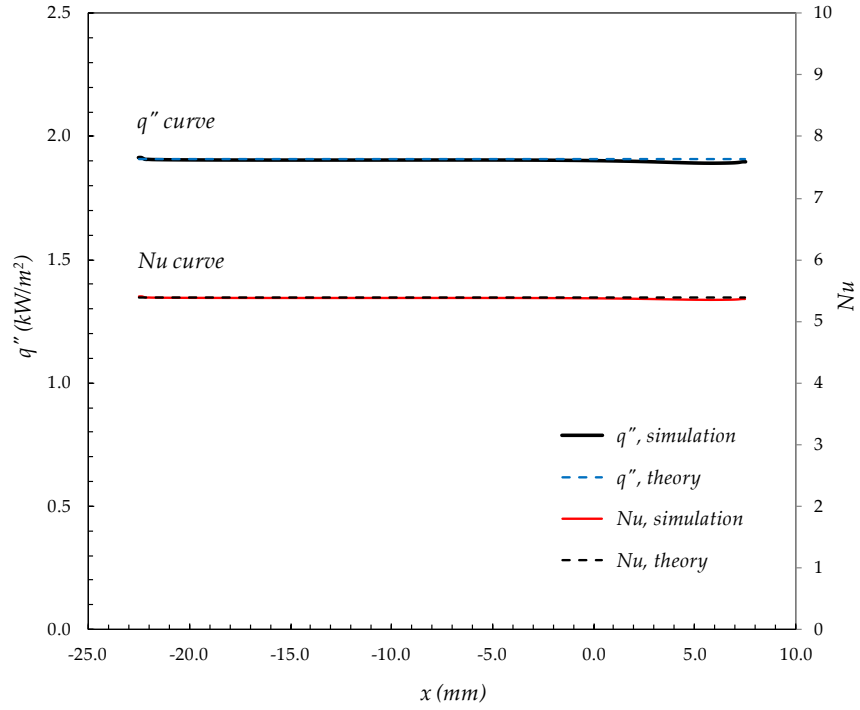


Figure 5.2 Heat flux and Nu distribution along the heated wall center-line for the HS precursor flow at $t^* = 1$. Theoretical curves are from Heaton et al. (1964).

5.1.2 Spatial and temporal convergence

For selection of an appropriate size for the mesh, grid independence tests are conducted for grid sizes (Δz) of 125 μm (coarse), 62.5 μm (medium) and 31.25 μm (fine) using HS parameters. Figures 5.3 (a) and (b) show the temperature distribution along the centerline of the heated wall for the three grid sizes at $t^* = 0.5$ and $t^* = 1.0$, respectively. The coarse-grid curve is shifted in both plots because the bubble moves slightly downstream as the simulation progresses. This bubble motion is a consequence of the inability of the coarse grid to capture the velocity gradients near the bubble. This inaccuracy alters the drag force. The general agreement between the medium and fine grids identifies an acceptable resolution given the resources available.

Similarly, Figures 5.4 and 5.5 show plots of heat flux and Nusselt number distribution along the channel, respectively. For all runs with the bubble present, the streamwise evolution of the mixing cup temperature was computed as a linear rise from the mixing cup temperature impressed by the left (inlet) fluid boundary condition to that impressed by the right (outlet) boundary condition. This simplification avoids the need for the large integrations described in the previous section and avoids the difficulty in defining the temperature inside the bubble. Given that the rise is less than a degree on a 15 degree driving difference; the simplification is a reasonable one. The fine grid produces higher heat flux and Nu values near the rear of the bubble. However, the medium and fine grids agree well except very near the bubble surface.

A new dimensionless fluid temperature is introduced as

$$\theta^* = \frac{T_w - T(x, z)}{T_w - T_b}, \quad (5.3)$$

where T_b represents the temperature of the bottom wall. Figures 5.6 (a) and (b) are plots of θ^* across the channel at two streamwise locations for the three meshes.

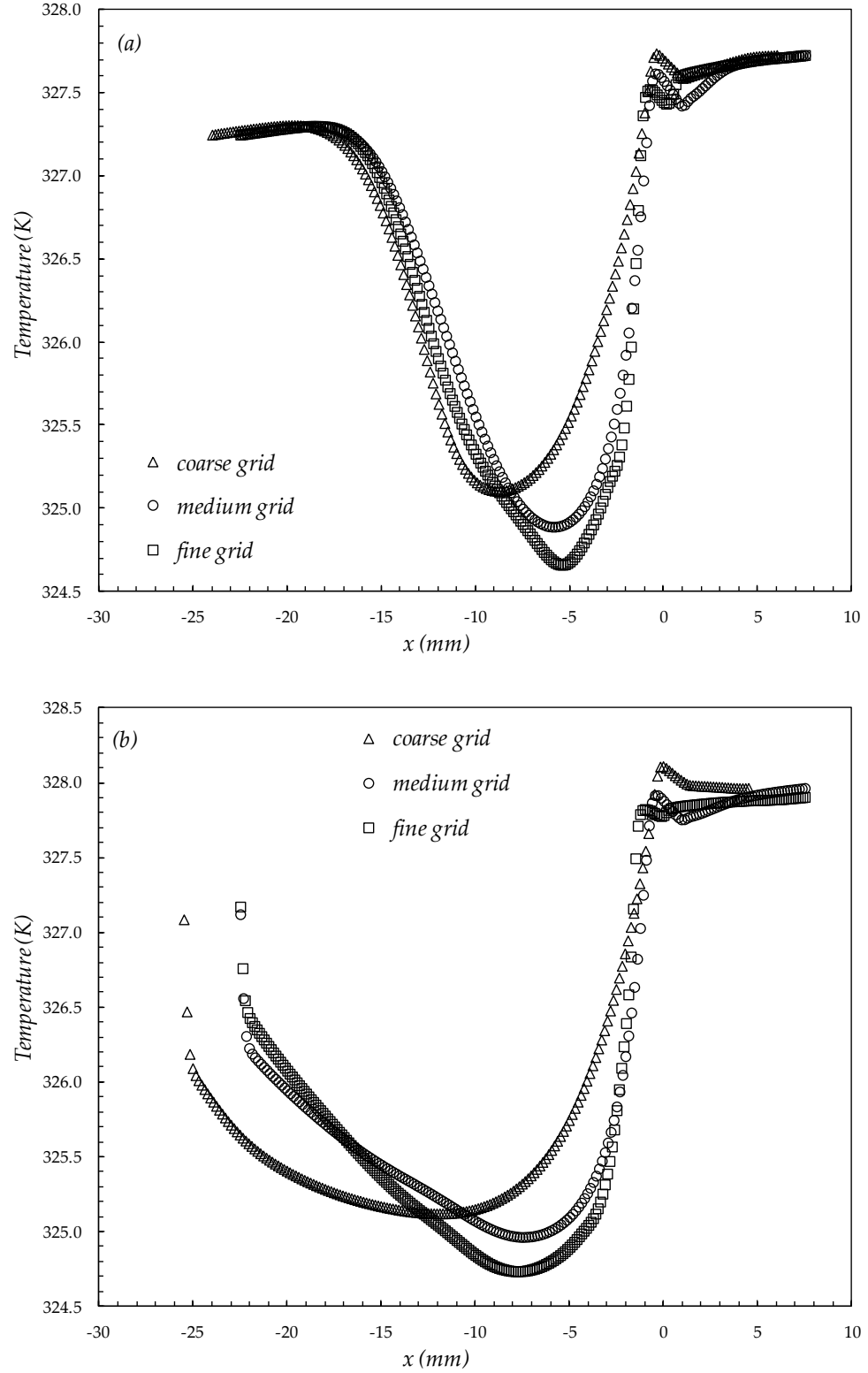


Figure 5.3 Grid independence test on temperature distribution of the heated wall during HS run at (a) $t^* = 0.5$, where the coarse grid curve is shifted 1.5 mm to the left and (b) $t^* = 1$, where the coarse grid curve is shifted 3 mm to the left.

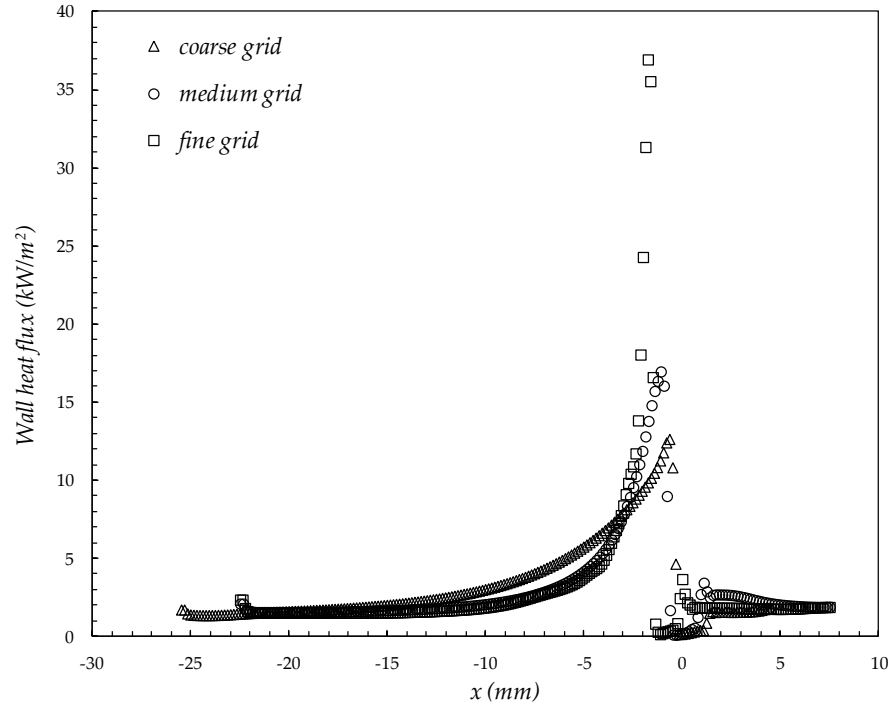


Figure 5.4 Grid sensitivity check for heat flux distribution of the heated wall for the HS run at $t^* = 1$.

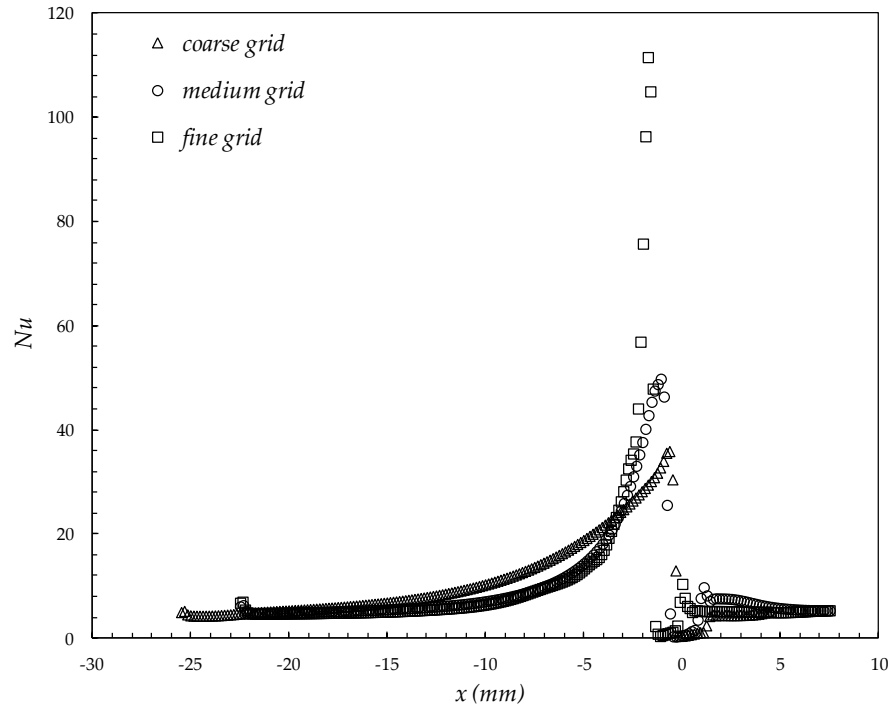


Figure 5.5 Grid convergence for Nusselt number distribution of the heated wall for the HS run at $t^* = 1$.

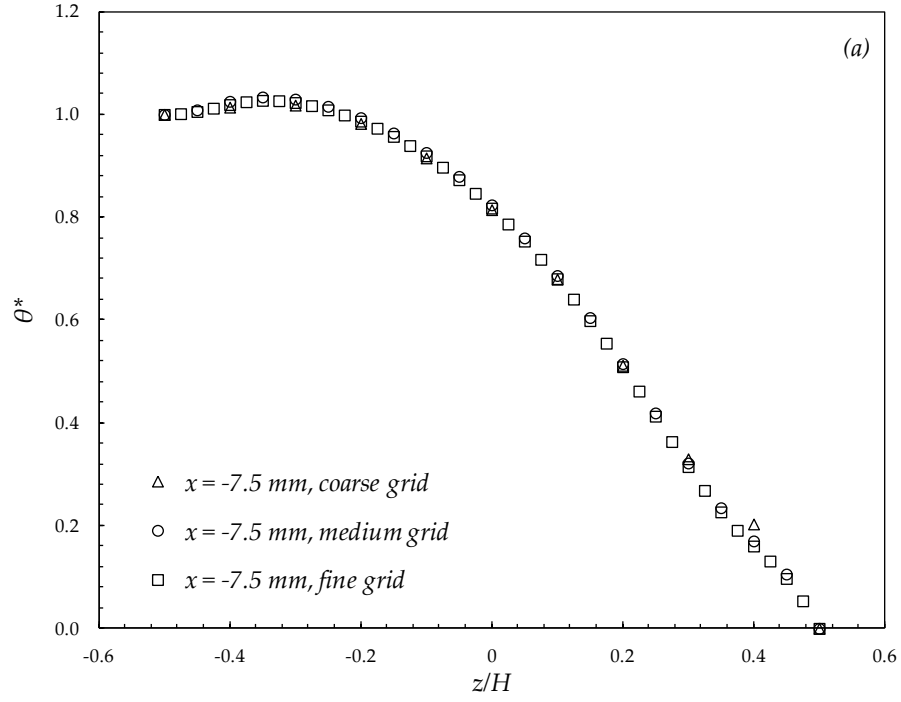


Figure 5.6 (a) Grid convergence for the fluid temperature during HS run at $x = -7.5$ mm ($t^* = 0.5$).

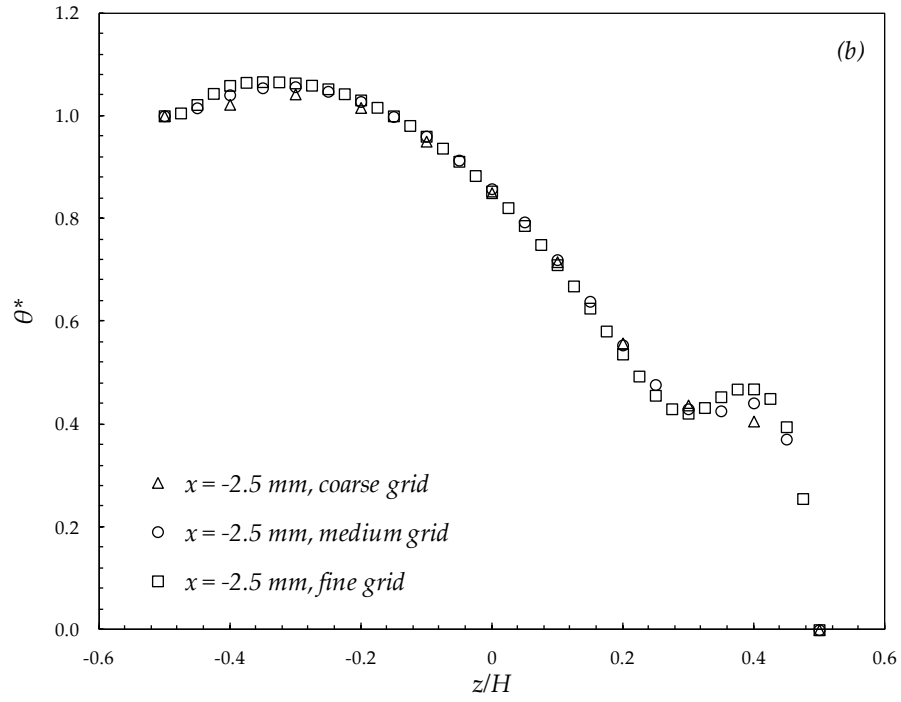


Figure 5.6 (b) Grid convergence for the fluid temperature during HS run at $x = -2.5$ mm ($t^* = 0.5$).

At $x = -7.5 \text{ mm}$, in Figure 5.6 (a), all the three grids agree due to negligible change in the centerline temperature in the far-field of the bubble early in the relaxation process at $t^* = 0.5$. The centerline temperature at $x = -2.5 \text{ mm}$ (1.75 mm behind the surface of the bubble) is similar in shape for the medium and fine grids, but the coarse grid fails to capture the large temperature drop near the heated wall. Based on the results of the grid sensitivity tests and the current availability of the computational resources, the medium grid was chosen for all simulations.

Figure 5.7 demonstrates the development of the centerline temperature in the near field and the far field of the bubble as the solution relaxes from the initial condition. This result shows that there is a significant near-wall change as the solution relaxes between $t^* = 1$ and $t^* = 5$.

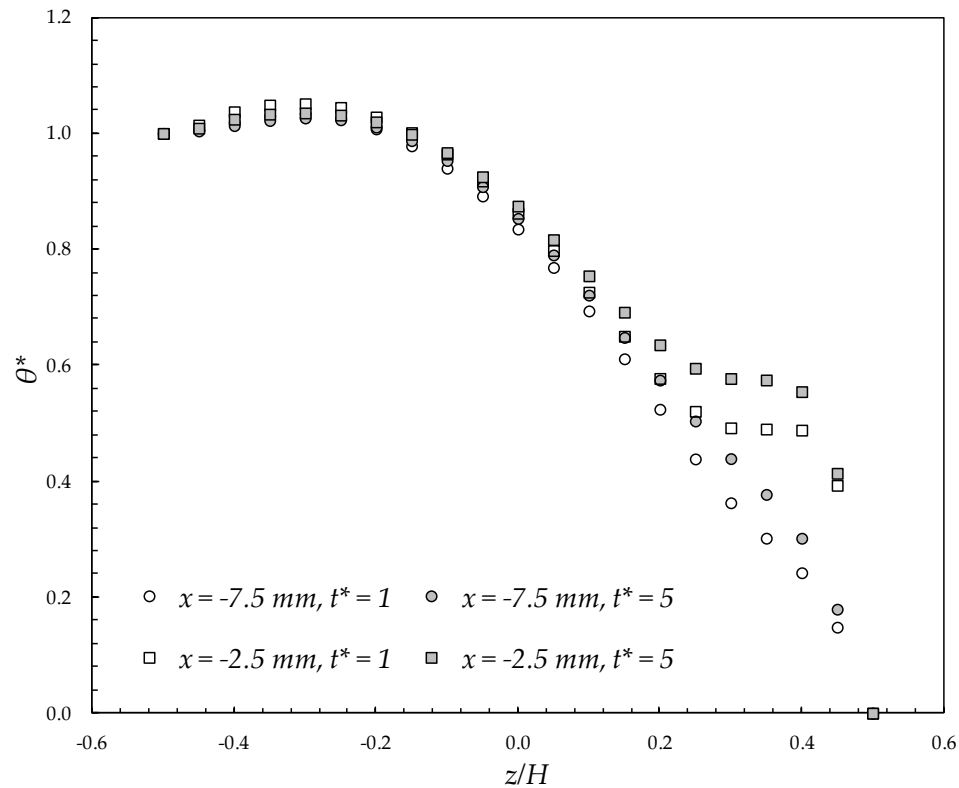


Figure 5.7 Centerline fluid temperature profiles in the near-field and far-field of the bubble at two different t^* values for the medium grid.

Time convergence was tested for time steps of 0.3409, 0.17045 and 0.0852 ms over a time span in which the heated plate traverses one-fourth of the channel length in the moving reference frame. Figure 5.8 shows the temperature profiles varying with the distance from the heated wall for three different time steps during a medium-grid HS run. A time step of $\Delta t = 0.1705\ ms$ was selected.

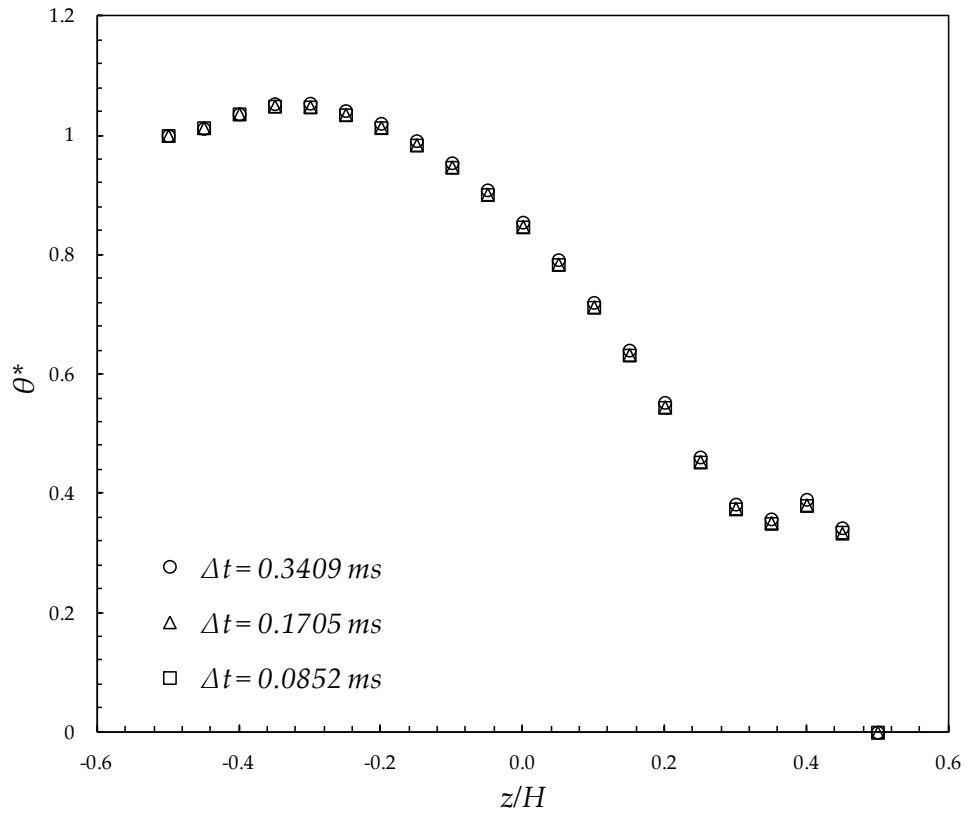


Figure 5.8 Time sensitivity test for the medium grid during HS run: dimensionless temperature profile at $x = -2.5\ mm$ and $t^* = 0.25$.

Figure 5.9 shows the wall heat flux distribution at the centerline of the channel at different computational times as the solution relaxes. After $t^* = 3$ the distribution tend to overlap each other, confirming that the solution exhibits convergence.

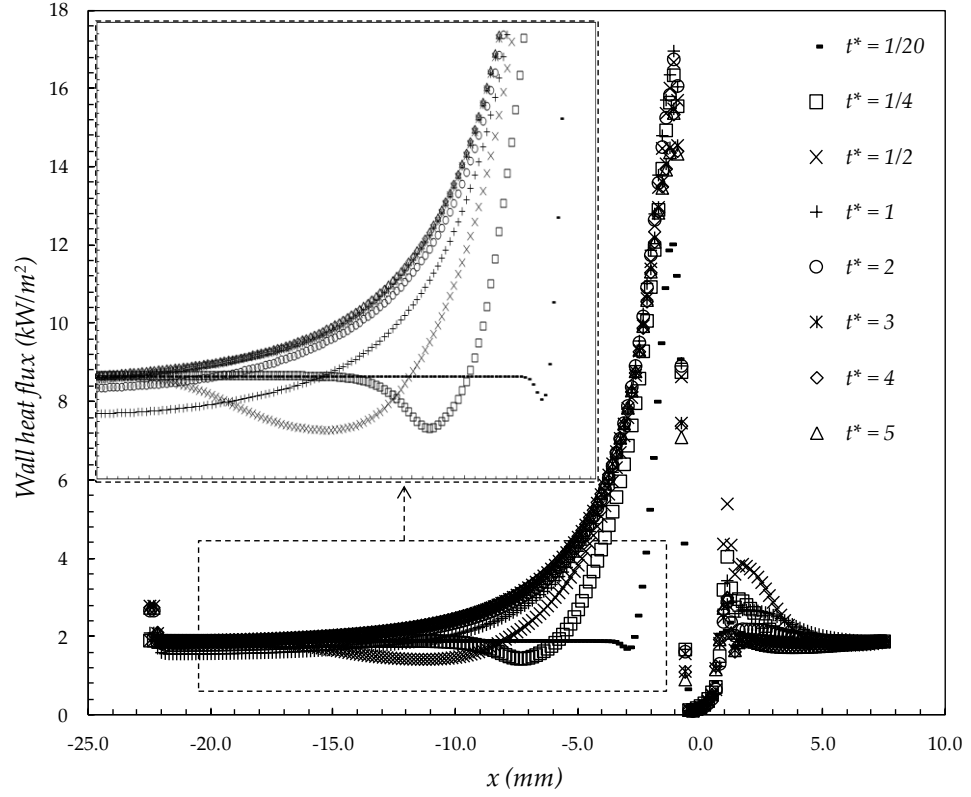


Figure 5.9 Heat flux distribution along the centerline of the heated wall versus x -direction at different computational times.

Similarly, Figure 5.10 shows convergence of the streamwise velocity distribution in the near field of the bubble ($x = -2.5$ mm) to a shape that is very close to the streamwise velocity profile expected for the undisturbed precursor flow. Negligible variation in time is observed, suggesting that streamwise velocity changes are strongly localized near the bubble (within 2 mm from the surface of the bubble).

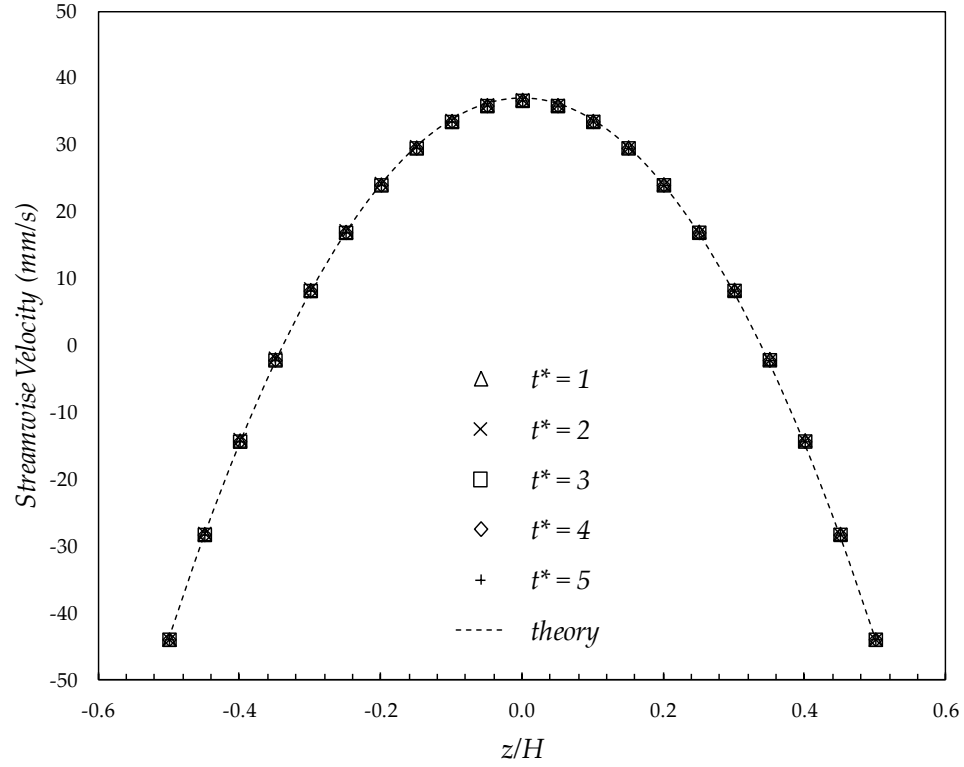


Figure 5.10 Distribution of the streamwise velocity across the channel at the channel centerline at $x = -2.5$ mm.

5.2 EFFECT OF BUBBLE VELOCITY

Figures 5.11 (a) and (b) show the streamwise evolution of the driving temperature difference along the centerline of the channel. In Figure 5.11 (b), the term $(T_w - T_m)_{undisturbed}$ represents the temperature difference between the wall and the bulk fluid in the absence of the bubble (for the precursor flow). A dimensionless distance is introduced in that figure to study the influence of the bubble velocity on the depression observed on the wall temperature plots and is expressed as

$$x^* = \frac{x}{Pe D_h}. \quad (5.4)$$

This dimensionless distance also represents the ratio of the convective and the diffusive time scales for this flow. Figure 5.11 (a) shows the difference in the centerline wall temperature

evolution for the LS and HS cases. For the HS case, the driving temperature difference decreases moderately and then recovers very slowly as the near-wall fluid is convected downstream (to the left). The curve does not recover the enforced boundary value before reaching the left end of the domain. On the other hand, for the LS case, the depression of the temperature difference is much steeper and the recovery is much faster than that of the HS case, although this curve also fails to recover fully before reaching the left boundary of the channel. The minima of the temperature difference occur at a distance of $5D$ and $3D$ to the left from the center of the domain for HS and LS cases respectively. Figure 5.11 (b) shows that the two curves are very similar when scaled on the precursor temperature difference and x^* . There is only a single diffusivity here, so the inference that the Péclet number is the proper scale cannot be tested. Given that x^* is the natural distance scale for the development of a laminar thermal layer in a hydrodynamically fully developed channel flow, the fact that these curves collapse may indicate that the affect of the bubble passage is similar to the initiation of a new thermal boundary layer from the rear of the bubble that develops downstream (to the left) of the bubble.

Figure 5.12 shows the variation of wall heat flux and Figure 5.13 shows the distribution of Nu along the channel. Higher heat flux values are predicted by the HS case than the LS case. The heat flux and Nu variations along the channel are very similar in nature due to very low depression (up to only 3 degrees) observed in the heated wall temperature distribution, as discussed previously. The numerically computed values for Nu are compared to the analytical solution obtained by Heaton et al. (1964) for the precursor flow. The maxima on the Nu -curves along the center-line of the heated wall for HS and LS cases are recorded to be nearly eight times the value for fully developed flow between two parallel plates. This enhancement is not the highest on the surface and the maxima of Nu are seen 1 mm to the left of the center of the bubble (on the lines $y = \pm 0.3\text{ mm}$).

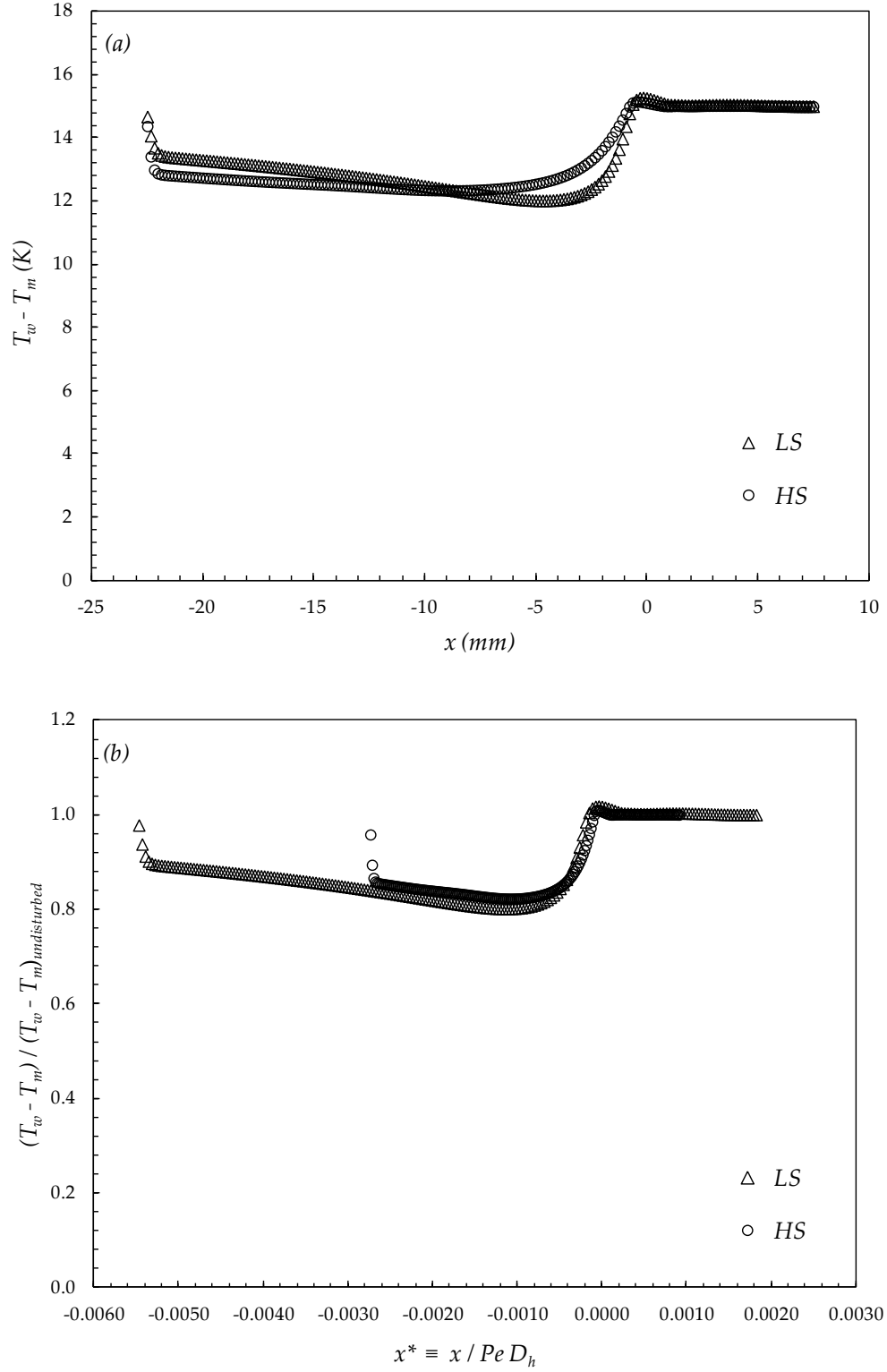


Figure 5.11 Plots of (a) driving temperature difference against streamwise position and (b) non-dimensional driving temperature difference versus x^* , for LS and HS runs at $t^* = 3$.

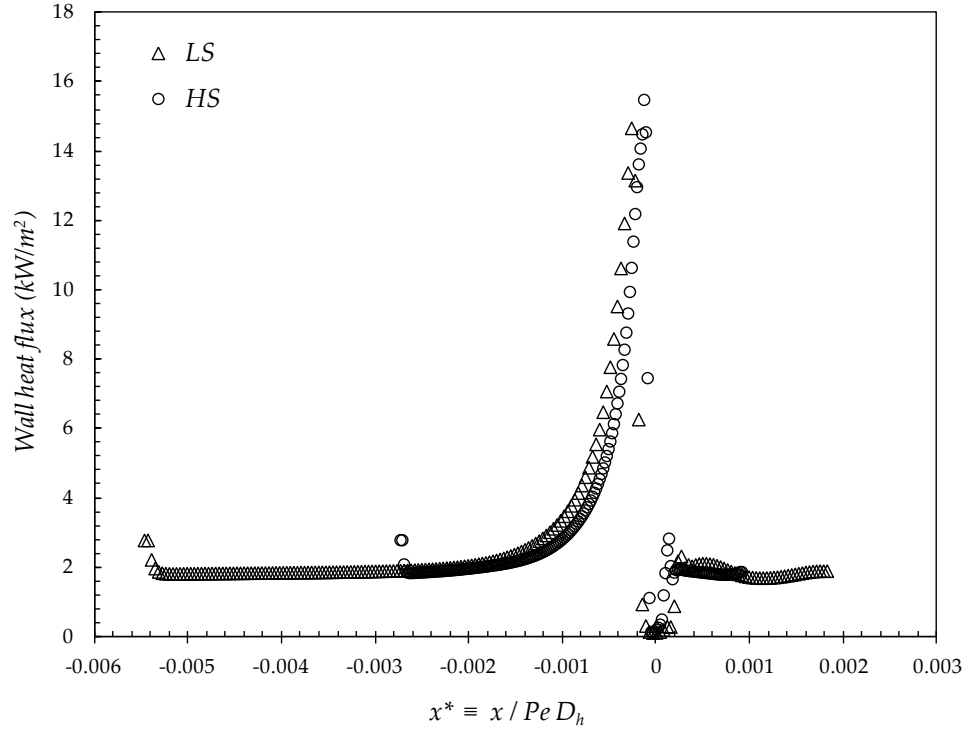


Figure 5.12 Wall heat flux distribution against normalized streamwise position comparing HS and LS runs at $t^* = 3$.

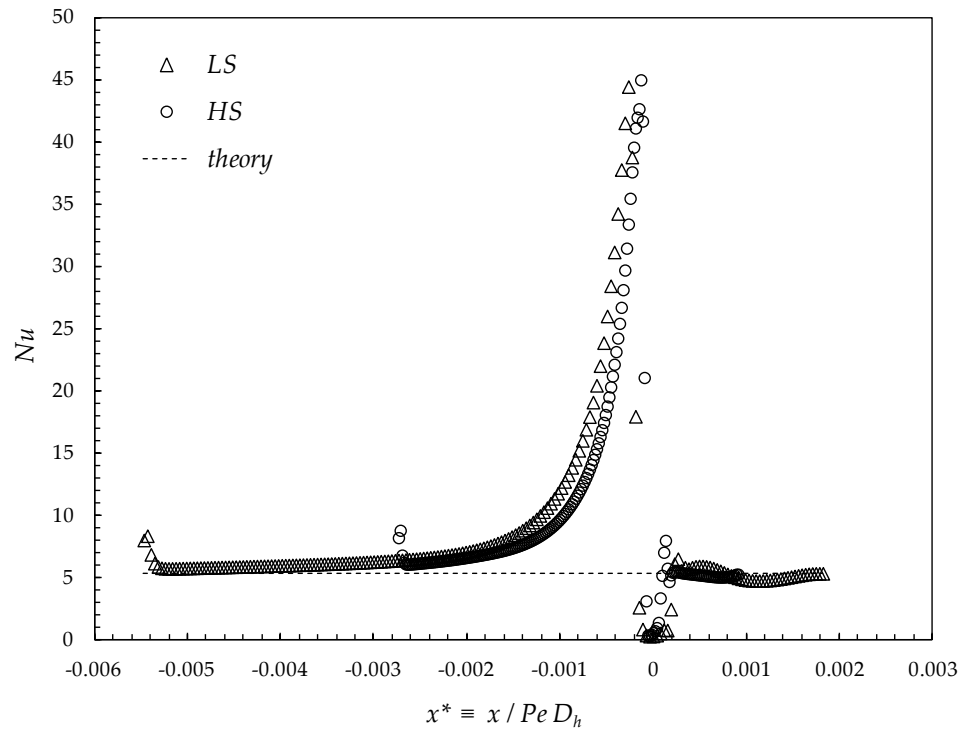


Figure 5.13 Nu distribution versus normalized streamwise direction for HS and LS cases at $t^* = 3$.

5.3 WALL HEAT TRANSFER

Figure 5.14 and Figure 5.15 show the initialized temperature inside the plate and initialized phase volume fraction in the x - y symmetrical plane respectively.

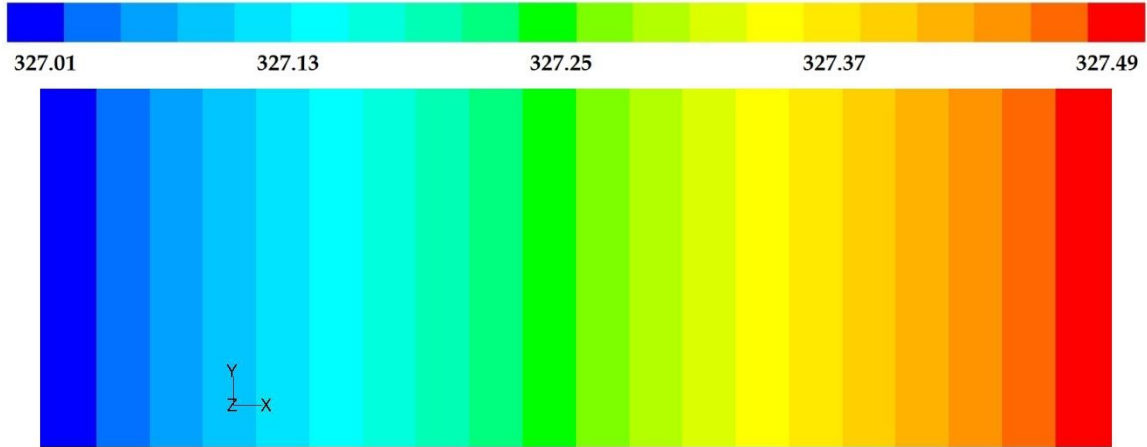


Figure 5.14 Node values of temperature of the heated plate at initialization with $T_{iw} = 327$ K.

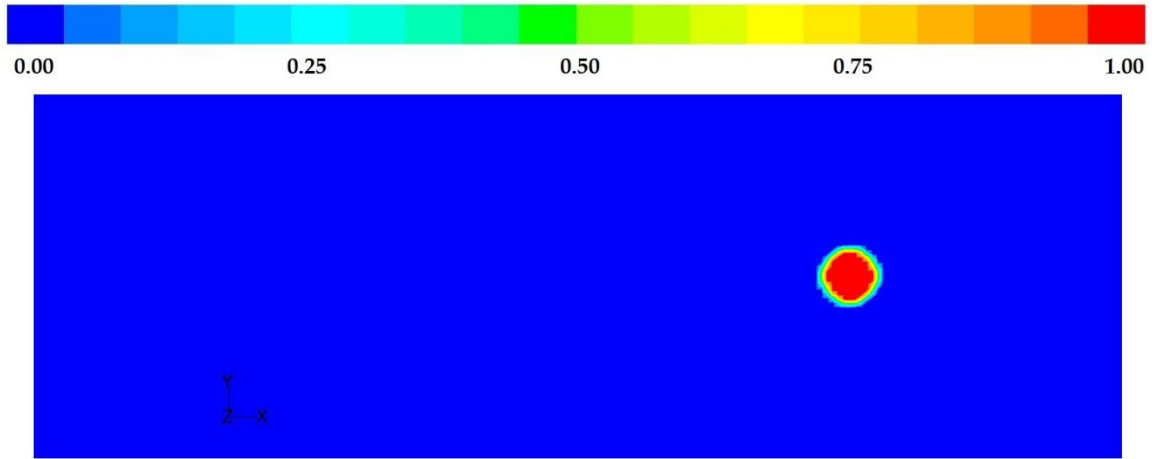


Figure 5.15 Node values of volume fraction of the vapor phase in the symmetrical x - y plane at initialization.

The plate is initialized with a volumetric heat generation rate, a velocity relative to the moving reference frame and a temperature profile linearly increasing with flow time from the left edge of the domain. Likewise, the fluid domain is initialized with fully-developed velocity and

temperature distributions as derived in the third chapter. A vapor bubble of 1.5 mm diameter under saturation conditions is also ‘patched’ inside the fluid domain and its initial location is chosen such that there is enough domain space to analyze the flow and heat transfer activity downstream (to the left) of the bubble.

Figure 5.16 illustrates the two-dimensional surface heat flux contours for the HS case at the most developed stage of the computation ($t^* = 5$). A two-lobed structure is apparent 1 mm downstream of the center of the bubble and 0.3 mm from the wall-centerline in both y -directions. It is observed that heat flux at the center of these two lobes lie in the range of 20 - 20.42 kW/m², nearly ten times that of the precursor value. A pair of similar in kind but relatively weaker spots is observed 1 mm upstream of the bubble. These two pairs on either side of the bubble are attached to each other by a horseshoe-like structure wrapping around the shoulders of the bubble; recording relatively lower heat flux values than the downstream lobe structures. Although the high heat flux is quite localized, its effect is prominent even in the far-field of the bubble as the elongated profile shape extends out to either ends and near the side-walls of the computational domain.

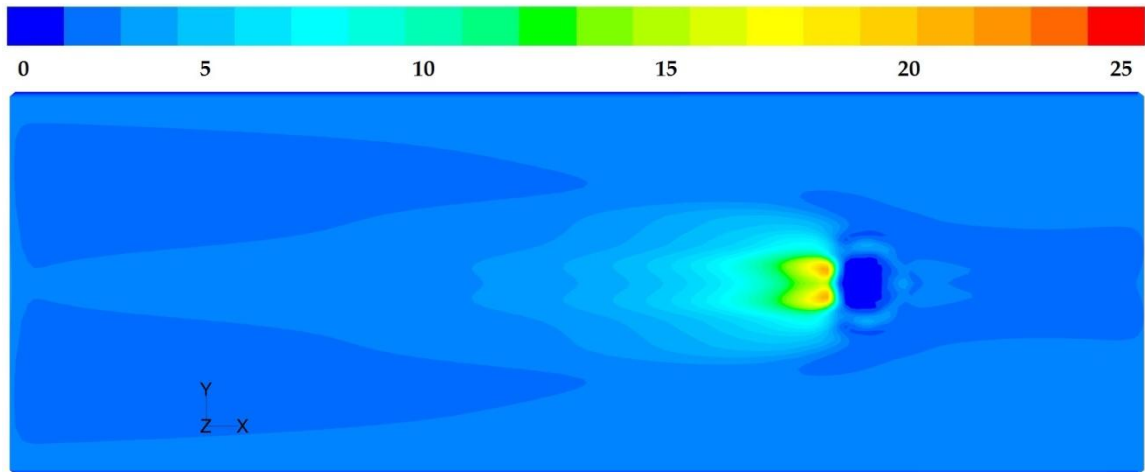


Figure 5.16 Contours of surface heat flux (kW/m²) on the heated wall for HS run at $t^* = 5$.

On the two-dimensional surface temperature plot in Figure 5.17, it can be seen that the contour lines are closer in the near-field of the bubble but farther apart in the far-field of the bubble. The most striking feature of this figure is the nonconformity of the wall-temperature distribution with the heat flux plot to register two cold spots to the left of the bubble. The highest amount of wall temperature depression is seen about four to five bubble diameters to the left of the downstream face of the bubble, and not at the high heat flux regions. The reason for this behavior is justified by calculating the thermal time constant for the plate.

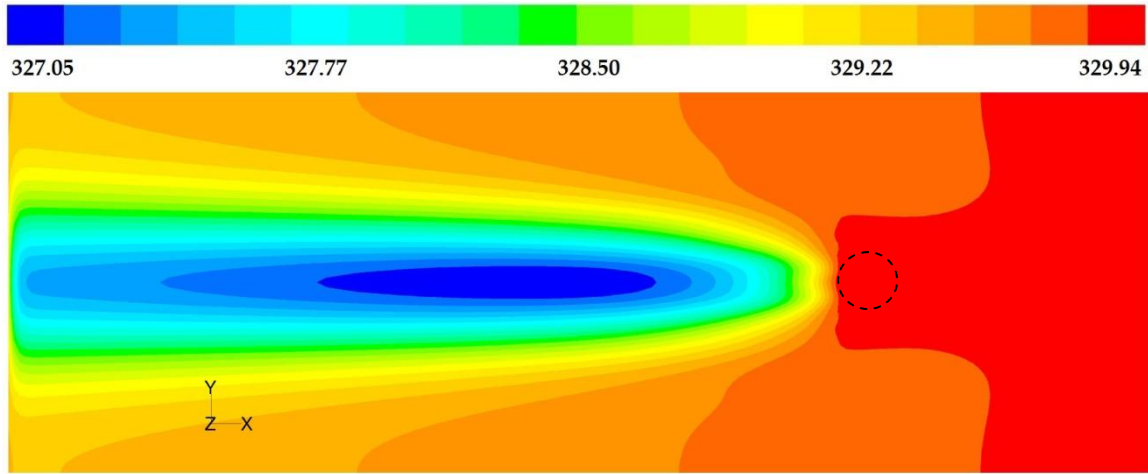


Figure 5.17 Contours of wall temperature (K) on the heated wall for HS case at $t^* = 5$. The location of the bubble interface on the heated wall is depicted by a dashed line.

The rate of temperature change of the plate is related to the velocity, dimensions and the intrinsic material properties of the plate by

$$\tau_c = \frac{\rho_s C_{ps} V_s}{h A_{surface}}, \quad (5.5)$$

$$\tau_c = \frac{8970 \frac{kg}{m^3} * 397 \frac{J}{kg K} * 0.03 m * 0.01 m * 0.000075 m}{127 \frac{W}{m^2 K} * 0.03 m * 0.01 m} = 2.103 \text{ seconds.} \quad (5.6)$$

For a plate of $75\ \mu\text{m}$ thickness, a time constant of 2.103 seconds is huge. The low thermal conductivity of 3M™ Novec™ 649 is a key factor for such a large thermal time constant. The thermal conductivity of the fluid (k) is present in the heat transfer coefficient term (h) in Equation 5.5 through the expression given by Equation 3.5. This expression relates k and h with the precursor Nusselt number. In the HS case the plate travels at $44\ \text{mm/s}$ and hence covers $94\ \text{mm}$ in one thermal time constant. This time-lagging response of the plate to any thermal changes in the fluid causes the temperature drop to extend out of the left side of the domain; with the computational domain being only $30\ \text{mm}$ in length. The same phenomenon is observed in the LS case as well but the plate responds quickly to the changes in the fluid temperature because the plate velocity decreases twofold.

An array of contour plots in Figure 5.18 show the evolution of surface heat flux (left column) and static temperature (right column) on the heated wall for the HS run. These contours show that the interaction of the approaching flow and the bubble can have a significant impact on the wall heat flux. At an early stage of the computation, two small high heat flux regions start to appear to the left of the bubble on the heat flux contour. From $t^* = 0.125$ to $t^* = 0.25$, the maximum heat flux at the center of these spots keeps increasing and the maximum temperature drop on the wall keeps shifting towards the left. At $t^* = 0.5$, a distinct structure appears on the heat flux plot upstream of the bubble while the temperature of the wall gradually decreases downstream (to the left) of the bubble, with the largest temperature drop observed around three bubble diameters downstream of the bubble. On the heat flux contour the horseshoe-like structure wraps around the bubble shoulders and the distinct thermal feature upstream of the bubble stretches towards the right as the heated plate moves towards the left. From $t^* = 1$ to $t^* = 3$, localized changes in the heat flux contour are observed in the vicinity of the bubble while the temperature drop starts to extend out of the left side of the computational domain, reason for which has been discussed

earlier. The heat flux and temperature fields are symmetric about plane $y = 0$ and variations in the heat flux and temperature are apparent in the transverse (y) direction. Comparing $t^* = 4$ and $t^* = 5$, negligible changes are observed in both heat flux and temperature contour plots between these time intervals. However, animations of wall temperature contours suggest that after $t^* = 3$, the temperature contours start to oscillate in the x -direction with the region of the highest temperature drop moving back and forth along the length of the plate.

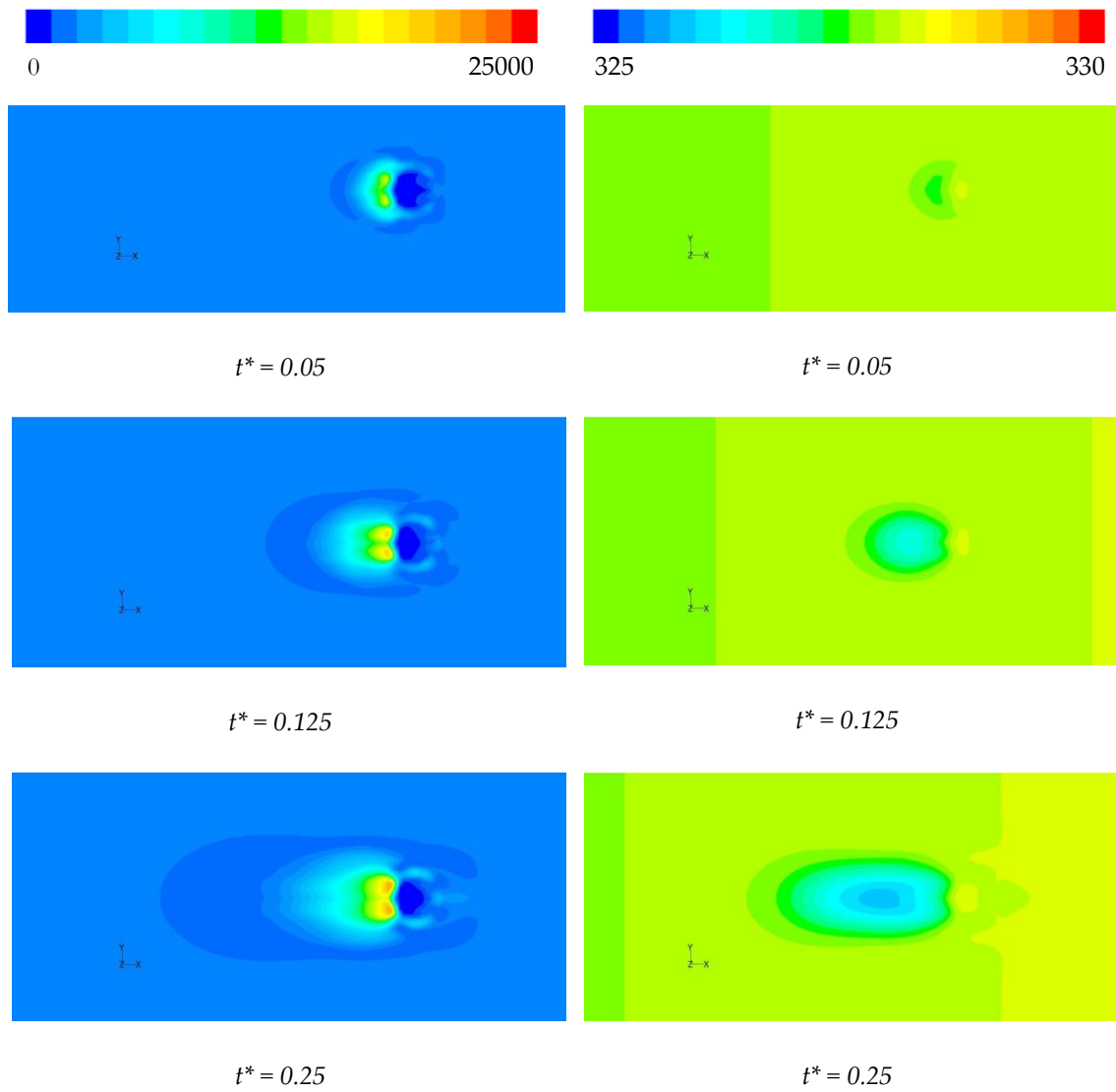


Figure 5.18 Temporal evolution of total surface heat flux (left) and temperature (right) on the heated wall for HS case. Range for heat flux and temperature is specified in W/m² and K respectively.

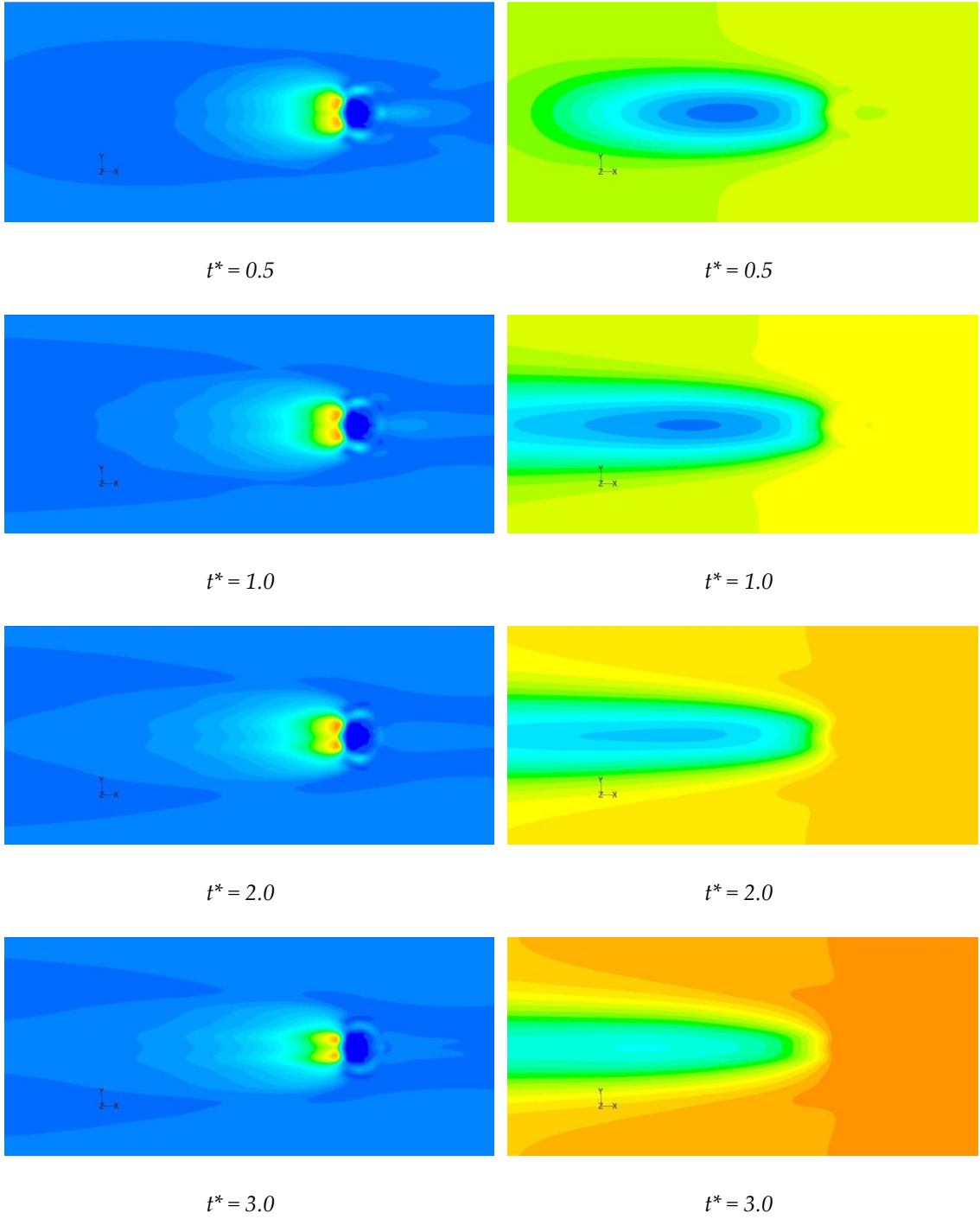


Figure 5.18 Temporal evolution of total surface heat flux (left) and temperature (right) on the heated wall for HS case. Range for heat flux and temperature is specified in W/m^2 and K respectively (continued).

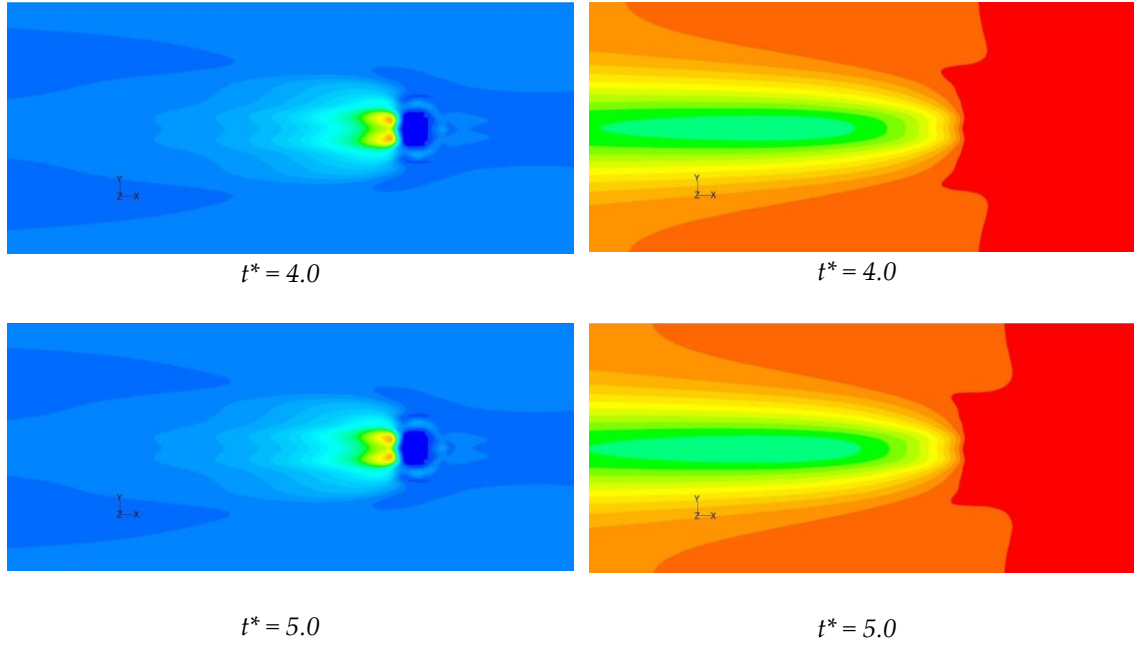


Figure 5.18 Temporal evolution of total surface heat flux (left) and temperature (right) on the heated wall for HS case. Range for heat flux and temperature is specified in W/m^2 and K respectively (continued).

The evolution of the wall heat transfer is correlated to the change in flow configuration in the vicinity of the bubble. Thus it is necessary to study the details of the flow structure around the bubble in relation to the features observed in the heat flux contours. Since areas of high heat flux are of practical importance, the next section is devoted to different mechanisms and flow events that result in regions of heat transfer enhancement.

5.4 FLOW STRUCTURE VISUALIZATION

The effect of the flow structure around the bubble on the wall heat transfer is examined to better understand the features observed on the wall heat flux and temperature contours. The first section illustrates the flow in terms of velocity vector plots and fluid temperature fields inside the channel. The second section confirms the flow model using vorticity fields.

5.4.1 Velocity vector plots

Figure 5.19 shows the line contours of the total surface heat flux on the heated wall along with the vapor phase contours (*bubble*) inside the channel. Five planes are chosen in the regions where the heat transfer enhancement is observed and heat flux values are nearly 10 - 12 times the precursor value. In addition to these planes, surfaces are arbitrarily created to aid in explanation of the flow structure.

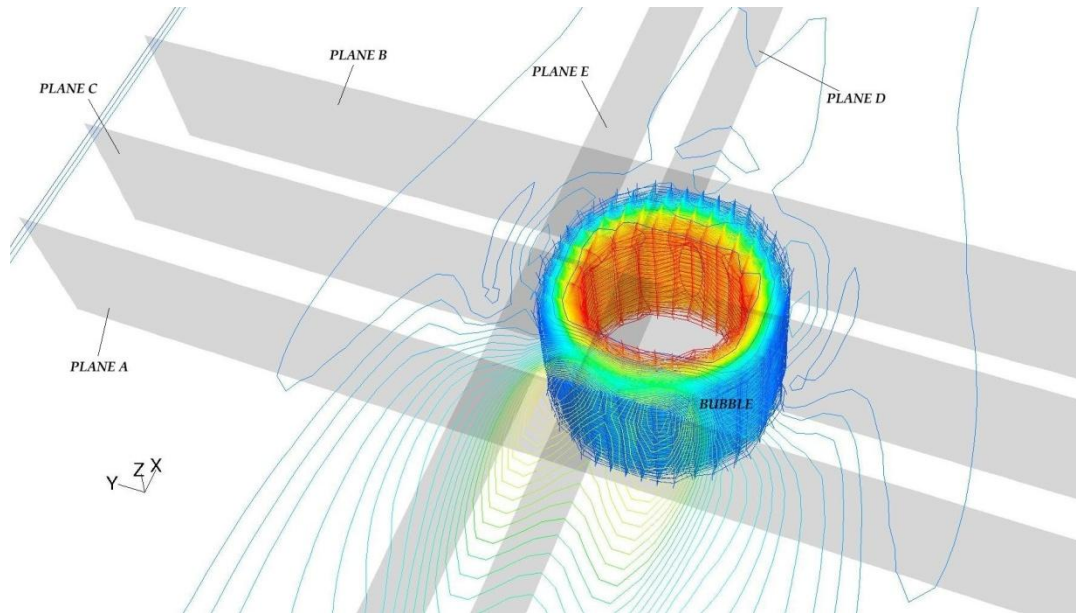


Figure 5.19 Isometric view illustrating the planes, Plane A ($x = -1$ mm), plane B ($x = 1$ mm), plane C ($x = 0$ mm), plane D ($y = 0.3$ mm) and plane E ($y = 1$ mm); created near areas of high heat transfer activity on the heated wall and overlaid with contours of vapor phase (bubble).

Plane A ($x = -1$ mm) intersects the two high heat flux spots in the cross-stream direction. Figure 5.20 shows the fluid temperature contours overlaid with velocity vectors lying in that plane. The red strip on the top of the plot represents the $75\ \mu\text{m}$ heated plate; and C1 and C2 are regions that indicate the positions of the two maxima (cold spots) observed on the wall heat flux contours. Noting that the precursor flow field would have zero y and z components of velocity,

the velocity vectors in this plane represent the y and z components of the velocity field perturbation due to the presence of the bubble. It is observed that below the cold spots the fluid in the middle of the channel approaches the bubble from the left, is decelerated by the presence of the bubble and flows laterally toward the channel walls. Above the center-plane, the fluid moves upward on either side of the centerline and approaches the plate surface near C1 and C2. Thus, colder fluid from below is transported towards the plate surface, increasing the local temperature gradients and resulting in the increased heat fluxes. The liquid temperature in the two cells next to the heated wall was noted to be in the range of 317 – 322 K, which is a temperature drop of nearly 5 -10 K with respect to the wall. In a U-shaped region between C1 and C2, near the center-plane of the channel, a relatively higher temperature is observed due to weaker motion of cold bulk liquid towards the wall.

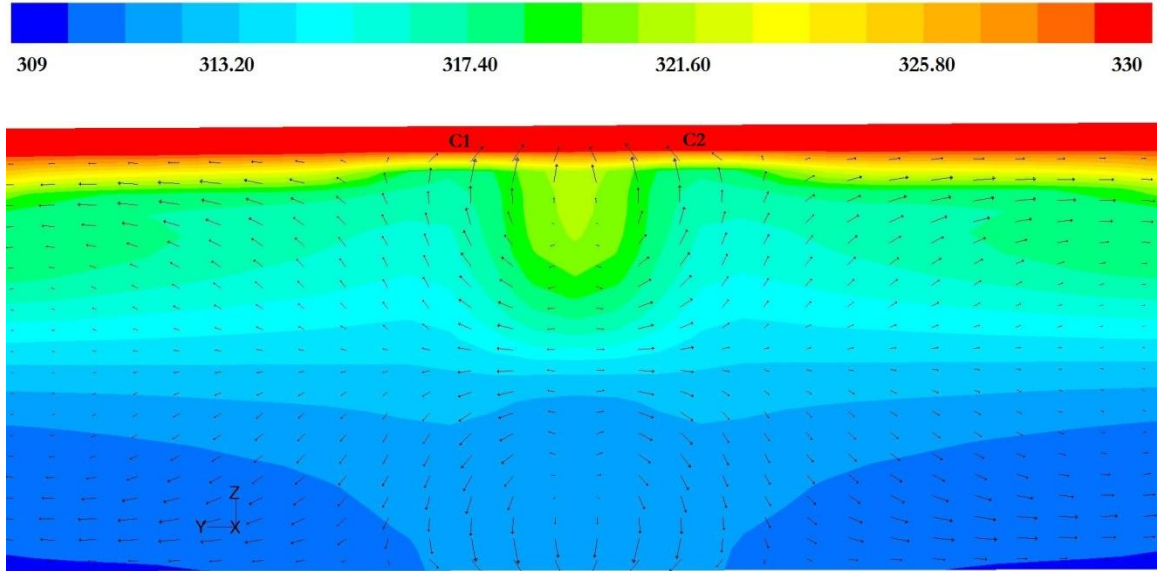


Figure 5.20 Fluid temperature overlaid with in-plane velocity vectors on plane A ($x = -1$ mm) to explain the formation of the high heat flux spots C1 and C2. Fluid in the center of the channel is flowing perpendicular to the page, inwards.

Similarly, 1 mm to the right of the center of the bubble a distinct thermal feature is observed in the wall heat flux contours, recording nearly twice the precursor heat flux value. Figure 5.21 explains that feature by showing plane B ($x = 1$ mm) depicted by fluid temperature contours and overlaid with velocity vectors in that plane. Contrary to what is observed in plane A, mixing of hot near-wall liquid, which is approaching the bubble from the right, and cold bulk liquid takes place in the center of the channel with the liquid near both top and bottom walls flowing towards the center of the channel. This mixing phenomenon spans nearly a bubble diameter in the y -direction. In addition to that, two pairs of counter-rotating swirls are observed on either half of the plane. It is discussed later that these swirls are streamwise vortices advected downstream, inducing bulk fluid mixing near the center of the channel.

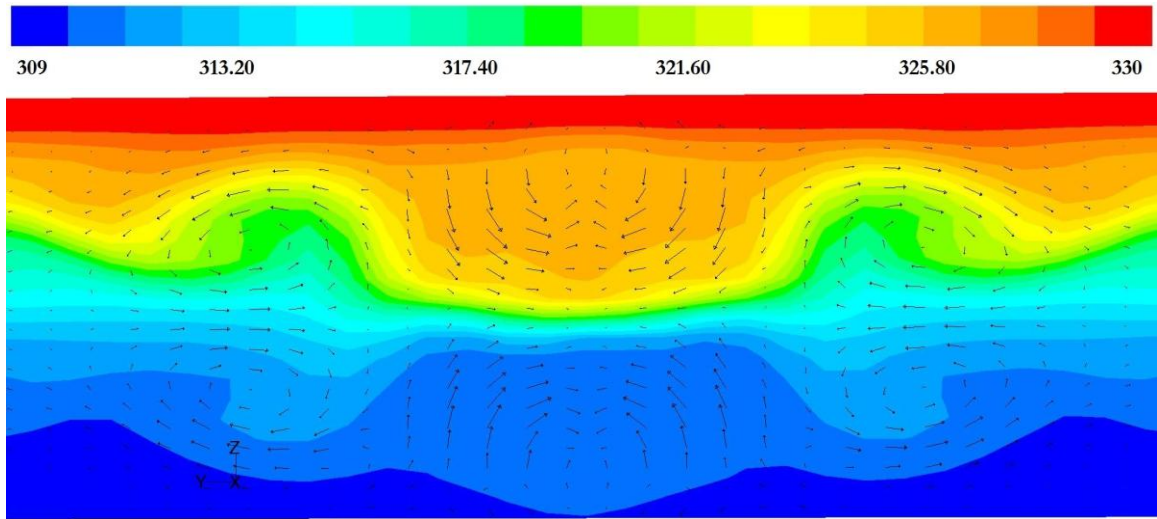


Figure 5.21 Fluid temperature overlaid with in-plane velocity vectors on plane B ($x = 1$ mm) to explain wall heat transfer upstream of the bubble. Fluid in the center of the channel is flowing perpendicular to the page, inwards.

Figure 5.22 depicts fluid temperature contours and velocity vector plots on plane C ($x = 0$ mm) to describe the influence of flow on the development of the thermal structure on the heat flux plot that wraps around the shoulders of the bubble. Vapor in the center of the bubble is

nearly stationary while closer to the bubble surface it has a high y -velocity component. This confirms the existence of a pair of counter-rotating vortices spanning the channel height inside the bubble, driven by the relative wall motion. On either side of the bubble and near the center of the channel, the accelerated fluid is directed towards the bubble surface. A strong vortex structure on the shoulders of the bubble could be causing such a motion. However, near the upper and lower walls, streamwise vortices (SV) are observed. It is seen later that these vortices are a part of the horseshoe-like vortex structure which wraps around the periphery of the bubble. Although these regions were not completely resolved with the current grid, it can be said that these fluid circulation phenomena enhance momentum exchange along the shoulders of the bubble.

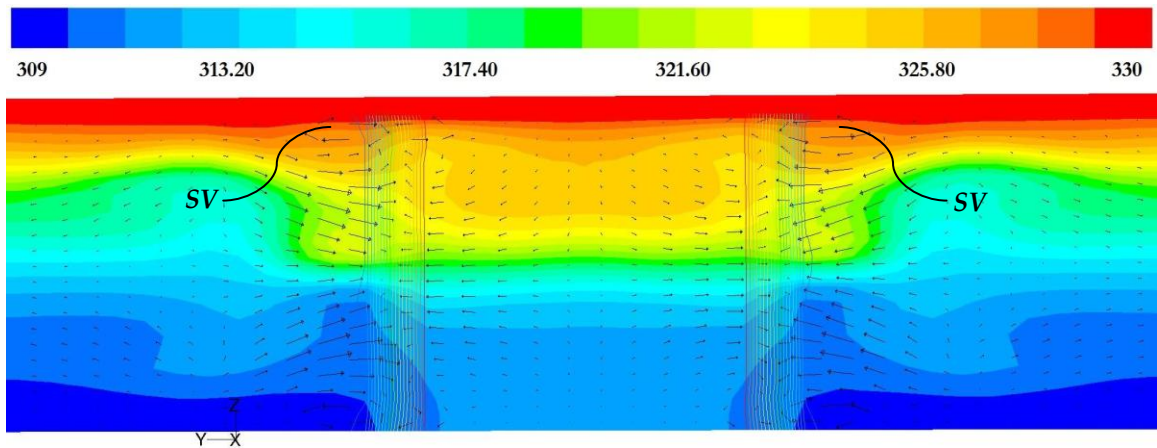


Figure 5.22 Fluid temperature overlaid with in-plane velocity vectors on plane C ($x = 0$ mm) to explain the thermal structure along the bubble shoulders. Fluid in the center is flowing perpendicular to the page, outwards.

Figure 5.23 shows fluid temperature, velocity vectors and vapor phase contours on plane D ($y = 0.3$ mm) to observe the influence of the bulk fluid motion to the left and right of the bubble. Around 0.25 mm to the left of the downstream surface of the bubble (outlined with a black oval-shaped region), a region of low temperature is observed and the temperature contour lines are

closely spaced. This was due to the in-rush of cold fluid from the core of the channel towards the wall, evident from the higher normal (z) velocity component at that point. As this fluid approaches the heated wall, a tiny vortex is observed within the boundary layer of the surface. Because this vortex is not properly resolved by the current grid the near-wall flow events are not discussed at length. Around 0.25 mm to the right of the upstream surface of the bubble, the same mixing phenomenon observed in Figure 5.21 is seen from the side view.

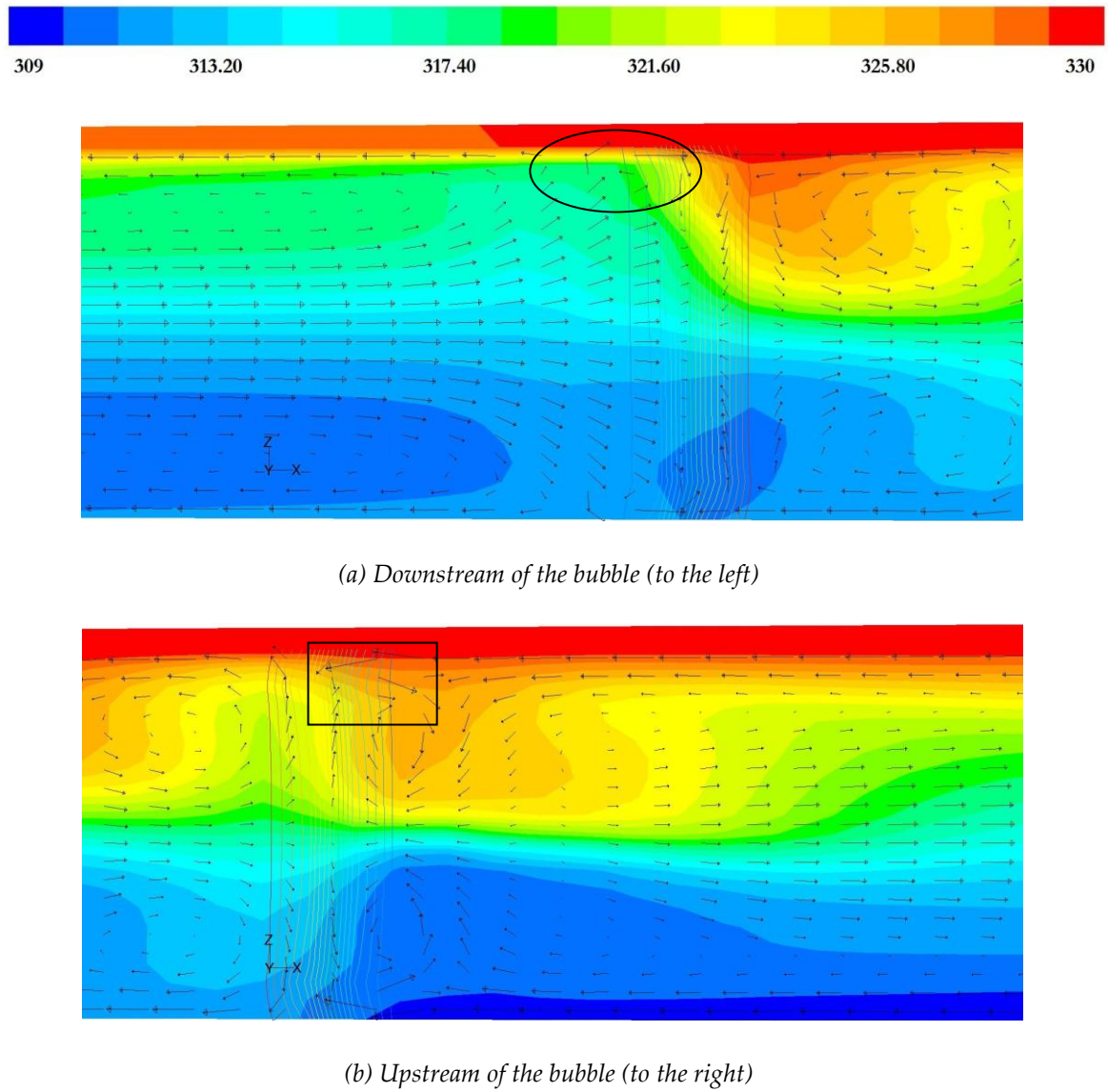


Figure 5.23 Fluid temperature overlaid with in-plane velocity vectors and line contours of vapor phase volume fraction on plane D ($y = 0.3\text{ mm}$).

A strong vortex is observed near the bubble interface on the top wall (outlined with a black rectangular region). As discussed later, the formation and the stretching of this vortex in all the three directions leads to the formation of a complex vortex system around the bubble. The isotherms are more widely spaced away from the bubble interface, resulting in a relatively lower heat transfer to the right of the bubble.

Figure 5.24 shows velocity vector plots tiled over the fluid temperature contours on plane E ($y = 1 \text{ mm}$). Since this plane does not intersect the bubble, the bubble is specified by transparent contours of vapor phase density in front of the plane. On the left side of the bubble, fluid from the center of the channel flows towards the heated wall and thins the boundary layer. To the right of the bubble the high temperature layer at the heated wall descends downwards and heads to the outer flow region. Mixing of fluid in the core of the channel and the near-wall hot fluid approaching from the right is observed near the center in the region of the bubble.

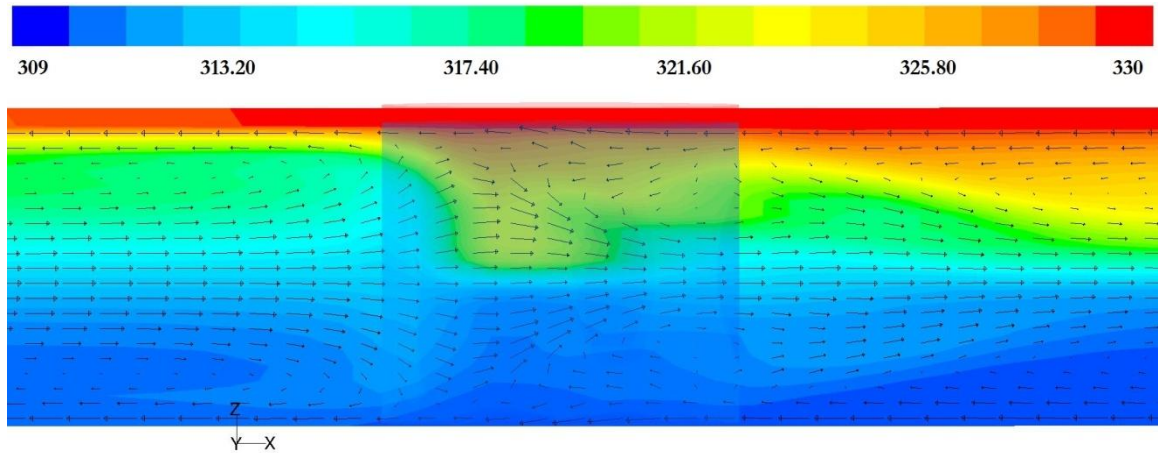


Figure 5.24 Fluid temperature overlaid with in-plane velocity vectors and transparent contours of vapor phase density on plane E ($y = 1 \text{ mm}$).

5.4.2 Vorticity fields

In this section, the influence of vortex dynamics around the bubble on the wall heat transfer is discussed by studying the vortex structures near the high heat flux regions. In doing

this, a better picture of the flow structure around the bubble is also obtained. Figure 5.25 shows a plot of vorticity magnitude tiled with velocity vectors at $y = 0 \text{ mm}$ (the transverse plane of symmetry). A pair of oppositely rotating vortices is visible near both top and bottom walls to the right of the bubble. A vortex (V1) rotating counter-clockwise forms on the heated wall and initiates the formation of a clockwise rotating vortex (V2) near the center of the channel. Although the near-wall regions have not been resolved properly with this grid, it is seen that V1 has a large y -vorticity component near the walls (also seen from the direction of the vectors) and forms due to the interaction between the near-wall fluid and the bubble surface in contact with the heated wall. To the left of the bubble, a strong vortex (with a high y -vorticity component) sits near the bubble-wall interface. This vortex induces mixing between the fluid near the wall advected from upstream and the bulk fluid downstream that impinges on the opposite walls.

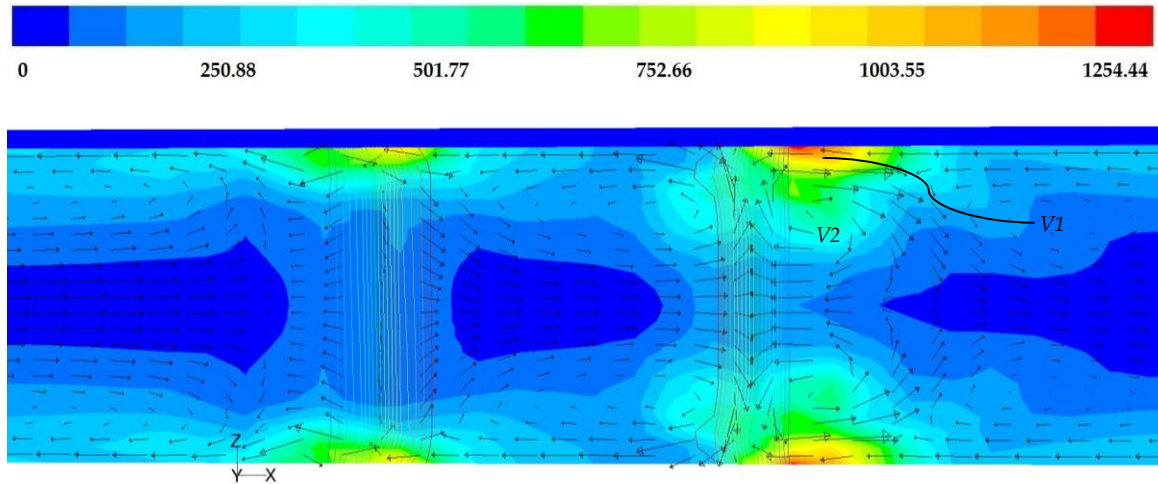


Figure 5.25 Contours of vorticity magnitude and velocity vector plots on the symmetry plane ($y = 0 \text{ mm}$).

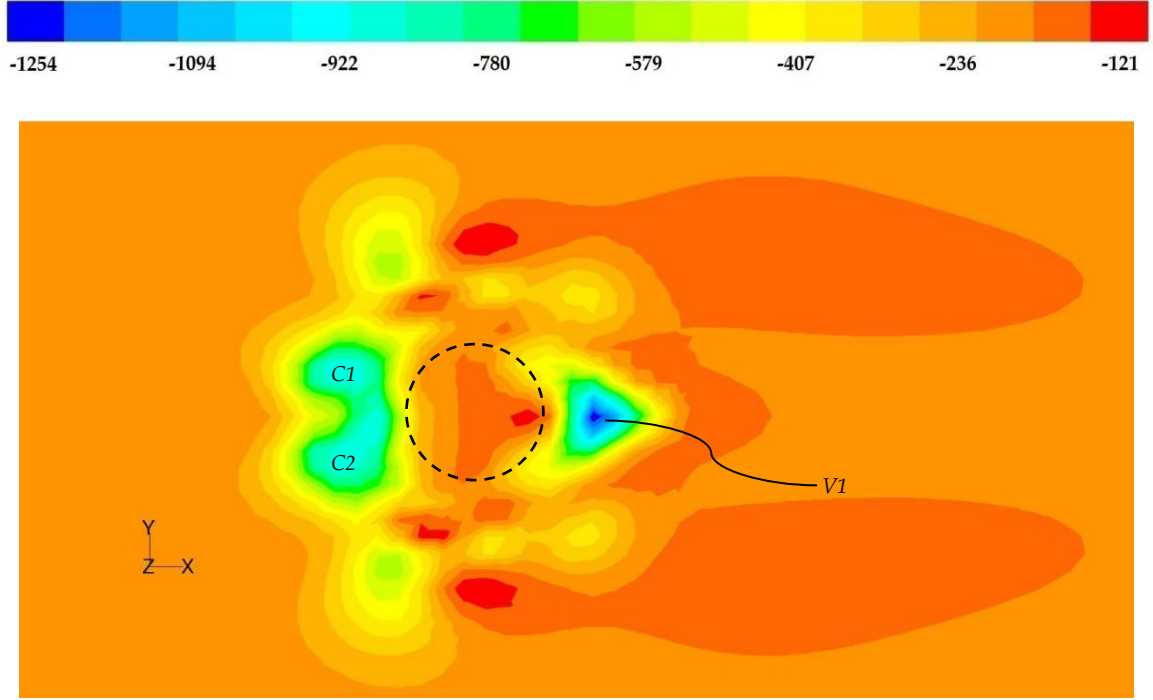


Figure 5.26 Transverse vorticity (y -axis) on the heated wall showing footprints of vortices to the left and right of the bubble.

Figures 5.27 (a) – (f) illustrate the contours of vorticity magnitude plotted at varying distances from the heated wall. The interaction between the flow and the bubble-wall interface upstream of the bubble occurs in a region of adverse pressure gradient. The fluid layer closer to the heated wall rolls up and forms a vortex (V1) that creates a V-shaped footprint on the heated wall, as shown in Figure 5.26.

This vortex is swept around the base of the bubble (on the heated wall) by the near-wall flow approaching from the right (upstream) and contains a large transverse (y -component) vorticity component. As it is convected downstream, it carries hot fluid and undergoes vortex-stretching in y -direction. Around the shoulders of the bubble, it is redirected into the streamwise direction. When it reaches the left (downstream) side of the bubble it forms two large cylindrical vortical structures to the left of the bubble in the z -direction. It is seen that C1 and C2 have large components of transverse (y -component) wall vorticity. This is a result of streamwise shoulder

vortices being redirected in y -direction. The shape of these oval-shaped footprints suggests the motion close to the wall being fluid moving inwards, as observed earlier in Figure 5.20. The method of fluid transport and mixing by these cylindrical structures is such that the hotter near-wall fluid flows towards the core of the channel and it is replaced by the upward movement of the colder bulk fluid. This mechanism influences the wall heat transfer dramatically by creating two spots of maximum heat flux on the heated wall. It is seen that before reaching C1 and C2 the fluid swirls around the cores S1 and S2. This motion of the flow also has a large influence on the wall heat transfer as the transverse variations on the heat flux contours span nearly a bubble width in both directions.

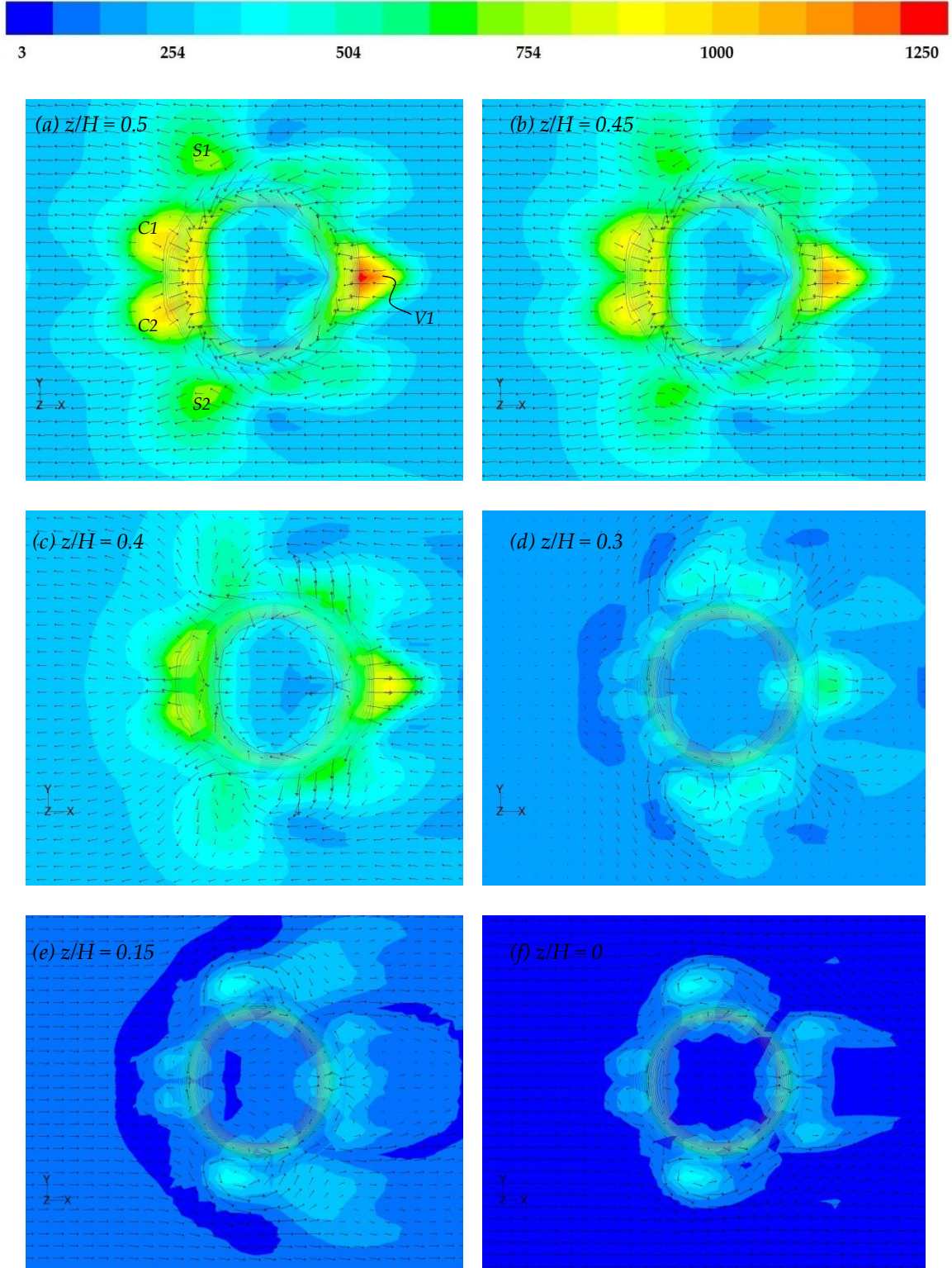


Figure 5.27 (a) – (f) Contours of vorticity magnitude and velocity vector plots at varying distances from the heated wall (HS run at $t^* = 5$).

Figure 5.28 (a) – (h) shows the stretching of the upstream vortex (V1) at different streamwise locations as it is convected downstream. It has to be noted that V1 has not been properly resolved in the z -direction. In these set of figures, contours of vorticity magnitude of the upper half of the channel is shown because only flow events closer to the heated wall are of practical significance. From figures (a) and (b), it is seen that the vortex V1, with considerable transverse vorticity strength, promotes circulation of fluid near the wall and the flow approaching the bubble from the right (upstream) stretches it in the y -direction. Additionally, the velocity vector field shows that there is significant z -component velocity along the surface of the bubble and a vortex V2 is present, as suggested by Figure 5.25. Figures (c) and (d) show the motion inside the bubble and vortices V3 and V4 on either side of the bubble roll up and are convected downstream by the flow accelerating around the bubble. These vortices carry significant streamwise vorticity. At the plane bisecting the bubble, $x = 0 \text{ mm}$, the vortices V3 and V4 persist due to the near-wall motion downstream. But the flow near the center of the channel moves upstream and figures (e) and (f) suggest that there is a large vortex structure presents along each side surface of the bubble. Figures (g) and (h) show that the streamwise vortices V3 and V4 lose their strength and meet at the center-plane of the channel ($y = 0 \text{ mm}$) in the form of two transverse vortices beneath C1 and C2. These two vortices (C1 and C2) are stretched and intensified in the z -direction and, in this way, exchange near-wall hotter fluid approaching from upstream with the colder fluid coming from the core of the channel downstream. The strong circulatory fluid motion inside these structures promotes high heat transfer on the wall and as mentioned earlier in this section, drives the formation of the two lobes observed on the wall heat flux contours.

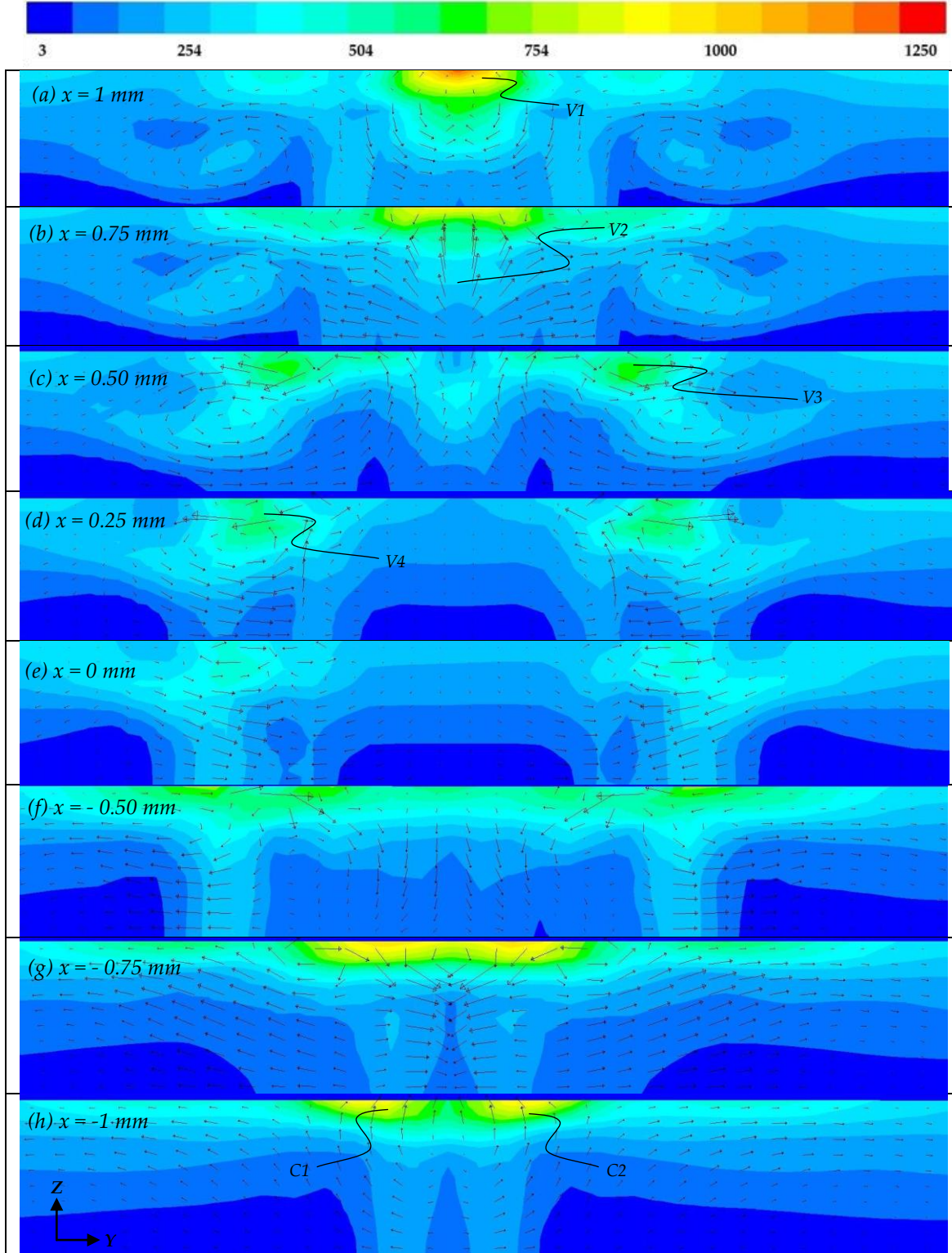


Figure 5.28 (a) – (h) Formation, stretching and the transport of the upstream vortex pair by the near-wall flow, visualized at different streamwise positions around the bubble (HS run at $t^* = 5$). The axis is same for all the contour plots.

Figure 5.29 (a) – (f) illustrates the complex three-dimensional vortex structures around the bubble by creating an iso-surface of vorticity magnitude ($\omega = 175 \text{ 1/s}$), *i.e.* about 14% of the absolute maximum in ω .

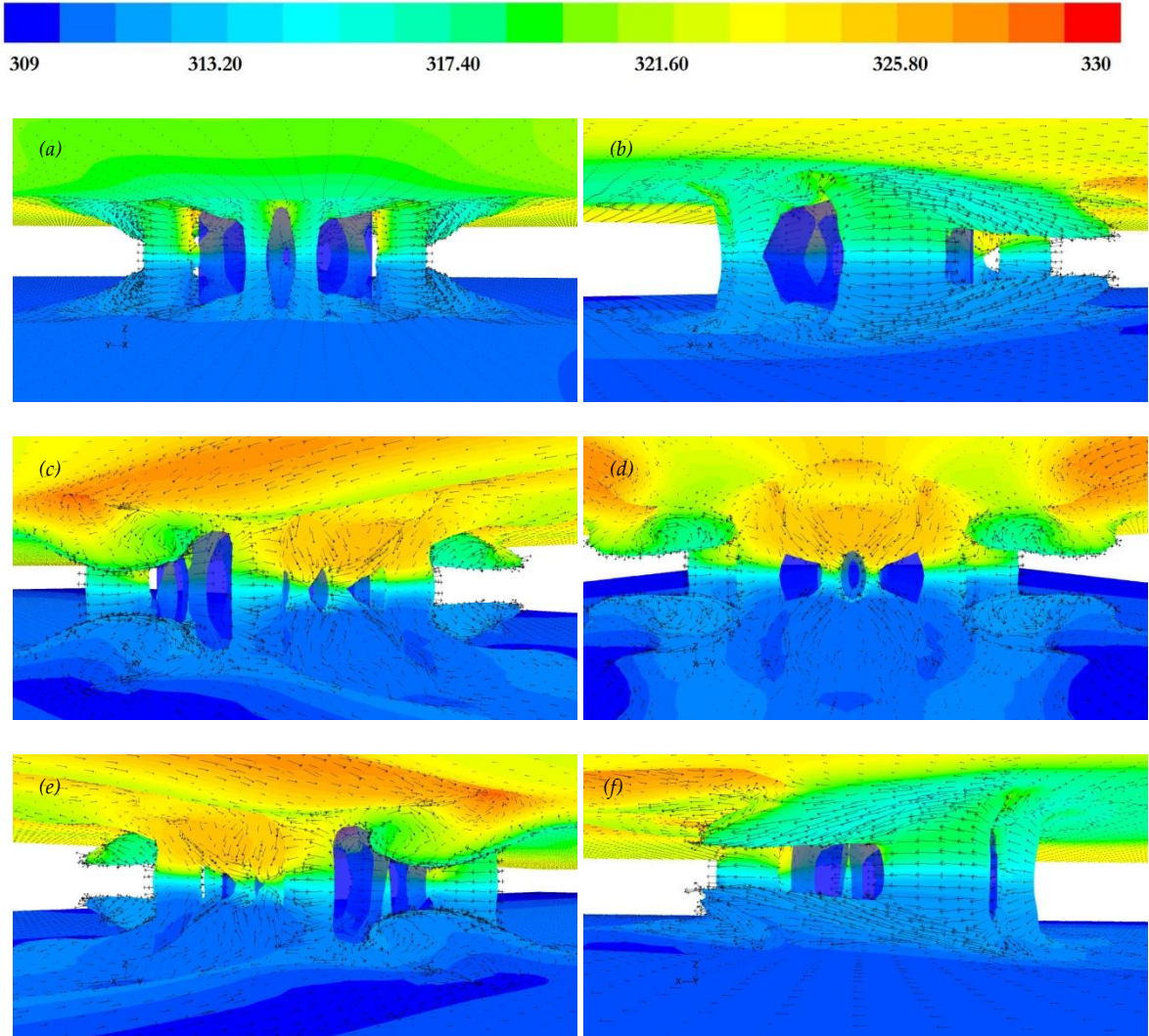


Figure 5.29 (a) – (f) Iso-surface of vorticity magnitude, $\omega = 175 \text{ 1/s}$ (HS run at $t^* = 5$). Contours are colored with temperature in the range shown above, over-laid with velocity vectors and the bubble is indicated by contours of vapor density (transparent blue).

The iso-surface is colored by fluid temperature to show the motion of cold bulk fluid towards the wall, in the form of two large structures beneath C1 and C2 downstream of the bubble. Figure

5.29 (a), showing a y - z plane view from downstream is rotated in the clockwise direction to view the vorticity field through other perspectives before reaching Figure 5.29 (f). The surfaces on the top and bottom shown in these images are not actual domain walls but are surfaces on which vorticity is constant. The structure is symmetric in the transverse direction and shows good agreement with the results presented regarding the flow in the earlier discussions.

5.5 WALL HEAT FLUX – TIME HISTORY

The secondary vortices induced by the flow around the bubble significantly increase the heat transfer from the heated surface. As time progresses and the heated surface slides over the bubble, the temperature and the heat flux of a point on the heated surface responds to the changes in the bulk liquid temperature and its motion.

Figure 5.30 shows a time-history plot of the heat flux of a point on the heated surface LS and HS cases. Instead of taking wall center-line values, a facet average of the total surface heat flux is computed over a width of $\pm 1.5 \text{ mm}$ on the heated wall at each streamwise location downstream of the bubble. The plots are compared with curves for three different mixed lengths from a simplified unsteady diffusion model proposed by Özer (2010): $0.21H$; $0.4H$ and H . The model considers that a uniform fluid temperature occurs over a certain distance from the heated surface due to the mixing associated with the quenching process and that distance is termed as the “mixed length”. This mixed length is a function of the bubble diameter, the frequency of bubble passage over the same surface location and the material properties of the liquid associated with diffusion. As a result of matching of the model results to his experiments, Özer found that mixed length varied from 15% to 50% of the channel height.

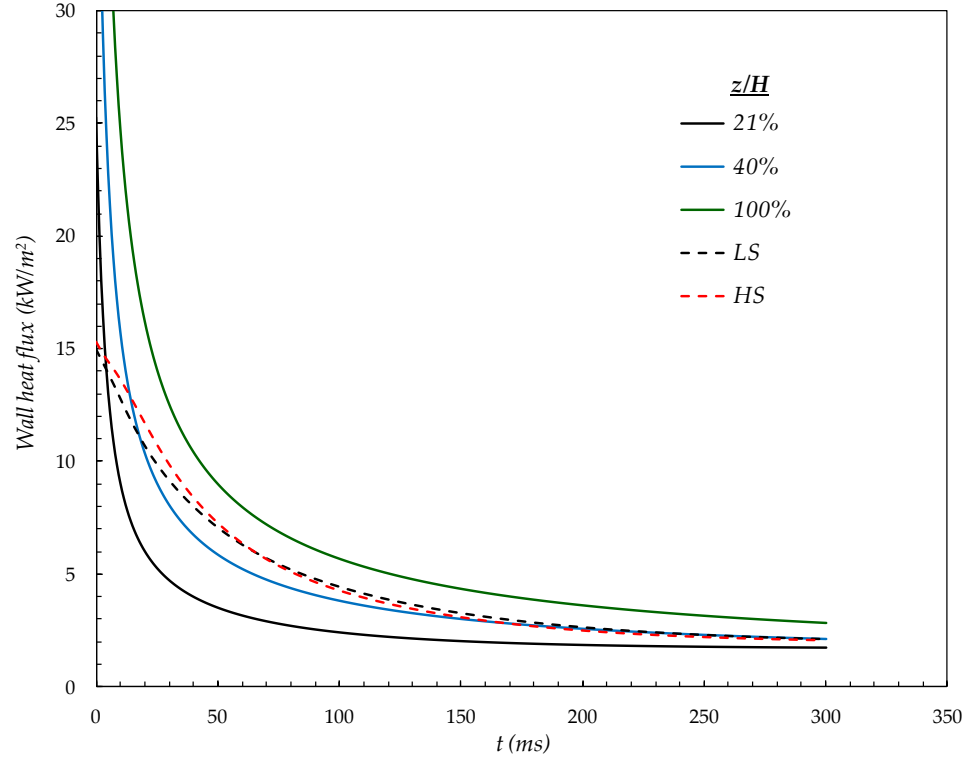


Figure 5.30 Time history of the wall heat flux of a point on the heated surface for LS and HS cases compared with Özer's (2010) quenching/diffusion model.

It is observed that the curves for LS and HS cases nearly overlap each other and are in close agreement with the transient wall heat flux distribution at a mixed length of $0.4H$. An integral over time is computed for all the curves in Figure 5.30 by first subtracting the precursor value from each of these curves. This integral value represents the amount of energy (in *Joules*) added per square meter to the heated plate due to passage of one bubble. Figure 5.31 illustrates this amount of excess flux added into the heated surface due to passage of a single bubble as a function of the mixed length. The energy enhancement above background level is solely due to the strong mixing induced by the vortex structures downstream of the confined cylindrical bubble. It is concluded that if a cylindrical bubble spans the entire channel, the mixed length is 35% to 40% of the channel height irrespective of the speed of the plate (or speed of the bubble in a laboratory reference frame). This means that the bubbles at 20% mixed length, observed in

experiments conducted by Özer (2010) and Oncel (2011) take on the shape of a pancake or a hemisphere.

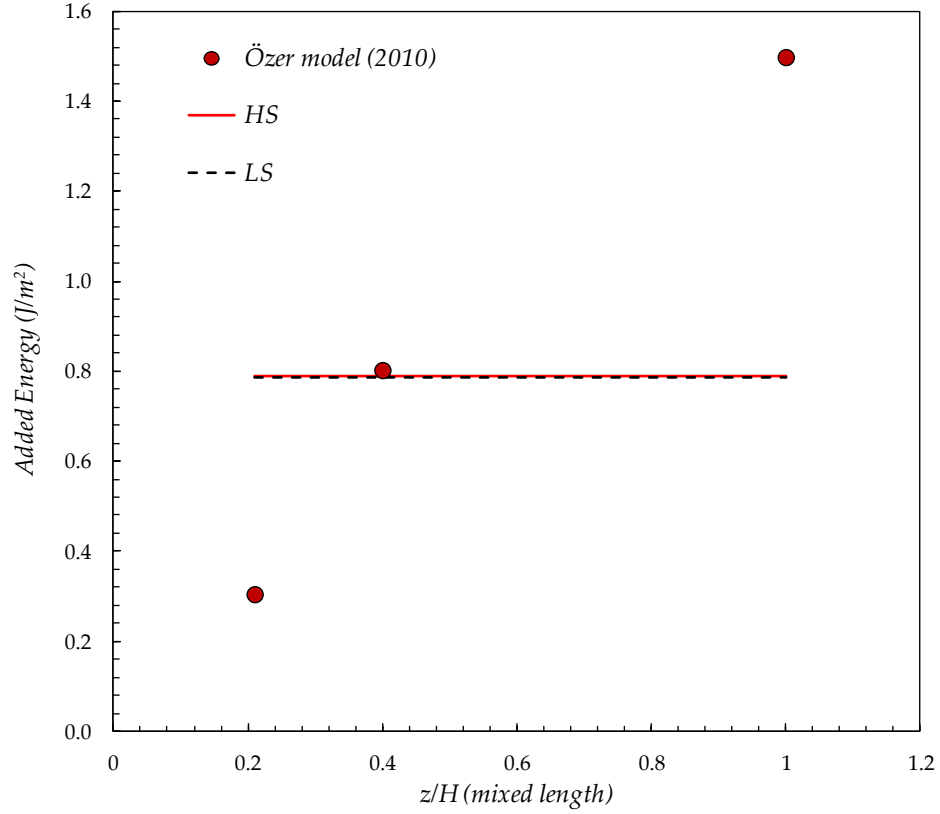


Figure 5.31 Energy added into the heated plate due to single bubble passage as a function of the mixed length.

The added power (into the plate) per unit streamwise length is plotted against the streamwise length downstream of the tail of the bubble for both HS and LS cases in Figure 5.32. These curves show facet averages of the total surface heat flux perturbations over a width of $\pm D$ from the wall center-line plotted against each streamwise location downstream of the bubble. The area under these two curves gives the total added power into a section of the heated plate that is marked by a dashed line on the wall heat flux contour, also shown in Figure 5.32. The total added

power due to the passage of a single bubble for HS case (71.8 mW) is exactly twice that of LS case (35.9 mW).

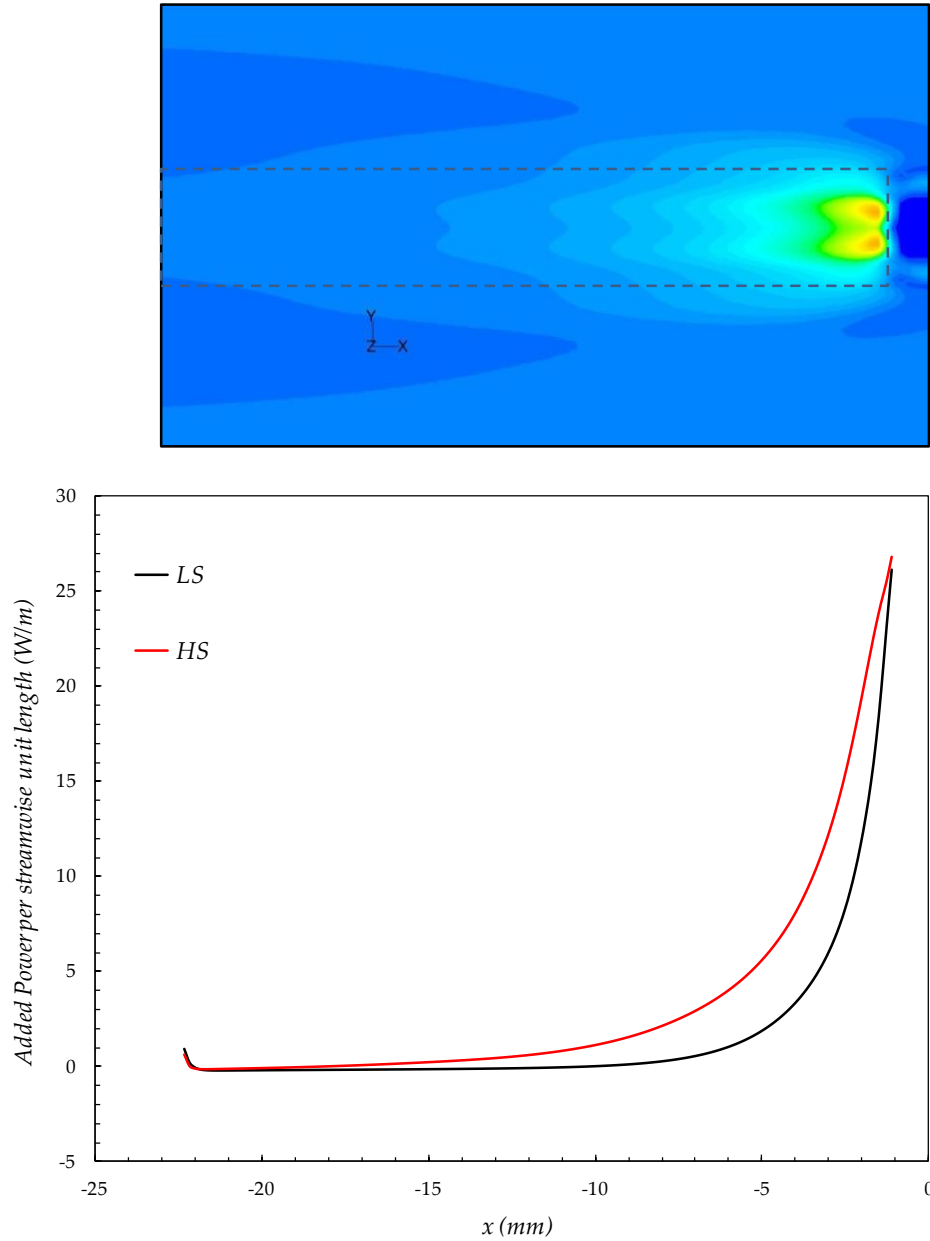


Figure 5.32 Power added to the plate per unit streamwise length downstream due to passage of a single confined cylindrical bubble for HS and LS cases. The integration is computed over an area shown by dashed line on the surface heat flux contours.

CHAPTER 6: SUMMARY AND CONCLUSIONS

6.1 SUMMARY

Two-phase cooling using mini-channels (with channel spacing near 1 *mm*) that highly confine the vapor phase offers enhanced convection through bubble-driven mixing mechanisms between the near-wall and bulk fluid and heat transfer via evaporation. The flow structure around the bubble moving in this confined geometry draws the low-temperature bulk fluid from the core of the channel towards the heated wall. This motion of the bulk fluid increases the temperature gradient at the heated wall near the bubble and thereby increases the average heat transfer coefficient in the channel.

A series of experimental investigations performed at the Heat Transfer and Phase Change Laboratory at the University of Houston pertaining to such flows concluded that, for highly subcooled flows, the heat transfer enhancement was due largely to cold liquid being transported nearer to the wall by the flow field near the bubble and not to evaporation of the liquid microlayer between the bubble and the wall. This study seeks to investigate this conclusion through using a direct numerical simulation of a simple model problem to identify a liquid transport mechanism which would explain the heat transfer enhancement. This numerical work uses the commercial software Fluent™ to perform the simulation (at laminar Reynolds numbers) of the flow and heat transfer around a confined cylindrical vapor bubble moving through a rectangular channel. The Volume of Fluid method is used to track the liquid-vapor interface and the bubble is held stationary within the computational domain by adopting a moving reference frame (Lagrangian coordinate system) that translates down the channel at the speed of the bubble. In the model problem, mass transfer by phase change through the liquid-vapor interface is not allowed so as to eliminate this energy transport mechanism from the

model. This was done to isolate the contribution of the liquid motion around the bubble to the wall heat transfer enhancement. Additional simplifications include prescribing a constant surface tension coefficient for the liquid-vapor interface and a constant static contact angle between the bubble surface and the upper and lower walls of the channel. Fully developed laminar flow was considered between the channel upper and lower walls along with the initial and boundary conditions consistent with the experiments of Özer (2010). The lower channel wall was treated as adiabatic and the upper channel wall was attached to a uniform-energy-generation foil of the same thickness and properties as used in Özer's experiments.

The computed velocity vector and vorticity fields are correlated to the solutions for the temperature and heat flux distributions of the upper heated surface. The time history of the wall heat flux of a point on the heated surface is also plotted and compared against the quenching/diffusion model proposed by Özer (2010).

6.2 CONCLUSIONS

The chief contributions and conclusions are:

- The centerline wall temperature traces showed a maximum depression at a distance of about $3D$ (LS case) and $5D$ (HS case) behind (to the left of) the rear surface the bubble. The temperature depression extended out of the left boundary of the computational domain in both cases and a higher degree of lateral diffusion was observed in the LS case. The bubble speed has a significant influence on the wall temperature distribution.
- The streamwise distribution of the driving temperature difference was shown to scale on the driving temperature difference present in the precursor flow if that ratio was plotted against a dimensionless distance formed on the hydraulic diameter and the Péclet number. This indicates that the effect of the bubble passage is to create a laminar thermal boundary layer

that “starts” at the rear of the bubble and extends behind (to the left) of the bubble. More runs at different bubble speeds and fluid diffusivities would be needed to verify this interpretation.

- A two-lobed structure in wall heat flux formed immediately behind (to the left) of the bubble where the largest heat flux values (around 11 to 13 times the precursor value) were observed. The plot of wall heat flux along the plate centerline showed a dramatic increase of heat flux 1 *mm* downstream of the rear of the bubble. The flow structure around the bubble drives the formation of the heat flux lobes downstream of the bubble. It is the wall heat flux and not the wall temperature that correspond most closely with the flow structure in the near field of the bubble.
- Adjacent to the trailing (left) edge of the bubble, the centerline Nusselt was nearly 9 times the precursor value. The shape of the Nusselt number curve to the left of the bubble was similar to the wall centerline heat flux plot. By comparison to the heat flux, the centerline wall temperature depression (around 3 °C) was not large enough to control the shape of the Nusselt number distribution.
- Due to the low thermal conductivity of the fluid, the heated plate had a time constant of more than two seconds. Thus, in one plate time constant, the plate (when moving at 44 *mm/s*) traverses nearly 94 *mm* in the computational reference frame. With the computational domain being only 30 *mm* in length, the depression in wall temperature must extend out of the domain. This is also true for the low-speed case. It is this plate time constant that is the longest in the simulation, and the presentation and analysis of results after t^* of 3 to 5 (3 to 5 plate traverses) allows the plate temperature and heat flux to adjust away from the initial condition and to come to a steady behavior consistent with the passage of the bubble.

- Contour plots of vorticity magnitude tiled with velocity vectors showed that a pair of large vortex structures (initiated by the formation of a strong upstream vortex) appear as pillars across the channel immediately behind (to the left of) the bubble. These structures lie near the maximum heat flux lobes on the heated surface and pump cold bulk fluid towards the heated wall in a pattern that forms the heat flux lobes.
- The total energy enhancement over the background level due to a single bubble passage for the HS case (71.8 *mW*) was twice as that of LS case. This result indicates that the power added to the flow due to a single bubble passage scales directly with the bubble velocity.
- The increase in energy into the plate due to passage of a single bubble confined in a rectangular narrow channel was nearly 29.5% and 59% of the precursor value for the LS and HS cases respectively. If multiple bubbles are present as observed in the experiments by Özer (2010) and Oncel (2011), the enhancement would be larger.
- The simulation results corresponded to a thermally well-mixed region in Özer's (2010) quenching/diffusion model of 40% of the channel height. Özer found a mixed length in the range of 20 – 50% of the channel height that produced results consistent with his measurements of the passage of multiple bubbles. Oncel (2011) suggested from his data that a mixed length of 16% was consistent with the passage of a single bubble. The current results of 40% for a single cylindrical bubble infers that the bubbles observed in experiments by Özer (2010) may have been hemispherical or “pancake” in shape or a range of shapes.
- With the available computational resources, the numerical grid was unable to adequately resolve the large gradients in velocity and temperature near the juncture of the heated wall and the liquid-vapor interface. However, this study elucidates the basic secondary flow patterns around the bubble which are responsible for heat transfer enhancement and solves other challenges associated with the approach selected to simulate this model problem.

6.3 RECOMMENDATIONS FOR FUTURE WORK

Based on the outcome of this investigation, recommendations for future work are as follows:

- A direct, immediate addition to the present work would be to use the facility within Fluent™ to allow the injection of particles into the flow to study the motion of the fluid closer to the wall and the bubble and the formation of vortices behind the bubble.
- The foremost suggestion for a follow-on study is to repeat this simulation with
 - (a) a more highly resolved grid near the bubble with a boundary layer mesh near the bubble-wall interface, and
 - (b) a range of liquid diffusivities to verify the findings as to wake decay, and
 - (c) bubble geometries that include both cylindrical and hemispherical bubbles, and
 - (d) the use of parallel computing to reduce the time required for these computations.
- The question of bubble shape in a real channel flow remains open as illustrated by the difference in the mixed-length computations described in the previous section. Future experimental work is necessary to image the profile of these bubbles from the side walls or end walls of the channel in order to clarify this issue.
- A longer-term and more ambitious undertaking would be to extend this work by the inclusion of phase change, variable surface tension, and a dynamic contact angle. Akhtar's (2011) corrections to the Fluent™ phase-change model can be incorporated and the simulations can be re-run. The issue of the inclusion/existence of a liquid microlayer between the bubble and the walls would be an element of consideration here.

REFERENCES

- Akhtar, M. W.**, "Numerical investigation of vapor bubble interaction with a superheated wall,"
PhD Dissertation, Department of Mechanical Engineering, University of Houston, 2011.
- Akhtar, M. W.**, "Rising vapor bubble approaching an inclined heated wall," *M.S. Thesis*,
Department of Mechanical Engineering, University of Houston, 2006.
- Bayazit, B. B.**, 2000, "A thermographic analysis of the heat transfer mechanisms generated by a
sliding bubble," *M.S. Thesis*, University of Houston, Houston, TX.
- Bayazit, B. B., Hollingsworth, D. K. and Witte, L. C.**, "Heat Transfer Enhancement Caused by
Sliding Bubbles," *J. Heat Transfer*, **125**: 503-509, (2003).
- Brackbill, J. U., Kothe, D. B., Zemach, C.**, "A continuum method for modeling surface tension,"
J. Comput. Phys., **100**: 335-354, (1992).
- Bush, John W. M.**, "The anomalous wake accompanying bubbles rising in a thin gap: a
mechanically forced Marangoni flow," *Journal of Fluid Mechanics*, **352**, pp 283-303 (1997).
- Bussman, M., Mostaghimi, J. and Chandra, S.**, "On a three-dimensional volume tracking model
of droplet impact," *Phys. Fluids*, **11**: 1406- 1417, (1999).
- Bustnes, O. E.** (2002), "Heat transfer near single sliding vapor bubbles," *M.Sc Thesis*, University
of Oxford.
- Chang, Y. C., Hou, T. Y., Merriman, B. and Osher, S.**, "A level set formulation of Eulerian
interface capturing methods for incompressible fluid flows," *J. Comput. Phys.* **124**: 449-
464, (1996).
- Chorin, A. J.**, "On the Convergence of Discrete Approximations to the Navier-Stokes Equations,"
Mathematics of Computation **Vol. 23, No. 106** (Apr., 1969), pp. 341-353

- Clift, R., Grace, J. R. and Weber, M. E., Bubbles, drops and particles, Academic Press, New York, (1978).
- Cooper, M. G., Lloyd, A. J., "The microlayer in nucleate boiling," *Int. J. Heat Mass Transfer*, **12** (1969), pp. 895-913
- Delhaye, J. M., 1974, "Jump conditions and entropy sources in two-phase systems, local instant formulation," *Int. J. Multiphase Flow*, **1**, 395-409.
- Esmaeeli, A. and Tryggvason, G., "Direct numerical simulation of bubble flows. Part I. Low Reynolds number arrays," *J. Fluid Mech.*, **377**: 313-345, (1998).
- Fedkiw, R. P. and Osher, S., "Level-set methods: An overview and some recent results," *J. Comput. Phys.*, **169**: 463, (2001).
- Ferziger, J. L. and Peric, M., 1996, Computational Methods for Fluid Dynamics, Springer-Verlag, Heidelberg.
- Fluent, Fluent™ User's Guide. Fluent Inc, 2003.
- Heaton, H. S., Reynolds, W.C., and Kays, W.M., 1964, "Heat transfer in annular passages, simultaneous development of velocity and temperature fields in laminar flow," *Intl. J. Heat Mass Transfer*, **Vol. 7**, pp. 763-781.
- Hirt, C. W. and Nichols, B. D., "Volume of fluid (VOF) method for the dynamics of free boundaries," *J. Comput. Phys.*, **39**: 201, (1981).
- Hollingsworth, D. K., Witte, L. C., Figueroa, M., 2009, "Enhancement of Heat Transfer behind Sliding Bubbles," *Journal of Heat Transfer*, **Vol. 131**, 121005 (9 pp.)
- Houston, S. D. and Cornwell, K., "Heat Transfer to Sliding Bubble on a Tube under Evaporation and Non-Evaporation Conditions," *Int. J. Heat Mass Transfer*, **39**: 211214, (1996).
- Kataoka, I., 1986, "Local instant formulation of two-phase flow," *Int. J. Multiphase Flow*, **12**, 745-758.

- Kenning, D. B. R, Zu, Y. Q., Yana, Y. Y., Gedupudi and S., Karayiannis, T. G.,** "Confined bubble growth during flow boiling in a mini-/micro-channel of rectangular cross-section part II: Approximate 3-D numerical simulation," *International Journal of Thermal Sciences* **50** (2011) 267-273.
- Kenning, D. B. R., Bustenes, O. E. and Yan, Y.,** "Heat transfer to a sliding vapor bubble," *Proc. of Boiling 2000: Phenomena and Emerging Applications*, Girdwood, Alaska, April 30-May 5, 253-27, (2000).
- Koffman, L. D., Plesset, M. S.,** "Experimental observations of the microlayer in vapor bubble growth on a heated solid," *J. Heat Transfer*, **105** (1983), pp. 625–632.
- Kothe, D. B., Mjolsness, R. C. and Torrey, M.D.,** "RIPPLE: A Computer Program for Incompressible Flows with Free Surfaces," *Technical Report LA-12007-MS*, Los Alamos National Laboratory, April, (1991).
- Kusuda, H., Monde, M., Uehara, H. & Otsubo, K.** 1981, "Bubble influence on boiling heat transfer in a narrow space," *Heat Transfer Jap. Res.* **9**, 49-60.
- Ladd, A. J. C.,** "Numerical simulations of particulate suspensions via a discretized Boltzmann equation, Part 1: Theoretical foundation," *J. Fluid. Mech.*, **271**: 285-309 (1994).
- Li, D., Dhir, V. K.,** "Numerical Study of a Single Bubble Sliding on a Downward Facing Heated Surface," *J. Heat Transfer*, July 2007, **Volume 129, Issue 7**, 877 (7 pages).
- Li, X.,** 2005, "An experimental study of the microlayer thickness and the kinematics of a sliding vapor bubble," *PhD Thesis*, Department of Mechanical Engineering, University of Houston.
- Maity, S., 2000,** "Effect of Velocity and Gravity on Bubble Dynamics," *MS thesis*, University of California, Los Angeles, CA.

- Maneri, C. C. and Zuber, N.**, "An experimental study of plane bubbles rising at inclination," *Int. J. Multiphase Flow*, **1**: 623-645 (1974).
- Manickam, S. and Dhir, V.**, (2003) "Holographic interferometric study of heat transfer associated with a single vapor bubble sliding along a downward-facing heater surface," *ASME Summer Heat Transfer Conference*, Las Vegas, Nevada.
- Mehdizadeh A., Sherif S. A., Lear W. E.**, "Numerical simulation of thermofluid characteristics of two-phase slug flow in microchannels," (2011) *International Journal of Heat and Mass Transfer*, **54 (15-16)**, pp. 3457-3465.
- Mei R., Chen W., Klausner J. F.**, "Vapor bubble growth in heterogeneous boiling-II: Growth rate and thermal fields," *International Journal of Heat and Mass Transfer*, **38 (5)**, pp. 921-934 (1995).
- Monde, M.** 1988 "Characteristics of heat transfer enhancement due to bubbles passing through a narrow vertical channel," *J. Heat Transfer* **110**, 1016-1019.
- Monde, M. and Mitsutake, Y.**, "Enhancement of heat transfer due to bubbles passing through a narrow rectangular channel," *Int. J. Multiphase Flow* **Vol. 15, No. 5**, pp. 803-814, 1989.
- Monde, M., Mihara, S., Mitsutake, Y., and Shinohara, K.**, 1989, "Enhancement of heat transfer due to bubbles passing through a narrow vertical rectangular channel (Heat transfer enhancement in subcooled liquid)," *Wärme und Stoffübertragung*, **Vol. 24**, pp. 321-327.
- Muzaferija S., Peric M., Sames P., Schellin T.**, "A two-fluid Navier–Stokes solver to simulate water entry," *Proceedings of 22nd Symposium on Naval Hydrodynamics, Washington, DC*, 1998; 638–651.
- Nichita, B. A.** (2010), "An improved CFD tool to simulate adiabatic and diabatic two-phase flows," *PhD Dissertation*, Ecole Polytechnique Federale De Lausanne.

- Oncel, A. F.**, "Heat transfer caused by the controlled production of sliding vapor bubbles in laminar subcooled flow in a narrow channel," *PhD Dissertation*, Department of Mechanical Engineering, University of Houston, 2011.
- Özer, A. B.**, "A combined photographic/thermographic study of highly subcooled flow boiling in a narrow channel," *PhD Dissertation*, Department of Mechanical Engineering, University of Houston, 2010.
- Özer, Arif B., Oncel, Ahmet F., Hollingsworth, D. Keith and Witte, Larry C.**, "The effect of sliding bubbles on nucleate boiling of a subcooled liquid flowing in a narrow channel," *International Journal of Heat and Mass Transfer* **54** (2011) 1930–1940.
- Özer, Arif B., Oncel, Ahmet F., Hollingsworth, D. Keith and Witte, Larry C.**, "A method for concurrent thermographic-photographic visualization of flow boiling in a minichannel," in: *Proceedings of the 14th International Heat Transfer Conference*, Washington, DC, 2010.
- Patankar, S. V.**, Numerical Heat Transfer and Fluid Flow: Series in computational methods in mechanics and thermal sciences, Taylor and Francis Pubs, (1980).
- Press, W. H., Teukolsky, S. A., Vetterling, W. T., Flannery, B. P.**, "Section 20.6: Multigrid Methods for Boundary Value Problems" – Numerical Recipes: The art of scientific computing (3rd edition), New York: Cambridge University Press, (2007).
- Qiu, D. and Dhir, V. K.**, "Experimental Study of Flow Pattern and Heat Transfer Associated With a Bubble Sliding on Downward Facing Inclined Surfaces," *Exp. Therm. Fluid Sci.*, **26**: 605-616, (2002).
- Rider, W. J. and Kothe, D. B.**, "Reconstructing volume tracking," *J. Comput. Phys.*, **141**: 112-152, (1998).
- Rider, W. J. and Kothe, D. B.**, "Stretching and tearing interface tracking methods," in: *12th AIAA CFD Conference*, San Diego, USA, (1995).

- Rudman, M.**, "Volume-tracking methods for interfacial flow calculations," *Int. J. Numerical Methods Fluids*, **24**: 671-691, (1997).
- Sankaranarayanan, K., Shah, X., Kevrekidis, I. G. and Sundaresan, S.**, "Analysis of drag and added mass forces in bubbly suspensions using an implicit formulation of the lattice Boltzmann method," *J. Fluid Mech.*, **452**: 61-96, (2002).
- Senthilkumar, S.**, "Computations of bubble dynamics with heat transfer," *PhD Thesis*, School of Mechanical and Manufacturing Engineering, Dublin City University, 2009.
- Sethian, J. A.**, Level Set Methods, Cambridge, UK: Cambridge Univ. Press; (1996).
- Son, G.**, "Numerical Study on a Sliding Bubble during Nucleate Boiling," *KSME Int. J.*, **15**: 931-940, (2001).
- Sussman, M., Smereka, P. and Osher, S.**, "A level set approach for computing solutions to incompressible two-phase flow," *J. Comput. Phys.*, **114**: 146-159, (1994).
- Thorncroft, G. E. and Klausner, J. F.**, "The Influence of Vapor Bubble Sliding on Forced Convection Boiling Heat Transfer," *J. Heat Transfer*, **121**: 73-79, (1999).
- Tryggvason, G., Bunner, B., Esmaeeli, A.**, "A front tracking method for the computations of multiphase flow," *J. Comput. Phys.*, **169**: 708-759, (2001).
- Unverdi, S. O. and Tryggvason, G.**, "A front-tracking method for viscous, incompressible multi fluid flows," *J. Comput. Phys.* **100** : 25-37, (1992).
- Welch, J. E., Harlow, F. H., Shannon J. P. and Daly, B. J.**, "The MAC method: A computing technique for solving viscous incompressible transient fluid flow problems involving free surfaces," **Report LA-3425**. Emeryville, CA: Los Alamos Scientific Laboratory; (1965).
- Youngs, D. L.**, "Time-dependent multi-material flow with large fluid distortion," In: Morton KW, Baines MJ, eds, Numerical Methods for Fluid Dynamics, New York, NY: Academic Press; 273-285, (1982).

APPENDIX A: THERMOPHYSICAL PROPERTIES OF WORKING MATERIALS

This section contains the relevant thermo-physical properties of the materials used in this numerical study, listed in a tabular form below. The information for 3M™ Novec™ 649 and HASTELLOY® C-276 is abstracted from the 3M™ manufacturing data sheet and the product section of the Haynes International, Inc website respectively.

Table A.1 Thermo-physical properties of the materials (abstracted from manufacturers' data sheets).

PROPERTIES	3M™ Novec™ 649	HASTELLOY® alloy C-276
Appearance	colorless and low odor fluid	corrosion-resistant alloy
Average Molecular Weight	316	-
Boiling Point (1 atm), °C	49	-
Pour (Melting) Point, °C	-108	1371
Estimated Critical Temperature, °C	169	-
Estimated Critical Pressure, MPa	1.88	-
Vapor Pressure, kPa	40	-
Latent Heat of Vaporization, kJ/kg	88	-
Density, kg/m ³	1600	8970
Kinematic Viscosity, centistokes	0.40	-
Absolute Viscosity, centipoises	0.64	-
Specific Heat, J/kg-K	1103	397
Thermal Conductivity, W/m-K	0.059	8.9
Coefficient of Expansion, K ⁻¹	0.0018	11.2 x 10 ⁻⁶
Surface Tension, N/m	0.0108	-

APPENDIX B: USER DEFINED FUNCTIONS

This section contains the user-defined functions (UDFs) that implement in Fluent all the initial and boundary conditions used for the HS case this study. Comments have been added at specific places to understand the algorithm with respect to the discussions made in the section 4.4.2.

UDF for specifying initial and boundary conditions

```

/*****
  UDF for specifying initial and boundary conditions
  *****/

#include "udf.h"          /* must be at the beginning of every UDF */
#include "flow.h"
#include "sg.h"
#include "sg_mphase.h"
#include "mem.h"
#include <stdio.h>
#include <stdlib.h>
#include <unsteady.h>

float whf = 1907;          /* precursor wall heat flux */
float time, told;
float Tsat = 322.0;        /* liquid saturation temperature */
float Twall = 327.0;       /* initial wall temperature at the inlet */
float kf = 0.059;          /* thermal conductivity of the liquid */

float ks = 8.9;            /* thermal conductivity of the solid (plate) */
float rhof = 1600;         /* density of the liquid */
float rhos = 8970;         /* density of the solid (plate) */
float Cpf = 1103;          /* specific heat of the liquid */
float Cps = 397;           /* specific heat of the solid (plate) */
float Hc = 0.00125;        /* height of the channel */
float Hp = 0.000075;       /* thickness of the plate/foil */
float Lc = 0.03;           /* length of the channel and the plate */
float Lneg = 0.0225;       /* length to the left of the bubble */
float Lpos = 0.0075;       /* length to the right of bubble */
float ufluid = 0.054;      /* average velocity of the liquid */
float uplate = 0.044;      /* velocity of the plate or the moving reference
                             frame */

```

UDF for specifying the vapor temperature boundary condition

/* UDF for specifying the vapor temperature boundary condition */

```
DEFINE_ADJUST(vapor_temperature, domain)
{
    Thread *t;
    Thread **pt;
    cell_t c;
    Domain *pDomain = DOMAIN_SUB_DOMAIN(domain,P_PHASE);
    Domain *sDomain = DOMAIN_SUB_DOMAIN(domain,S_PHASE);

    if(!Data_Valid_P())
        return;
    time = RP_Get_Real("flow-time");
    if(time != told)
    {
        mp_thread_loop_c (t,domain,pt)

        if (FLUID_THREAD_P(t))
        {
            Thread *tp = pt[P_PHASE];

            begin_c_loop_all (c,t)
            {
                if(C_VOF(c, tp) == 0.0)
                {
                    if(C_T(c,t) <= Tsat)
                    {
                        C_T(c,t)= Tsat;
                    }
                }
            }
            end_c_loop_all (c,t)
        }
        told = time;
    }
}
```

UDF for specifying an inlet plate temperature profile boundary condition

/* UDF for specifying a inlet plate temperature profile boundary condition */

```
DEFINE_PROFILE(solid_inlet_temperature,thread,index)
{
    float x[ND_ND];
    float ft,z;
    face_t f;
    ft = RP_Get_Real("flow-time");

    begin_f_loop(f,thread)
    {
        F_CENTROID(x,f,thread);
        F_PROFILE(f,thread,index) = Twall + (whf/(rhof*Cpf*ufluid*Hc))*uplate*ft;
    }
    end_f_loop(f,thread)
}
```


UDF for specifying an outlet plate temperature profile boundary condition

```
/* UDF for specifying a outlet plate temperature profile boundary condition */  
  
DEFINE_PROFILE(solid_outlet_temperature,thread,index)  
{  
    float x[ND_ND];  
    float ft,z;  
    face_t f;  
    ft = RP_Get_Real("flow-time");  
  
    begin_f_loop(f,thread)  
    {  
        F_CENTROID(x,f,thread);  
        F_PROFILE(f,thread,index) = Twall + (whf/(rho*f*Cpf*ufluid*Hc))*(Lc +  
update*ft);  
    }  
    end_f_loop(f,thread)
```

UDF for specifying an inlet fluid temperature profile boundary condition

```
/* UDF for specifying a inlet fluid temperature profile boundary condition */  
  
DEFINE_PROFILE(BCinlet_fluid_temperature,thread,index)  
{  
    float x[ND_ND];  
    float z, ft;  
    face_t f;  
    ft = RP_Get_Real("flow-time");  
    begin_f_loop(f,thread)  
    {  
        F_CENTROID(x,f,thread);  
        z = (-x[2]*1000.+0.625)/1.25;  
        F_PROFILE(f,thread,index) = Twall + (whf/(rho*f*Cpf*ufluid*Hc))*update*ft -  
(whf*Hc/kf)*(0.5*(z*z*z*z) - (z*z*z) + z);  
    }  
    end_f_loop(f,thread)  
}
```

UDF for specifying an outlet fluid temperature profile boundary condition

```
/* UDF for specifying a outlet fluid temperature profile boundary condition */

DEFINE_PROFILE(BCexit_fluid_temperature,thread,index)
{
    float x[ND_ND];                /* this will hold the position vector */
    float z, ft;
    face_t f;
    ft = RP_Get_Real("flow-time");
    begin_f_loop(f,thread)          /* loops over all faces in the thread
                                     passed in the DEFINE macro argument */
    {
        F_CENTROID(x,f,thread);
        z = (-x[2]*1000.+0.625)/1.25;
        F_PROFILE(f,thread,index) = Twall + (whf/(rho*f*Cpf*ufluid*Hc))*(Lc +
        uplate*ft) - (whf*Hc/kf)*(0.5*(z*z*z*z) - (z*z*z) + z);
    }
    end_f_loop(f,thread)
}
```

UDF for specifying an inlet and exit velocity profile boundary condition

```
/* UDF for specifying a inlet and exit velocity profile boundary condition */

DEFINE_PROFILE(x_velocity,thread,index)
{
    float x[ND_ND];                /* this will hold the position vector */
    float z;
    face_t f;

    begin_f_loop(f,thread)          /* loops over all faces in the thread
                                     passed in the DEFINE macro argument */
    {
        F_CENTROID(x,f,thread);
        z = (x[2]*1000.0)/0.625;
        F_PROFILE(f,thread,index) = 1.5*ufluid*(1.0 - (z*z)) - uplate;
    }
    end_f_loop(f,thread)
}
```

UDF to initialize the fluid and solid domain

```
/* UDF to initialize the fluid and solid domain */

DEFINE_INIT(my_init_function, domain)
{
    Thread *t;
    cell_t c;
    face_t f;
    Thread **pt;
    Thread **st;
    Domain *pDomain = DOMAIN_SUB_DOMAIN(domain,P_PHASE);
    Domain *sDomain = DOMAIN_SUB_DOMAIN(domain,S_PHASE);

    float xc[ND_ND],x,y,z,zp,w,s,ft,dr,r,vofsp,vofsp;
    float ri = 0.75e-3;

    thread_loop_c (t, domain) /* to initialize velocity and temperature
                                fields of fluid and plate inside both
                                domains */
    {
        if (!FLUID_THREAD_P(t))
        {
            /* loop over all cells */
            begin_c_loop_all(c,t)
            {
                C_CENTROID(xc,c,t);
                x = xc[0] + Lneg;
                C_T(c,t) = Twall + (whf/(rho*f*Cpf*ufluid*Hc))*x;
            }
            end_c_loop_all(c,t)
        }
        else
        {
            /* loop over all cells */
            begin_c_loop_all(c,t)
            {
                C_CENTROID(xc,c,t);
                x=xc[0]+Lneg;
                z = (-xc[2]*1000 + 0.625)/1.25;
                w = (xc[2]*1000)/0.625;
                C_T(c,t) = Twall + (whf/(rho*f*Cpf*ufluid*Hc))*x -
                (whf*Hc/kf)*(0.5*(z*z*z*z) - (z*z*z) + z);
                C_U(c,t) = 1.5*ufluid*(1.0 - (w*w)) - uplate;
            }
            end_c_loop_all(c,t)
        }
    }

    mp_thread_loop_c (t, domain, pt) /* to patch the cylindrical bubble (vapor
                                        phase) inside the fluid domain */
    {
        if (FLUID_THREAD_P(t))
        {
            begin_c_loop_all (c,t)
            {
                C_CENTROID(xc,c,t);
```

```

x=xc[0];
y=xc[1];
r= fabs(sqrt(x*x+y*y));

dr = pow(C_VOLUME(c,t)*3./(4.*3.14159),1./3.);
if ( ri - r >= 0.0 )
{
    vofsp = (dr*dr + (ri-r)*(ri-r))/(2.0*dr*dr)+ (ri-r)/dr;
    C_VOF(c,pt[1]) = vofsp;
    C_VOF(c,pt[0]) = 1. - vofsp;

    if(vofsp > 1.0)
    {
        C_VOF(c,pt[1]) = 1.0;
        C_VOF(c,pt[0]) = 0.0;
    }
}
else if( ri - r < 0.0)
{
    vofsp = (dr*dr - (ri-r)*(ri-r))/(2.0*dr*dr)+ (ri-r)/dr;
    C_VOF(c,pt[1]) = vofsp;
    C_VOF(c,pt[0]) = 1. - vofsp;
    if(vofsp < 0.0)
    {
        C_VOF(c,pt[1]) = 0.0;
        C_VOF(c,pt[0]) = 1.;
    }
}
}
end_c_loop_all(c,t)
}
}

```

